



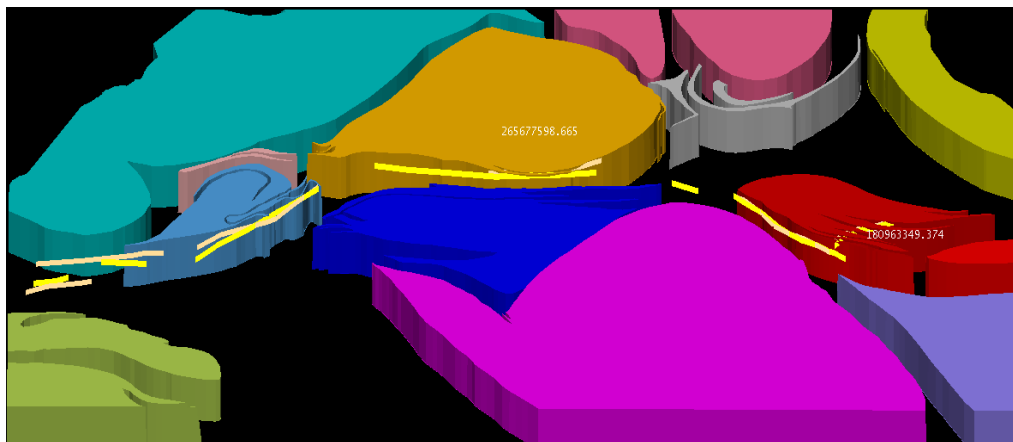
ARISTOTLE UNIVERSITY OF THESSALONIKI
FACULTY OF SCIENCES
SCHOOL OF GEOLOGY
DEPARTMENT OF MINERALOGY, PETROLOGY,
ECONOMIC GEOLOGY



SPYRIDON N. STRONGYLIS
Geologist

THREE-DIMENSIONAL MODELLING AND GEOCHEMICAL
ANOMALY MAPPING OF THE GOLD-ENDOWED HATTU SCHIST
BELT, EASTERN FINLAND

MASTER THESIS



THESSALONIKI
2023



"Taking a new step, uttering a new word, is what people fear most."
~ Fyodor Dostoevsky, Crime and Punishment (1866)



SPYRIDON N. STRONGYLIS
ΣΠΥΡΙΔΩΝ Ν. ΣΤΡΟΓΓΥΛΗΣ
Πτυχιούχος Γεωλόγος

THREE-DIMENSIONAL MODELLING AND GEOCHEMICAL ANOMALY
MAPPING OF THE GOLD-ENDOWED HATTU SCHIST BELT, EASTERN
FINLAND

ΤΡΙΣΔΙΑΣΤΑΤΗ ΜΟΝΤΕΛΟΠΟΙΗΣΗ ΚΑΙ ΧΩΡΙΚΗ ΑΝΑΛΥΣΗ ΓΕΩΧΗΜΙΚΩΝ
ΑΝΩΜΑΛΙΩΝ ΤΗΣ ΣΧΙΣΤΟΛΙΘΙΚΗΣ ΖΩΝΗΣ HATTU ΣΤΗΝ ΑΝΑΤΟΛΙΚΗ
ΦΙΝΛΑΝΔΙΑ

Υποβλήθηκε στο Τμήμα Γεωλογίας στα πλαίσια του Προγράμματος Μεταπτυχιακών
Σπουδών 'Εφαρμοσμένη και Περιβαλλοντική Γεωλογία', Κατεύθυνση 'Ορυκτοί Πόροι –
Περιβάλλον'

Ημερομηνία Προφορικής Εξέτασης: 19/01/2024
Oral Examination Date: 19/01/2024

Three-member Examining Board

Assistant Professor Dr. Grigorios Aarne Sakellaris, Supervisor
Associate Professor Dr. Alexandros Chatzipetros, Member
Professor Dr Nikolaos Kantiranis, Member

Τριμελής Εξεταστική Επιτροπή

Επίκουρος Καθηγητής Γρηγόριος Άαρνε Σακελλάρης, Επιβλέπων
Αναπληρωτής Καθηγητής Αλέξανδρος Χατζηπέτρος, Μέλος
Καθηγητής Νικόλαος Καντηράνης, Μέλος



© Spyridon N. Strongylis, 2023
All rights reserved.

THREE-DIMENSIONAL MODELLING AND GEOCHEMICAL ANOMALY
MAPPING OF THE GOLD-ENDOWED HATTU SHIST BELT, EASTERN FINLAND
– *Master Thesis*

© Σπυρίδων Ν. Στρογγύλης, 2023

Με επιφύλαξη παντός δικαιώματος.

ΤΡΙΣΔΙΑΣΤΑΤΗ ΜΟΝΤΕΛΟΠΟΙΗΣΗ ΚΑΙ ΧΩΡΙΚΗ ΑΝΑΛΥΣΗ ΓΕΩΧΗΜΙΚΩΝ
ΑΝΩΜΑΛΙΩΝ ΤΗΣ ΣΧΙΣΤΟΛΙΘΙΚΗΣ ΖΩΝΗΣ HATTU ΣΤΗΝ ΑΝΑΤΟΛΙΚΗ
ΦΙΝΛΑΝΔΙΑ – *Μεταπτυχιακή Διπλωματική Εργασία*

Citation:

Strongylis S., 2023. – THREE-DIMENSIONAL MODELLING AND GEOCHEMICAL ANOMALY
MAPPING OF THE GOLD-ENDOWED HATTU SHIST BELT, EASTERN FINLAND. Master Thesis,
School of Geology, Aristotle University of Thessaloniki.

Στρογγύλης Σ., 2023. – ΤΡΙΣΔΙΑΣΤΑΤΗ ΜΟΝΤΕΛΟΠΟΙΗΣΗ ΚΑΙ ΧΩΡΙΚΗ ΑΝΑΛΥΣΗ
ΓΕΩΧΗΜΙΚΩΝ ΑΝΩΜΑΛΙΩΝ ΤΗΣ ΣΧΙΣΤΟΛΙΘΙΚΗΣ ΖΩΝΗΣ HATTU ΣΤΗΝ ΑΝΑΤΟΛΙΚΗ
ΦΙΝΛΑΝΔΙΑ. Μεταπτυχιακή Διπλωματική Εργασία, Τμήμα Γεωλογίας Α.Π.Θ.

Any copying, storage and distribution of this work, in whole or part thereof for commercial purposes is forbidden. Reproduction, storage and distribution for nonprofit, educational or research nature, are authorized, on the condition that the source and this message are indicated. Questions concerning the use of this work for profit should be addressed to the author

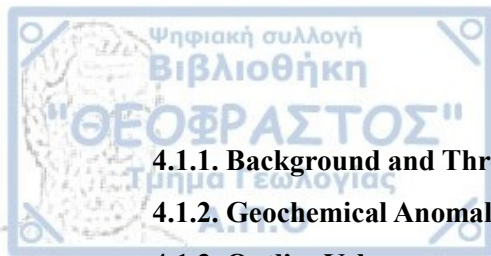
The views and conclusions contained in this document express the author and should not be interpreted as expressing the official positions of the Aristotle University of Thessaloniki.

Cover Figure: A brief illustration of the 3D geological modeling of the Hattu schist belt in Vulcan 2021.3 software showcasing the lithological intrusive units and the distribution of geochemical anomalies as constructed in ArcMap 10.8.1 GIS software



Contents

ABSTRACT	8
ΠΕΡΙΛΗΨΗ	9
ACKNOWLEDGEMENTS	10
CHAPTER 1. INTRODUCTION	11
1.1. HATTU SCHIST BELT – LOCATION, TOPOGRAPHY AND CLIMATE	11
1.2. EXPLORATION HISTORY OF THE HATTU SCHIST BELT	12
1.3. OROGENIC GOLD MINERALIZATION	14
1.3.1. Distribution of orogenic gold deposits	14
1.3.2. General characteristics of orogenic gold mineralization.....	15
1.3.3. Ore fluid pathways and traps	15
1.3.4. Ore fluid characteristics and source of metals	16
1.4. MINERAL EXPLORATION	20
1.4.1. History of gold exploration	20
1.4.2. Exploration stages	21
1.5. PURPOSE AND OBJECTIVES OF THIS THESIS	23
CHAPTER 2. GEOLOGY OF THE HATTU SCHIST BELT	25
2.1. REGIONAL GEOLOGICAL SETTING	25
2.2. GEOLOGICAL FRAMEWORK OF THE HATTU SCHIST BELT	26
2.2.1. Geological evolution	26
2.2.2. The Hattu Supersequence	28
2.2.3. Intrusive Units	29
2.2.4. Structural Evolution.....	29
2.3. GOLD OCCURRENCES	30
2.3.1. Gold Occurrences	30
2.3.2. Kuittila Zone	32
2.3.3. Hattuvaara Zone.....	33
2.3.4. Pampalo Zone	34
2.3.5. Hosko Zone.....	36
Chapter 3. Data and Software	38
3.1. BASEMAP AND STUDY AREA	38
3.2. LITHOLOGY	40
3.3. GEOCHEMISTRY	41
3.3.1. Soil Samples	42
3.3.2. Rock and drillcore samples.....	42
3.4. AIRBORNE MAGNETICS	43
3.5. STRUCTURE	44
3.6. SOFTWARE	44
CHAPTER 4. METHODOLOGY	45
4.1. TERMINOLOGY OF GEOCHEMICAL ANOMALY MAPPING	45



4.1.1. Background and Threshold Values	45
4.1.2. Geochemical Anomaly Values.....	45
4.1.3. Outlier Values.....	45
4.2. STATISTICAL ANALYSIS OF GOLD CONCENTRATIONS.....	46
4.2.1. Exploratory Data Analysis.....	46
4.2.2 EDA Graphical Tools.....	47
4.2.3 Boxplot.....	48
4.2.4 Dealing with censored-extreme (outliers) values	50
4.2.5. Threshold value estimation with EDA statistics and boxplot	50
4.2.6. Data transformations	52
4.3. SPATIAL PREDICTION.....	52
4.3.1. Deterministic methods.....	52
4.3.2 Inverse Distance Weighting (IDW)	53
4.3.3 Geostatistical Methods	55
4.3.4. The essential assumptions of Random Variables and Stationarity	56
4.3.5. The Experimental Variogram.....	58
4.3.6 Factors that affect the Experimental Variogram	60
4.3.7 Variogram models.....	63
4.3.8. Ordinary Kriging.....	65
4.3.9. Results Quality and Validity Assessment of IDW/OK Analyses	66
4.3.10. Interpolation Map	68
4.4. 3-DIMENSIONAL MODELLING.....	69
4.4.1. Explicit and implicit modelling techniques	69
4.4.2. 3-D Modeling Workflow.....	70
4.4.3 Data import and file formats	71
CHAPTER 5. RESULTS.....	73
5.1. DATA ANALYSIS.....	73
5.1.1. Data Reduction	73
5.1.2. Outliers	73
5.1.3 Descriptive Statistics	76
5.1.4. Data Transformation.....	78
5.2. THRESHOLD EVALUATION	81
5.3. VARIOGRAPHY.....	81
5.3.1. Trend analysis	82
5.3.2. Variogram parameters and models.....	82



5.3.3. Ordinary Kriging's Cross-Validation	86
5.3.4. Ordinary's Kriging Geochemical Maps	86
5.4. IDW INTERPOLATION	88
5.4.1. Characteristics of IDW	88
5.4.2. Inverse Distance Weighting's Cross-Validation	88
5.4.3. IDW's Geochemical Maps	89
5.4.4. Comparing Ordinary Kriging and Inverse Distance Weighting Methods	90
5.5. GEOCHEMICAL GOLD ANOMALY ZONES.....	92
5.6. DELINEATION OF GOLD ANOMALY LINEAMENTS.....	97
5.7. THREE-DIMENSIONAL (3-D) GEOLOGICAL MODELLING	98
5.7.1. 3-D Topography	98
5.7.2. 3-D lithological model.....	99
5.7.3. 3-D structural map	100
5.7.4. Geochemical data.....	101
5.7.5. Drill hole data	102
5.8. 3-D GEOLOGICAL MODEL AND GEOCHEMICAL ANOMALY MAP	102
CHAPTER 6. DISCUSSION AND CONCLUSIONS	104
6.1. STATISTICAL ANALYSES AND THRESHOLD ESTIMATION	104
6.2. SPATIAL INTERPOLATION	105
6.3. GEOCHEMICAL PREDICTION MAP.....	107
6.4. 3-D GEOLOGICAL MODELLING	108
6.5. FURTHER WORK.....	108
REFERENCES.....	109



ABSTRACT

Defining and mapping the geochemical signature, or hydrothermal footprint, of ore deposits from exploration survey records represents a key criterion in the mineral exploration procedure. In this research work is investigated the distribution of gold geochemical anomalies in the soil, bedrock and drill core sample datasets from the complexly deformed and gold-endowed Archaean Hattu schist belt, in Eastern Finland. This belt is approx. 40 km long and 5 km wide and hosts numerous orogenic-gold type deposits, including one active underground mine and over 20 gold prospects. The belt was initially separated in four continuous domains and further accurate geochemical gold anomaly maps were produced by applying two conceptually different interpolation methods, the Ordinary Kriging and the Inverse Distance Weighting. Several classic statistical and Exploratory Data Analysis methods were applied for the analysis of the distribution of the gold values and for the calculation of the threshold values, censored and outlier values, in each dataset. The available lithological, structural, geophysical datasets were further incorporated and combined with the geochemical interpolation maps to define gold anomaly lineaments in GIS-environment. The produced lineament maps highlight continuous, of several kilometers in length, zones with potential for discovering concealed gold occurrences underneath. The work included in addition the creation of the detailed regional 3-D lithological and structural map of the Hattu schist belt. The projected gold anomaly lineaments in the 3-D maps show that gold distribution in soil and bedrock follows collectively the western margin of tonalitic intrusions within the volcanic-sedimentary sequence aligning well with high-strain shear zones. The dispersion of the gold element in the soil was very narrow, ranging between 30 and 200 meters from the source rock. The 3D integrated geological model of this study provides evidence that the Hattu schist belt can be characterized as a single, crustal scale ore mineralizing system. Application of geochemical anomaly mapping could produce an updated exploration model for the area and dictate guidelines for future exploration for the discovery of new gold deposits.



Μία από τις σημαντικότερες διαδικασίες κατά την αναζήτηση μεταλλικών κοιτασμάτων είναι ο προσδιορισμός και η χαρτογράφηση του γεωχημικού, ή υδροθερμικού, αποτυπώματος από τα δεδομένα των γεωχημικών διασκοπήσεων. Σε αυτή την εργασία διερευνάται η κατανομή των γεωχημικών ανωμαλιών χρυσού βάσει γεωχημικών δειγμάτων από εδάφη, πετρώματα και γεωτρήσεις που συλλέχθηκαν στην Αρχαϊκή σχιστολιθική ζώνη Hattu, στην Ανατολική Φινλανδία. Η ζώνη αυτή εκτείνεται σε μήκος 40 χλμ. με πλάτος 5 χλμ. και φιλοξενεί πολυάριθμες εμφανίσεις μεταλλοφοριών χρυσού ορογενετικού-τύπου, συμπεριλαμβανομένου ενός ενεργού υπόγειου μεταλλείου. Για την εργασία αυτή, η σχιστολιθική ζώνη χωρίστηκε αρχικά σε τέσσερις επιμέρους συνεχείς ζώνες ενώ, δημιουργήθηκαν για κάθε μια από αυτές χάρτες γεωχημικών ανωμαλιών χρυσού με την εφαρμογή δύο διαφορετικών μεθόδων παρεμβολής, το Ordinary Kriging και το Inverse Distance Weighting. Στα γεωχημικά δεδομένα, εφαρμόστηκαν πολλαπλές μέθοδοι στατιστικής για την ανάλυση της κατανομής του χρυσού και για τον υπολογισμό των κατώτατων τιμών ανωμαλίας καθώς και των ακραίων τιμών. Τα διαθέσιμα γεωλογικά, τεκτονικά, γεωφυσικά δεδομένα ενσωματώθηκαν και συνδυάστηκαν με τους γεωχημικούς χάρτες για τον προσδιορισμό συνεχών ζωνών ανωμαλίας χρυσού σε περιβάλλον GIS. Στους χάρτες αυτούς αναγνωρίστηκαν συνεχείς γραμμικές ζώνες ανωμαλιών που εκτείνονται για αρκετά χιλιόμετρα και οι οποίες υποδηλώνουν την πιθανότητα ύπαρξης μεταλλοφορίας κάτω από το εδαφικό κάλυμμα. Με τη βοήθεια ενός λεπτομερούς τρισδιάστατου λιθολογικού και τεκτονικού μοντέλου για την σχιστολιθική ζώνη έγινε εμφανές ότι η κατανομή του χρυσού ακολουθεί το δυτικό άκρο των τοναλιτικών διεισδύσεων της περιοχής, στα όρια με τη μεταϊζηματογενή ακολουθία και των ζωνών διάτμησης. Η διασπορά του στοιχείου του χρυσού στο έδαφος είναι περιορισμένη, κυμαινόμενη μεταξύ 30 και 200 μέτρων. Το τρισδιάστατο γεωλογικό μοντέλο σε συνδυασμό με τον γεωχημικό χάρτη ανωμαλιών χρυσού αυτής της μελέτης παρέχει σημαντικές ενδείξεις πως οι διάσπαρτες εμφανίσεις των μεταλλοφοριών της σχιστολιθικής ζώνης Hattu ανήκουν σε ένα ενιαίο και συνεχές σύστημα μεταλλοφορίας με σημαντικό δυναμικό για την ανακάλυψη νέων κοιτασμάτων χρυσού.



ACKNOWLEDGEMENTS

This master's thesis was assigned to me following a series of highly constructive discussions with Assistant Professor Mr. Grigorios Arne Sakellaris at the Department of Mineralogy-Petrology-Economic Geology, Faculty of Geology, of the Aristotle University of Thessaloniki. Being my supervisor, I would like to express my heartfelt gratitude to him for entrusting me with this topic, for his willingness to assist me in achieving the best possible outcome, for his guidance, patience, and editing of my thesis. I would also like to thank him separately for his invaluable motivation and assistance in providing me with the opportunity to undertake an internship in Germany at Beak Consultants GmbH, which represents a significant turning point in my life.

Furthermore, I would also like to express my gratitude to Professor Nikolaos Kantiranis and Associate Professor Alexandros Chatzipetros for their revisions and comments on the writing of this thesis. More specifically, my gratitude to Mr. Kantiranis for the valuable discussions and his constructing comments in handling geochemical data. Similarly, to Mr. Chatzipetros for his assistance in understanding the tectonic evolution of my study area, the structural controls as well as the tectonic terminology. Additional thanks to Professor Georgios Vargemezis and Dr. Alexandros Stambolidis at the Department of Geophysics for their expertise and assistance in interpreting geophysical data. Sincere gratitude to Mr. Jani Rautio, Chief Geologist at Endomines Oy for providing and entrusting me with their data to work with. Warm appreciation to Maptek for supplying the state-of-the-art 3-D modeling software Maptek Vulcan 2021.3, which played a crucial role in the successful completion of this thesis.

Finally, in these typical acknowledgment's sections, I can't fully express my gratitude to my mother Sofia, my father Nestoras, my brother Argyris who provided all the materials, tangible and intangible support, love, and understanding throughout my academic studies, as well as throughout my life. Special thanks to my grandmother Sofia, grandfather Argyris and Marianna for their unwavering and unconditional faith in me since my early years.

Thessaloniki, 2023

CHAPTER 1. INTRODUCTION

1.1. HATTU SCHIST BELT – LOCATION, TOPOGRAPHY AND CLIMATE

The Late Archaean Hattu Schist Belt (HSB) is located in the central and easternmost part of Finland, in the North Karelia Province close to the Russian borders (Fig. 1.1). According to the Geodetic Coordinate System (GCS) the area crosses the 63°N latitude and 32°E longitude lines, situated approximately 500 kilometers northeast of the capital city, Helsinki. The area belongs to the rural municipality of Ilomantsi which has approx. 4000 inhabitants. The largest village in the area is Hattuvaara which is the easternmost village in Finland. The exact point of the easternmost continental part of the European Union lies on a small island within Lake Virmajärvi 19 kilometers east of Hattuvaara.

Location of Hattu Schist Belt

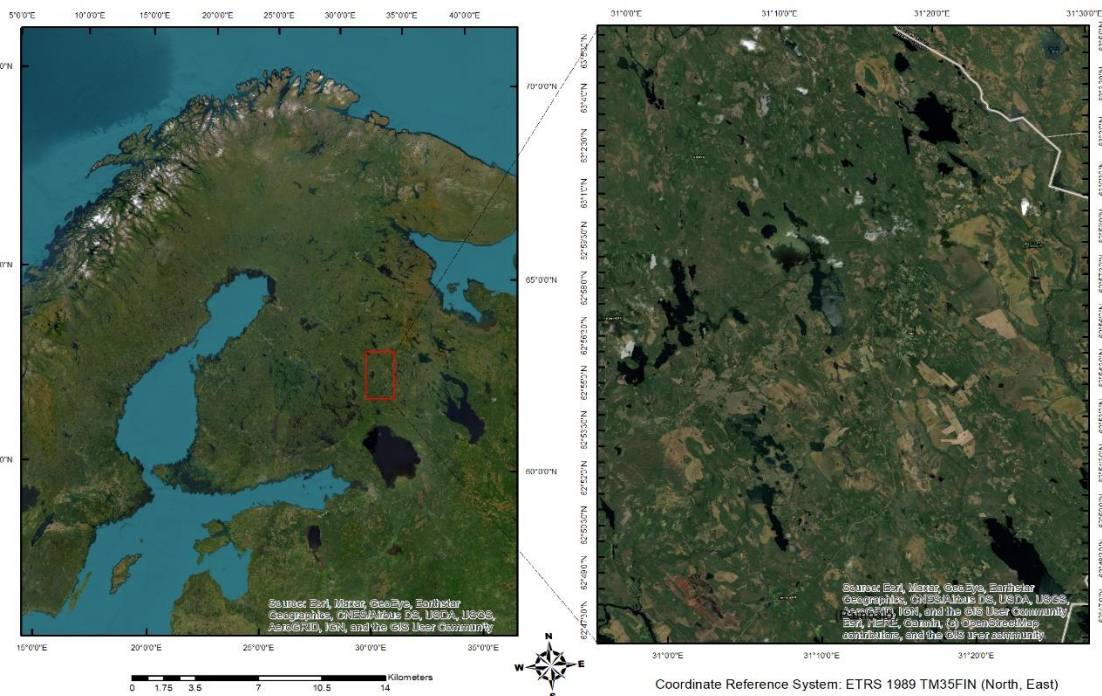


Fig. 1.1. Left the red rectangle shows the location and the extent of the Hattu schist belt in eastern Finland. The right figure is a zoomed-in perspective displaying the geomorphological details (lakes, forests etc.). The Russian borders are depicted by the white lines.



The area is sparsely populated characterized by sporadic small agricultural and pastoral holdings and is mostly covered by forests. It is situated in the temperate boreal forest zone, where the woodlands are mostly represented by a mix of Scots pine (*Pinus sylvestris*), Silver birch (*Betula pendula*), and Norway spruce (*Picea abies*). The terrain is characterized by swamps, wetlands, and glacial landforms that include eskers, moraines and isolated hills as the result of the last Ice age which shaped the current HSB's landscape. The bedrock is covered by Quaternary glacial and postglacial sedimentation, represented by continuous single, till sedimentary cover (moraine), with a typical thickness of 5 meters. A topographical characteristic in the HSB are the NW-SE trending chains of drumlins that produce noticeable hills, parallel to the route of the last ice sheet's retreat (Nenonen and Huhta, 1993).

The area can be climatologically positioned in the sub-arctic climate zone having average winter temperatures of -10°C , with snow covering the ground from early November until the end of April. From June to mid-August the summers are generally mild, with daily maximum temperatures frequently exceeding 20°C . Since there are many swamps and small lakes in the area, exploration field surveys and drilling take place during the wintertime when the ground and lakes are frozen. Outcrop mapping can be conducted from early May until late October, with the period from May to early June being ideal for fieldwork. Except for swampy places and thick forest parts, the area has good infrastructure and is easily accessible by vehicle.

In the greater region of North Karelia, three National Parks (Petkeljärvi, Patvinsuo, and Koli) have been established with the goal of preserving many aspects of its ecosystem. In 1992, HSB along with other parts of eastern Finland was nominated for the UNESCO "Biosphere Program", without having any impact on exploration or mining activities (Sorjonen-Ward, 1993).

1.2. EXPLORATION HISTORY OF THE HATTU SCHIST BELT

Until the early 1980s, gold had not a significant impact on Finland's mining history and economy and there was no well-defined understanding of the country's gold potential (Hartikainen and Nurmi, 1993). During the late 1970s, systematic mineral exploration for gold and other metals was initiated for a major part of Finland by the Geological Survey

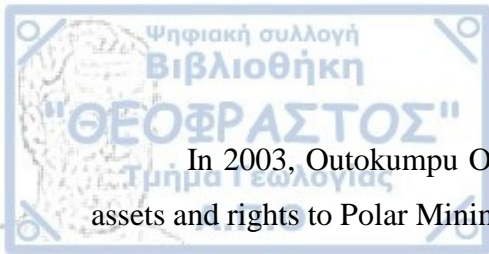


of Finland (GTK) and Outokumpu Oy, - a leading, state-owned mining exploration company at that time. Base metals and specifically nickel, copper and zinc were the main focus of exploration on that time (Salminen and Hartikainen, 1985; Sorjonen-Ward, 2015).

Gold exploration in the Hattu Schist Belt emerged in 1982, when systematic regional till geochemical mapping lead to identification of arsenic geochemical anomalies (Hartikainen and Salminen, 1982). The correlation between gold and arsenic was well-established and this incident intensified the exploration campaign for the following years.

In 1984, based on the till geochemical outcomes, additional exploration targets were indicated in the southern portion of HSB and particularly in the Kuittila region. There drilling exploration confirmed the existence of molybdenite and scheelite, and the presence of gold within a network of quartz veins in tonalites (Hartikainen and Damsten, 1991). Consequently, in 1985, GTK began an extensive and detailed exploration campaign, which aimed to determine the potential of gold resources of the HSB. During the years 1986-1992, GTK conducted the so-called “Ilomantsi Gold Project” exploration drilling campaign. This intense exploration in HSB resulted in the delineation of a 40 kilometers long gold-mineralization zone, known today as the “Karelian Gold Line”. The zone contains several gold-prospects and two currently active mines, the Pampalo and the small Rämepuro deposit. The results of the project are reported in GTK’S Special Paper 17 which contains 15 published articles regarding the geology and mineralization of HSB which still is the reference scientific database for the research in HSB (Nurmi and Sorjonen-Ward, 1993).

The southern part of the belt and the Pampalo mining lease were given to Outokumpu Oy, which owned the rights of the Hattuvaara area as well, while in 1996, a startup company, Endomines Oy (Jaakko Liikanen), obtained the northern concessions extending the exploration area from Pampalo to the north. Further regional exploration surveys were conducted by Outokumpu Oy close to the Russian border, but their primary focus remained the Pampalo area. Finally, Outokumpu established a small open pit production and by 1999 began selective underground mining. At Outokumpu Oy’s processing facilities, a total of 1755 kilograms of gold was produced from an ore quantity of 114,372 tons, resulting in an average grade of 15.3 ppm (Sorjonen-Ward et al., 2015).



In 2003, Outokumpu Oy ended the mining operations in the area, transferring its assets and rights to Polar Mining Oy. In 2006, with the same procedure, all Polar Mining's mining permits, rights, exploration data and findings, were leased to Endomines Oy. At Pampalo, although underground mining commenced in 1999, it was not until 2011 that excavation began on a large scale (Sorjonen-Ward et al., 2015). After a short period of seizure of mining activities between 2016-2018 due to low gold prices, currently intense exploration and gold production is being conducted by Endomines Oy throughout the belt.

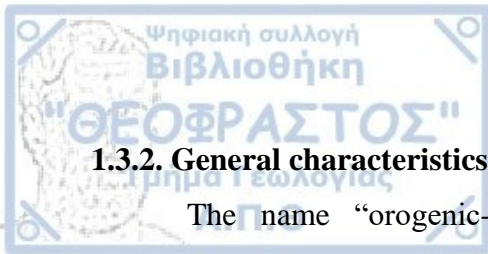
1.3. OROGENIC GOLD MINERALIZATION

1.3.1. Distribution of orogenic gold deposits

All discovered gold occurrences in the HSB are typical “orogenic-gold” type of deposits and the belt shares many similarities to other Archean orogenic gold provinces worldwide regarding the mineralization style, host rock lithologies and structural setting (Nurmi et al., 1993; Sorjonen-Ward et al., 2015). Generally, in Finland, the prevailing type of gold mineralization is orogenic, accounting for approximately 90% of the drilled gold occurrences in the country (Eilu et al., 2003).

Gold produced from orogenic-gold type of deposits represents almost one-third of the world gold reserves and over 75% of the gold that has been extracted by mankind throughout history comes from metamorphic terranes of Archean and Paleoproterozoic greenstone belts (Goldfarb et al., 2001; Frimmel, 2008; Phillips, 2013).

World-class gold-bearing quartz vein systems associated with Late-Archaean greenstone belts with major economic importance are the Barberton greenstone belt in the Kaapvaal craton of South Africa, the Kalgoorlie greenstone belt of Yilgarn craton in Western Australia, and the Abitibi greenstone belt in the Superior structural province of the Canadian Shield. Economically less significant orogenic gold ores can be found scattered within Late Archean greenstone belts in Africa, North America, and the Fennoscandinavian region (Meyer and Sager, 1985; Goldfarb et al., 2001).



1.3.2. General characteristics of orogenic gold mineralization

The name “orogenic-gold deposits” was established to substitute several terminologies such as lode gold, epigenetic etc. that refer to deposits exclusively containing gold and form a coherent group (Gebre-Mariam et al., 1995; Groves et al., 1998).

As implied by their name, all orogenic gold deposits are related to orogenic events. They are formed by compressional to transpressional deformation processes at convergent plate margins which could either be accretionary, or less commonly, collisional tectonic events related to subduction (Groves et al., 1998; Goldfarb et al. 2001, 2005). Since orogenic deposits are not formed in other types of tectonic regime, it is a strong indicator that convergent margins are the critical dynamic setting (Groves et al., 2020).

The deposits are formed in crustal depths that range from 2 to 20 km, while the most commonly reported conditions are between 1 and 5 kbar and 220 to 450 °C (Groves, 1993; Groves et al., 2020; Goldfarb and Groves, 2015). Groves et al., (1998), divided the deposits based on their depth of formation into epizonal for depths less than 6 km, mesozonal for depths between 6-12 km and hypozonal for those depths that exceed 12 km.

Despite their variability in geological age, which ranges from Precambrian to Phanerozoic, the orogenic-gold deposits exhibit consistent characteristics. These include: (1) syn- to late-timing of the mineralization relative to the peak metamorphism, (2) gold precipitation from low salinity fluids, (3) formation in broad thermal equilibrium with the host rocks, (4) metals enrichment in Ag, As, K, Sb ± B, Bi, Hg, Mo, Se, Te and W and low contents in base metals, and (5) structural control by crustal-scale shear zones (Gebre-Mariam et al., 1995; Groves et al., 1998; Goldfarb et al., 2001; Goldfarb and Groves, 2015; Fusswinkel et al., 2017; Kalliomäki et al., 2019).

1.3.3. Ore fluid pathways and traps

Metal transportation and dissolution requires ore-fluids to interact with extensive rock masses in order to create mineralization. Orogenic gold deposits display structural control, and the mineralization is linked to structural features such as shear zones, faults, and fractures (Cox et al., 2001). In most of the greenstone belts, economically important vein-type deposits are often connected with first order shear zones at the boundaries between contrasting lithostratigraphic units (Groves et al., 2018, 2000; Goldfarb et al.,

2005). These are situated in second and third order structures, close to large-scale often transcrustal compressional structures. The occurring structures range from ductile shear zones to brittle faults, stockwork networks, breccia, foliated zones, fold hinges (saddle riffs) etc. These structure pathways often exhibit extensive down-plunge continuity for long distances, reaching hundreds of meters to kilometers (Groves et al., 1998).

1.3.4. Ore fluid characteristics and source of metals

Orogenic gold deposits are typically formed from low salinity ore fluids, $H_2O \pm CO_2 \pm CH_4 \pm N_2 \pm H_2S$ (Groves et al., 2020). Three primary genetic concepts for the origin of the fluid were proposed by Kerrich (1983). These are illustrated in figure 1.2 and include: a) a syngenetic-exhalative, ii) a magmatic-hydrothermal (tonalite-, lamprophyre-, or oxidized magma-associated) and iii) a metamorphic (regional metamorphic devolatilization, lateral secretion, or mantle/granulitization). A meteoric fluid model was added later by Nesbitt (1991).

The syngenetic-exhalative models do not align with evidence, indicating that i.e. the stratiform to stratabound BIF-hosted gold deposits are syn- to late-metamorphic deposits, structurally controlled, formed by the sulfidation of magnetite (Phillips et al., 1984).

The meteoric-fluid models (Fig. 1.2.a) also cannot explain their formation as these are based on flawed calculations and interpretations of stable H and O isotope data, which are largely derived from the extraction of measured components from mixed (primary and secondary) fluid inclusions (Goldfarb and Groves, 2015).

The magmatic-hydrothermal models (Fig. 1.2.b) cannot explain the origin of many individual deposits or provide a universal mineral system model for orogenic gold formation (Wyman et al., 2016). Granitic intrusions can be post-, syn-, or pre-gold in the same terranes globally (Hughes et al., 1997; Goldfarb et al., 2008), or they can be completely missing in some places, like the Otago gold region in New Zealand (McKeag and Craw, 1989; Goldfarb et al., 2001). The age of gold deposits compared to the proposed fertile granitic intrusions are often not the same where comprehensive geochronological studies have been done (Goldfarb and Groves, 2015). In cases where lamprophyres and other mafic intrusions share the same age with the deposits, these are volumetrically

insignificant to provide the large fluid volumes required for a gold deposit formation (Vielreicher et al., 2010; Groves et al., 2019).

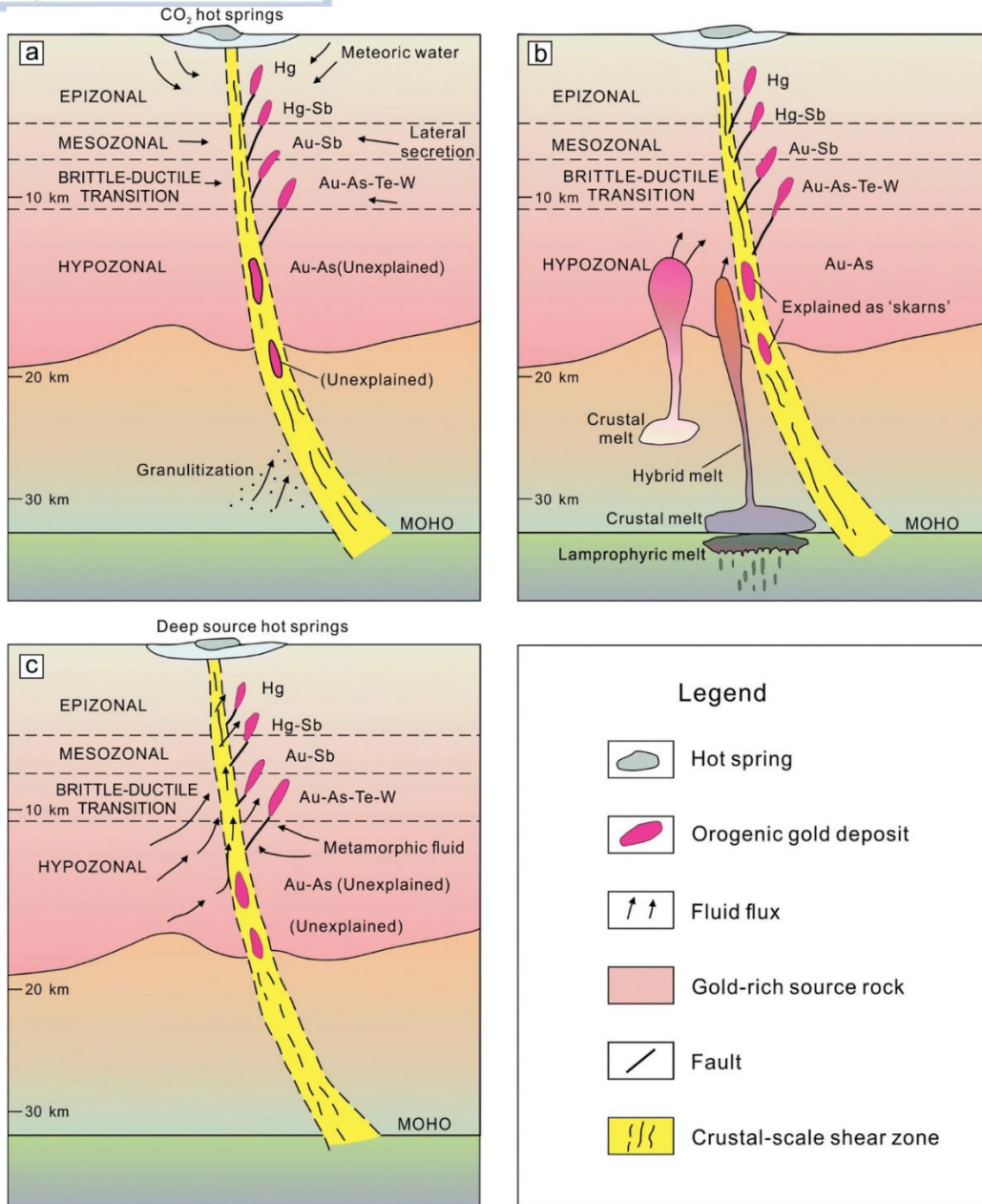


Fig. 1.2. Simplified schematic representation illustrating the various models for the origin of orogenic gold deposits and their ore-fluid source theories. The figure includes: (a) Shallow crustal meteoric, granulitization and metamorphic models (b) Magmatic-hydrothermal models, (c) Supracrustal metamorphic models (modified after Groves and Santosh, 2016; Groves et al., 2019).

Stable isotope data typically indicate a magmatic-hydrothermal fluid origin but considering that some deposits formed at depths exceeding 15 km, it is more likely that the fluids evolved through extensive vertical pathways rather than originating directly from magmatic-hydrothermal sources (Kontak and Kerrich, 1995; Ridley and Diamond, 2000).

The metamorphic origin model (Fig. 1.2.c) for the ore-fluid source supports the theory of the metamorphic devolatilization of the supracrustal rocks in the continental crust when greenschist- to amphibolite-facies conditions are present (Groves et al., 2020). The model places a strong emphasis on the massive upward advection of the resulting fluid and metals to the depositional location of orogenic gold mineralization at higher crustal levels (e.g. Groves et al., 1987; Cox et al., 1991). One of its key advantages is that it does not require any particular connection to host rock units or intrusion types.

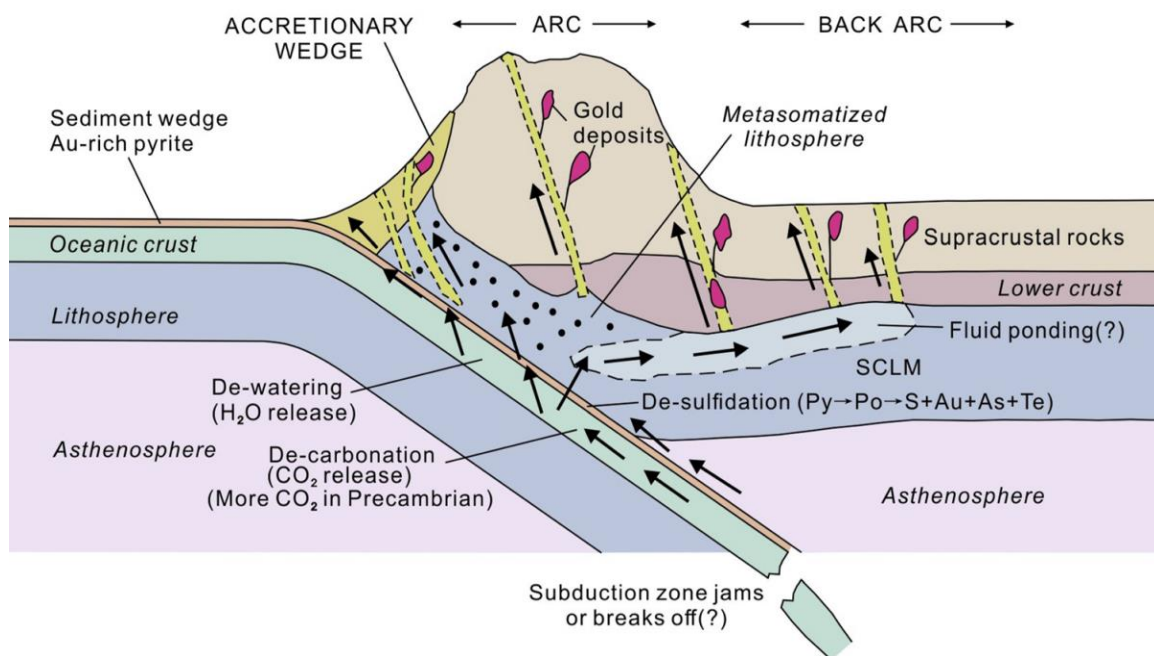
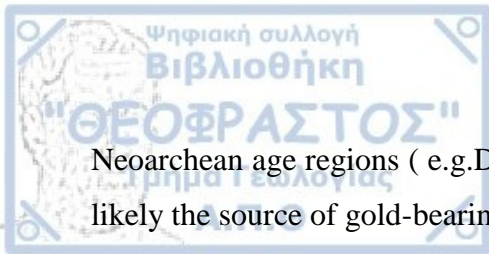


Fig. 1.3. Diagram illustrating the updated subduction-based worldwide model for the formation of orogenic gold deposits (Goldfarb and Groves 2015; Groves et al. 2020).

From the metamorphic devolatilization of supracrustal rocks, the characteristic low-salinity of H₂O-CO₂ (+/ CH₄, N₂, H₂S) fluids are also present (Fyfe et al., 1978; Tarantola et al., 2007). In the metamorphic model, the dominant rocks for producing fluids and metals might not have been stable over time (Goldfarb and Groves, 2015), In



Neoproterozoic age regions (e.g. Dong and Santosh, 2016), widespread mafic rocks are most likely the source of gold-bearing metamorphic fluids.

Limitations of this model are particularly prominent in Precambrian deposits, especially in China's Phanerozoic deposits. In these, evidence indicates that the ore fluids originated from depths over 15-km derived from the basement. There is also the challenge to define the mechanism that ore fluids migrated laterally on kilometer-scale into the larger-scale faults that control the position of most gold districts globally (Groves et al., 2020).

In contrast to previous models, there is a new hypothesis, the slab devolatilization model (Fig. 1.3) that was specifically developed for the giant Jiaodong gold province (Yang et al. 2014; Goldfarb and Santosh, 2014). This model is capable of becoming a universal model that can incorporate orogenic gold deposits including the deposits where regional metamorphism and the age of mineralization are inconsistent. The slab devolatilization hypothesis involves a common fluid source, the slab and the overlying pyritic sediment wedge. It has the potential to explain both the high CO₂ levels in Precambrian orogenic ore fluids, and the economic significance of Neoproterozoic deposits, which contain high gold contents of syngenetic pyrites in marine sediments. Unlike every model, there are a few gold regions in China, which considered as exceptions from this model, where there is evidence of an indirect relationship with subduction (Groves et al., 2020). In these examples, the auriferous fluid was generated by the devolatilization of the underlying metasomatized slab that was the outcome of an earlier orogeny.



1.4. MINERAL EXPLORATION

1.4.1. History of gold exploration

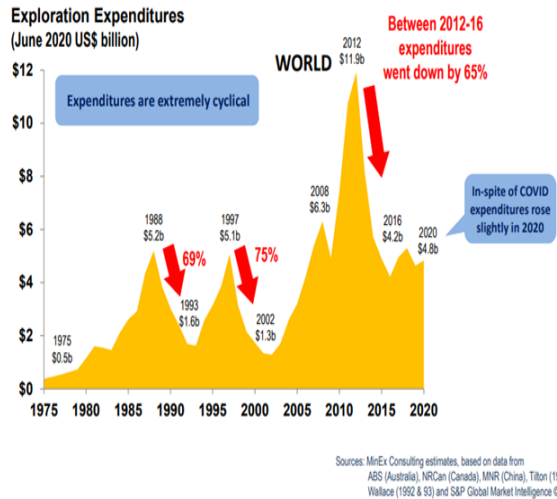
As stated by the Pan European Reserves and Resources Reporting Committee (PERC), a mineral resource refers to a concentration or an occurrence of material that holds economic significance, in such form, quality and quantity, that indicates reasonable expectations for eventual extraction. The mineral resources are classified further into metals (e.g. Au, Cu, Ni, Cr, Fe), industrial minerals and rocks (e.g. kaolinite, granite, marble, gemstones) and energy minerals such as coal, oil and natural gas (Khoshnaw, 2012).

One of the most significant traded commodities in the global economy is gold being used for thousands of years for monetary, jewelry, electronics along with some applications in medicine. Gold attracts the attention of both researchers and industry alike, owing to its unique characteristics and economic significance (Hauptfleisch et al., 2016).

Systematic exploration for gold in the last century started in the early 1970's, after significant rise of the price of gold, which led to increasing expenditures for exploration and the discovery of several large gold-endowed deposits (Fig. 1.4). This trend continued until 1993, while gold production reached its peak in 2001. At the early 2000's, the gold industry gold began to witness changes as the companies adopted a more cautious approach, carefully evaluating the profitability of new deposits before proceeding. Other companies chose to allocate more resources towards exploring other metals e.g. base metals rather than solely focusing on gold (Moon and Evans 2006).

In the last two decades, gold industry's expenditures for exploration have faced regular fluctuations reaching their peak in 2012. Since then, expenditures decreased by 65% but they are still remaining high without making noteworthy discoveries (Schodde, 2021). There has been a decline in exploration and a lengthening timeline to start mining operations (Fig. 1.4).

Gold Exploration Expenditures: World



Number of Gold Deposits found: World

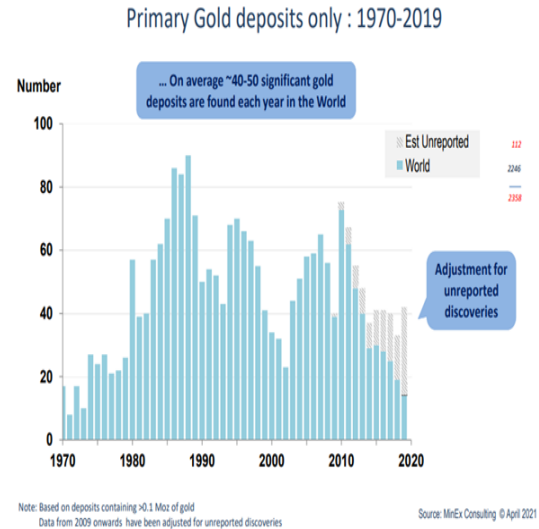


Fig. 1.4. Illustration of global gold exploration expenditures and the number of gold deposits discovered from the 1970s to 2020 (Schodde, 2021).

1.4.2. Exploration stages

Mineral exploration predominantly involves the discovery and identification of mineral deposits containing valuable minerals or metals that can be extracted economically. The exploration process (Fig. 1.5) is mainly divided into four phases: i) selection of the exploration area, ii) target generation, iii) evaluation of resources, and iv) determination of the size and quality of the reserve (Carranza, 2009). The first phase includes identifying regions where mineral deposits are likely to be found, called permissive regions, near the Earth's crust based on the geological conditions and processes that favor their formation (Singer, 1993).

The second phase deals with the delineation and narrowing down the prospect area into regions, by using exploration techniques that are compatible to the type of deposit being sought, and by analyzing geological, geochemical, and geophysical data. The identified areas are called prospective areas, and most likely contain a mineral occurrence. The third phase is the process of determining the quantity/quality of minerals or metals in the discovered deposit, mainly through drilling.

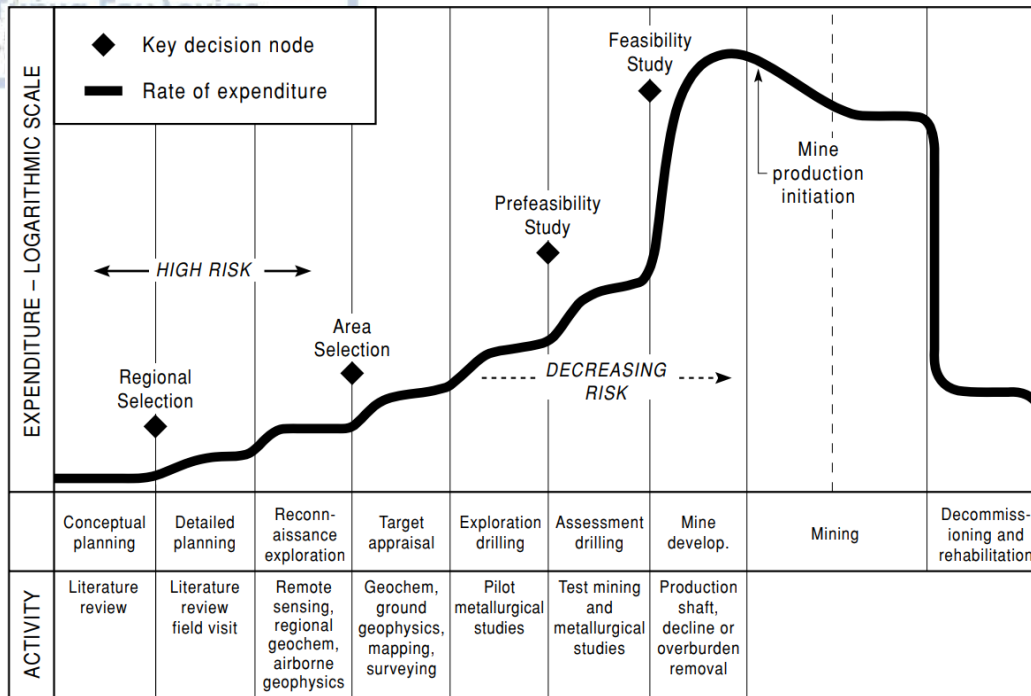


Fig. 1.5. Stages and key decision points of exploration process in a mineral exploration project (after Moon and Evans 2006).

Finally, the fourth phase incorporates categorizing different parts of the mineralization as reserves (proven and probable) or resources (measured, indicated, inferred), based on economic and technical feasibility analysis (Carranza, 2009).

Similar to the oil industry's approach in recent decades, the minerals industry strives to enhance the success rate of discoveries by minimizing the drilling of low-potential targets (Groves and Santosh, 2015). The primary techniques used to directly identify mineralization are airborne geophysics and geochemistry (Moon and Evans, 2006). Mapping geochemical anomalies holds significant importance in mineral exploration as it stands as one of the key methods.

During the late 1980s and 1990s, there were significant advancements in computer hardware and software, including GIS technology, which led to the rapid development of quantitative exploration techniques for mapping geochemical anomalies and mineral prospectivity (Burrough, 1986; Agterberg, 1989). Thus, it became easier to graphically and interactively display geoinformation, resulting in more convenient and efficient



interpretation of geochemical patterns and consequently more successful exploration (Harris et al., 2000).

1.5. PURPOSE AND OBJECTIVES OF THIS THESIS

The quest for comprehensive and effective exploration models to support mineral exploration and assist in the discovery of a mineral deposit, such as orogenic-gold deposit, remains a subject of ongoing research (e.g. Goldfarb and Groves, 2015; Groves et al., 2020). The focus of this thesis is to explore the geological and geochemical data of a gold-endowed belt in order to provide insights regarding the footprints of concealed mineralization in the earth's surface.

The primary objective of this research is to map and delineate the geochemical anomalies in the element gold that has been observed from field and drilling sampling campaigns in the gold district area of HSB. The second is to construct a three-dimensional (3D) geological model for the entire HSB from the available data set, as well as, from revised information through a detailed geological and structural data review and interpretation. The final output is a detailed three-dimensional geological model for the entire belt with integrated the geochemical data that identifies specific geochemical or/and geological patterns and could offer further insights and guide the mineral exploration. To accomplish this, certain objectives have been carried out as follows:

- Identification of geochemical gold anomalies by assessing the threshold values. The statistical Exploratory Data Analysis (EDA) technique is applied for the gold concentration data derived from the field and drilling surveys. The EDA technique is further tested for its reliability in estimating thresholds in demanding and complex univariate geochemical datasets.
- Conduct spatial analysis and employ the interpolation methods of Ordinary Kriging (OK) and Inverse Distance Weighting (IDW). The main target is to produce different continuous geochemical anomaly surfaces that make predictions in non-sampled locations and to compare/evaluate the performance of the two methods.



- Create a comprehensive 3D geological graphic representation for the entire gold-endowed belt, by revising and incorporating the two-dimensional geological and geochemical data with extracted three-dimensional data from the topographical, geological, structural, and geochemical data.



CHAPTER 2. GEOLOGY OF THE HATTU SCHIST BELT

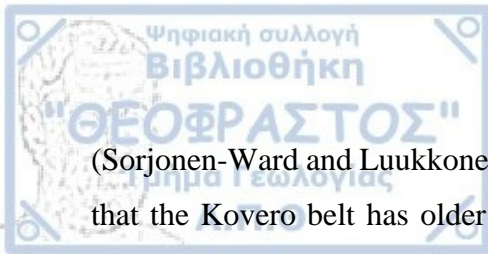
2.1. REGIONAL GEOLOGICAL SETTING

The Fennoscandian Shield is the largest exposed Precambrian domain in European Continent constituting the furthest northwestern part of the East European Craton, which includes the countries Finland, Sweden, Norway, and northwestern Russia (Weihed et al., 2005; Lahtinen et al., 2011). It shares many similarities with other shields in Australia, Canada and South Africa and is the superior in Europe producer of many metals including gold, chrome, copper etc. The shield has a high potential for new mineral discoveries and half of the current mineral exploration occurs in Sweden and Finland (Eilu, 2011).

Finland has a rich geological history that contains the oldest rocks of Fennoscandia being dated at 3.5 Ga in gneisses at Siurua (Central Finland) and possibly in kimberlites at Kaavi (Eastern Finland), with evidence of even older rocks dated at 3.7 Ga (Mutanen and Huhma, 2003; Huhma et al., 2011). The ages of Fennoscandia rocks generally decrease from northeast to southwest due to the accretion of new crust onto the pre-existing Archean core (Gaal, 1986). The most significant tectonic events are marked by two major orogenic events that occurred between 2800-2700 Ma and 1900-1800 and caused the separation between the Archean and Paleoproterozoic crust (Vaasjoki et al., 2005). These Archean and Paleoproterozoic rocks constitute the Fennoscandian shield in Finland (Fig. 2.1).

Several Archean greenstone belts in eastern Finland such as Tuntsa, Oijärvi, Suomussalmi, Kuhmo and Tipasjärvi have been recognized to contain orogenic-gold deposits (Airo 2007; Airo and Mertanen, 2008; Eilu et al., 2015). The most prospective of these belts is the Ilomantsi greenstone belt in easternmost Finland (Hölttä et al., 2012, 2016).

The Ilomantsi greenstone belt is located in the Archean Karelia domain and is part of a larger supracrustal zone known as the Ilomantsi-Kostamuksha greenstone belt (Sorjonen-Ward, 1993; Molnár et al., 2016). The Ilomantsi belt represents the youngest of several Archean greenstone belts in the Karelia, dated at 2750 Ma, and is divided into an eastern and a western section known as Hattu schist belt and Kovero belt, respectively



(Sorjonen-Ward and Luukkonen, 2005; Huhma et al., 2012). Their distinctive difference is that the Kovero belt has older rock strata and a higher proportion of mafic - ultramafic rocks (Sorjonen-Ward et al., 2015). Gold exploration has been concentrated in the HSB due and it was the first region in which Archaean “mesothermal” gold deposits have been reported in Fennoscandian shield (Nurmi et al., 1993; Sorjonen-Ward, 1993).

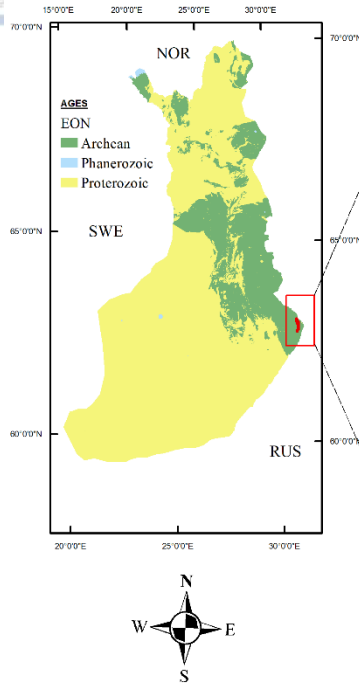
2.2. GEOLOGICAL FRAMEWORK OF THE HATTU SCHIST BELT

2.2.1. Geological evolution

The N-S trending Late Archean Hattu schist belt has an approximately 50 km strike length and up to 20 km width (Nurmi et al., 1993). The lithologies of the HSB can be mainly categorized into two dominant types: the supracrustal rock units or the Hattu Supersequence and the intrusive granitoid units. The supracrustals comprise predominantly metasedimentary rocks, feldspathic epiclastic rocks, intermediate to felsic volcanics and volcanoclastic rocks, smaller volumes of mafic to ultramafic volcanics and banded iron formations (Sorjonen-Ward, 1993). Briefly, the supracrustal sequence was deposited approximately between 2.71-2.75 Ga and based on field observations and isotopic analysis, were afterwards intruded (syn to post-tectonic emplacement) by felsic to intermediate porphyries, leucogranites, granitoids and tonalites having ages ranging from 2.76-2.70 Ga (Vaasjoki et al., 1993; Sorjonen-Ward, 1993; Huhma et al., 2012; Molnár et al., 2016; Käpyaho et al., 2017).

The depositional basement of the HSB remains unknown, however, zircon population in both supracrustal rocks and intrusive plutonic rocks was dated around 3.0 Ga, which indicates the presence of older crustal material (Huhma et al., 2012).

Fennoscandian Shield in Finland



Coordinate Reference System: ETRS 1989 TM35FIN (North, East)

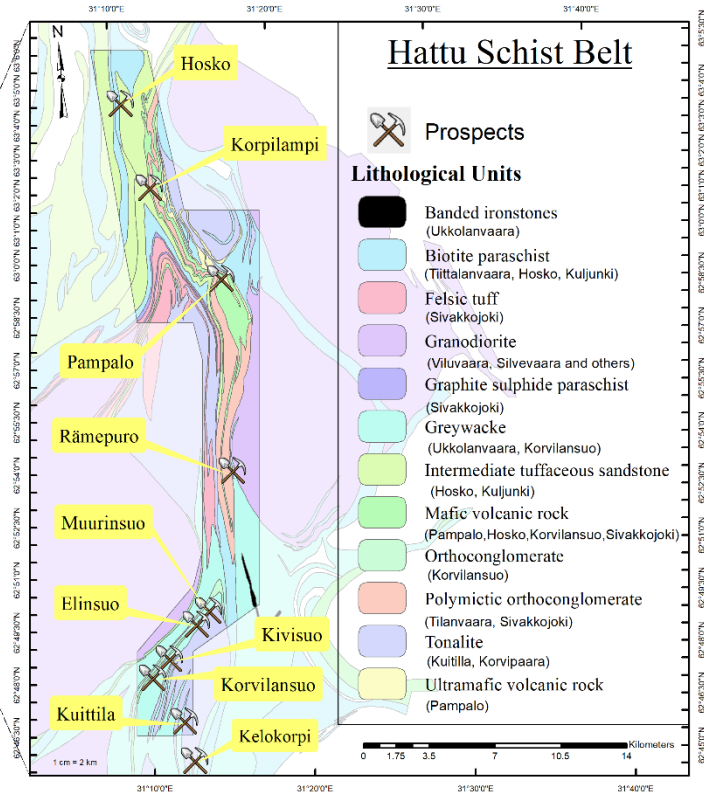
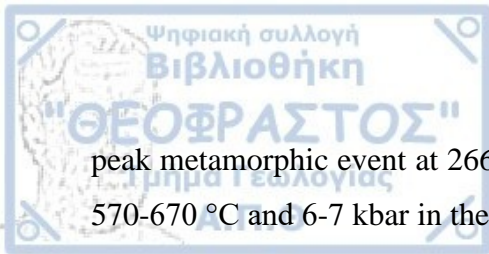


Fig. 2.1. Regional geological map of the Late-Archaeon Hattu schist belt. The figure highlights the study area and the lithological units and formations that are referred to in the text and the locations of known orogenic-gold deposits as prospects.

Deformation, metamorphism and intense hydrothermal alteration have affected all lithologies in the HSB (Sorjonen-Ward et al., 2015; Kalliomäki et al., 2019). Altered mineral assemblages through intense hydrothermal processes record metamorphic overprint and subsequent deformation at greenschist to lower amphibolite facies conditions with approximately peak temperature of 550 ± 50 °C and pressure of 3-5 kbar (Kojonen et al. 1993; O'Brien et al. 1993; Fusswinkel et al., 2017).

At 2.75 Ga, the HSB indicates rapid crustal evolution, probably within a continental margin arc setting or in an arc-continent collision (Vaasjoki et al., 1993; Sorjonen-Ward, 2015). According to titanite and monazite ages from granodiorite and leucogranite intrusions with U-Pb concordia intercepts between 2710 and 2696 Ga it is believed to give an estimate of the minimum age of crustal metamorphism and reworking (Vaasjoki et al., 1993). Based on recent results of monazite geochronology, Hölltä et al. 2016 suggests a



peak metamorphic event at 2660-2640 Ma which may have reached conditions as high as 570-670 °C and 6-7 kbar in the NE parts of the HSB.

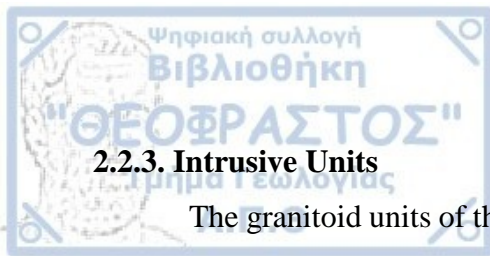
2.2.2. The Hattu Supersequence

Despite the strong deformation and metamorphism, the HSB hosts one of the most best-preserved Archean supracrustal sequences of Finland which maintains a consistent stratigraphic sequence and allows a proper description of lithostratigraphic units (Sorjonen-Ward, 1993). Based on primary lateral facies variations the volcano-sedimentary depositional environment was distinguished in two (partially overlapping) subvolcanic complexes that developed in turbidite basins (Sorjonen-Ward and Luukkonen, 2005, Sorjonen-Ward et al., 2015).

The northern part of the HSB consists of feldspathic graywackes of turbidite origin and coarse-clastic deposits of the Sivakkojoki Formation, occasionally mixed with flows of tholeiitic basalt and porphyritic andesite. The Hosko and Kuljunki Formations are composed of coarse clastic sediments with a few felsic pyroclastics, and turbidites in their lower sections. The conglomerate-dominated Tiittalanvaara Formation is characterized by a thin layer of mafic rock at its base that transitions upwards into iron-rich sediments overlapped by the mafic and ultramafic rocks of the Pampalo Formation (Sorjonen-Ward, 1993; O'Brien et al., 1993).

The central part of the HSB which involves the Pampalo Formation underwent a varying phase of volcanism that consisted of tholeiitic flows, volcanic breccia, as well as komatiite flows. Above these formations lies a thick layer of graywackes that is generally undifferentiated (Sorjonen-Ward et al., 2015; O'Brien et al., 1993).

In the southern part of the HSB, there are three formations that belong to the Hattu Supersequence, namely the Korvilansuo, Ukkolanvaara, and Naukulampi. The Korvilansuo turbiditic sediments overlie the banded iron formations of the Ukkolanvaara Formation. The Korvilansuo Formation consists mainly of graywackes that show extensive evidence of hydrothermal alteration. The Naukulampi Formation is structurally separated from the adjacent Ukkolanvaara Formation (Sorjonen-Ward, 1993).



2.2.3. Intrusive Units

The granitoid units of the belt have not been acknowledged as the basement for the Hattu Supersequence as their contacts are interpreted as intrusive or tectonic (Sorjonen-Ward, 1993). The intrusive units belong to the TTG group (tonalite-trondhjemite-granodiorite) and have penetrated the belt around 2.76-2.70 Ga. These are categorized into 3 distinct groups (O'Brien et al., 1993; Vaasjoki et al., 1993; Molnár et al., 2016)

The first group includes the Kuittila, Tasanvaara, and Korpivaara intrusions, all of which have tonalitic compositions. The Kuittila pluton exhibits a geochemical character that is typical for the Archean sanukitoids, and along felsic dikes indicate that they were not significantly influenced by older crustal material during their formation.

The second group comprises the Pogosta, Silvevaara, and Viluvaara plutons, which have granodiorite compositions and contain heterogeneous populations of zircons that suggest the involvement of older crustal rocks in their magma generation.

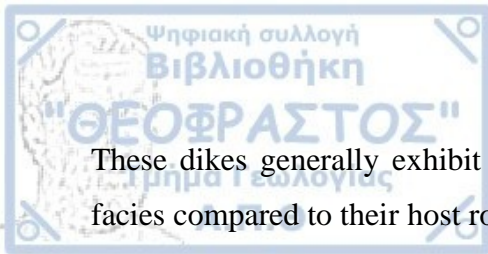
Finally, the third group comprises the Naarva and Lukanvaara leucogranites containing muscovite, biotite, and tourmaline, as well as garnet and mafic enclaves, indicating that partial melting of metasedimentary rocks played a significant role in their formation.

2.2.4. Structural Evolution

The HSB is characterized by upward-facing and steeply dipping structures that have been formed not by separate tectonic events but are the result of a continuous - progressive deformation (Sorjonen-Ward, 1993; Nurmi et al., 1993).

During the early stages of deformation tonalite and granodiorite intrusions were emplaced and produced antiform and synform structures with mostly vertical N-S axial planes (stage D1). A second deformation stage (D2) caused refolding events along the limbs of the previous folds, creating a series of synforms and antiforms, coaxial to the initial folds. The second stage was responsible for the development of more discrete shear zones and strike-slip duplexes in the area (Sorjonen-Ward et al., 2015).

All Archean rocks of the HSB are crosscut by NW-SW oriented dolerite dikes with ages ranging from 2.3 to 2.1 Ga. This incident is reviewed separately as a third stage (D3).



These dikes generally exhibit lower-grade metamorphic recrystallization in greenschist facies compared to their host rocks (Sorjonen-Ward, 1993).

The regional Paleoproterozoic Svecofennian orogenic event (1.8-1.7 Ga) has affected the HSB. Evidence of metamorphic overprint by the Svecofennian orogeny at 1840 Ma is present locally by greenschist facies mineral assemblages (Sorjonen-Ward 1993; Hölttä et al., 2016; Molnár et al., 2017).

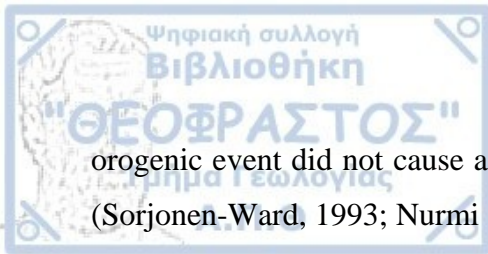
The current structural regime of HSB is marked by transpressional dextral shear systems trending in N-NE direction, in which the intrusions are positioned into dilatant sites and numerous distinct shear zones can be easily identified (Sorjonen-Ward and Luukkonen, 2005).

2.3. GOLD MINERALIZATION IN THE HATTU SCHIST BELT

2.3.1. Gold Occurrences

The gold occurrences of HSB share many similarities with typical Archean orogenic-gold provinces worldwide regarding the mineralization style, host rock lithologies and structural setting (Nurmi et al., 1993). The presence of gold through bedrock drilling has been confirmed to be present in almost all rock types of the HSB, suggesting that mostly the rheological-geochemical contrasts were crucial for directing fluid-flow interaction and gold deposition (Sorjonen-Ward et al., 2015). Economically valuable levels of gold, exceeding 1 ppm, can be found throughout the region indicating a significant event in the formation of gold deposits (Nurmi et al., 1993).

Intense hydrothermal alteration of country rocks culminated due to large-scale fluids concentrated into the shear zones (Kalliomäki et al., 2019). The alteration is evident along the belt in extensive zones which can range from tens to hundreds of meters wide and over 10 km long. The soil in these zones display elevated levels of gold, which extend over a distance of more than 40 km (Nurmi, 1993). Kojonen et al. (1993) stated that the primary ore depositional mechanism was the process of filling open spaces connected with strong hydrothermal metasomatic replacement that resulted in potassic alteration, silicification, carbonatization, tourmalinization and sulfurization. This hydrothermal ore alteration is not related to the doleritic dyke emplacement whereas the Paleoproterozoic



orogenic event did not cause any major ore re-distribution in the orogenic gold deposits. (Sorjonen-Ward, 1993; Nurmi 1993; Molnár et al., 2016).

Three major ore mineral assemblages dominate the HSB mineralization, though not all of them are found in every deposit. The first assemblage is an early Mo-W-(±Au) stockwork mineralization with molybdenite and scheelite as major minerals. This type is followed by a main, rich in Au-sulfide-telluride mineralization that occurs in quartz-carbonate veins. The third Au-telluride-sulfide-(±As) assemblage mostly occurs as disseminations in the mineralized altered host rocks (Kojonen et al 1993; Molnár et al., 2016; Fusswinkel et al., 2017).

Many gold prospects are found within greywackes and intermediate volcanics, interbedded with conglomerates, BIFs, and mafic to felsic volcanoclastics. Most if not all, these are aligned within high strain zones and close to the contact zones to granitoid intrusions (Nurmi et al., 1993; Sorjonen-Ward, 1993; Rasilainen, 1996).

Peak-metamorphic growth of garnet porphyroblasts and dynamic recrystallization of gold-bearing quartz veins occurred after gold mineralization and associated hydrothermal alteration (Sorjonen-Ward, 1993). Käpyaho et al., (2017) based on U-Pb geochronological data of hydrothermal zircons, support that gold mineralization occurred at 2.71 Ga post-dating most of the granitoids (2.75 Ga). The younger Naarva leucogranite (in northern HSB), dated at 2.70 Ga is the only intrusion that could have played a role in the orogenic gold of HSB, and potentially be interpreted as a contributor of magmatic fluids into the gold mineralizing hydrothermal system (Molnár et al., 2016).

Major and trace element tourmaline data from several deposits do not exhibit characteristics that would advocate for a magmatic contribution to the hydrothermal fluids. Ore fluid chemistry of the Pampalo deposit dispute the involvement of magmatic fluids and instead endorse a pure metamorphic devolatilization model (Fusswinkel et al., 2017).

According to Sorjonen-Ward 2015, the HSB can be separated into four distinct anomalous zones regarding the ore distribution, and the distinct geological and structural characteristics. From south to north, these zones include the Kuittila, Hattuvaara, Pampalo, and Hosko anomalous zones.

2.3.2. Kuittila Zone

The Kuittila zone can be further subdivided into the Kuittila-Kelokorpi prospects in the south and the Korvilansuo-Kivisuo-Elinsuo-Muurinsuo prospects in the north part. The name originates from the initial exploration trenches within the Kuittila tonalite intrusion where exposed quartz-veins and sericitic and carbonated shear zones were found to host gold, pyrite, molybdenite and scheelite. Further geochemical mapping and drill-core tests uncovered the presence of gold within the metasedimentary formations along the western boundary of Kuittila tonalite (Fig. 2.2). This zone exhibits extensive hydrothermal alteration and contains several distinct gold anomaly zones (Hartikainen and Nurmi, 1993; Sorjonen-Ward et al., 2015).

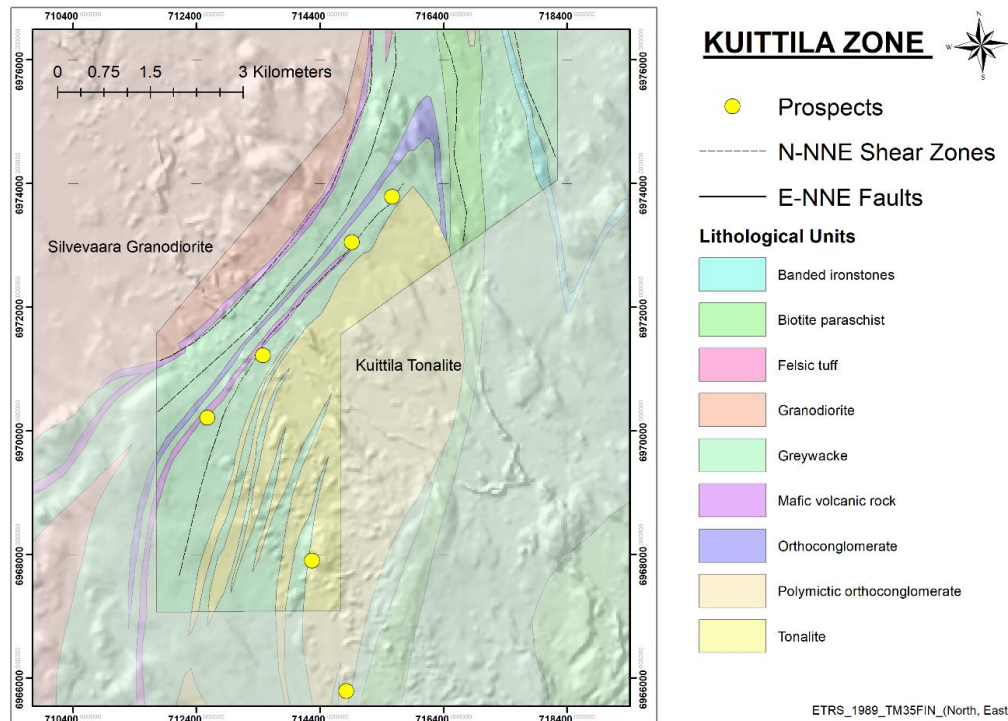


Fig. 2.2. The southern part of the HSB showing the prospects within the Kuittila ore zone; from north to south these are: Muurinsuo, Elinsuo, Kivisuo, Korvilansuo, and Kuittila.

At Kuittila prospect the gold mineralization is hosted within the tonalite expressed as a system of thin veins characterized by high concentrations of Mo, and W (Eilu, 2015). In drill core samples, the tonalite appears to be sheared across many meters in proximity with the quartz lodes, and is made up of minerals like sericite, albite, calcite, quartz, biotite, epidote, K-feldspar, and scattered iron sulfides. Gold exists in fine-grained form, with



particle sizes ranging from a few microns up to several tens of microns found as inclusions or intergrowths with pyrite, often associated with occasional tellurides (Kojonen et al., 1993).

At Korvilansuo and Kivisuo prospects gold mineralization is spread throughout silicified, chloritized and sericitized mica schist rocks, intruded by porphyritic and tonalite dikes. All lithologies are highly strained and locally ultra-mylonitic in texture and contain gold as scattered disseminations or within tourmaline-quartz veins (Sorjonen-Ward et al., 2015). The mineral assemblages contain mainly pyrrhotite, chalcopyrite, and pyrite, and gold is found mixed in with arsenopyrite and tellurides (Kojonen et al., 1993). Fine-grained native gold is frequently associated with Au-Ag-Bi-Pb tellurides and native bismuth (Nurmi et al., 1993).

The neighboring Elinsuo and Muurinsuo prospects are similar with host rocks involving strongly foliated mica schists with graywacke and mafic tuffitic layers. These are consistently altered to sericite and sericite-chlorite schists (Sorjonen-Ward et al., 2015). Gold is commonly found in association with various minerals such as bismuth, gold, and silver tellurides, with small amounts of arsenopyrite, chalcopyrite, pentlandite, and galena (Kojonen et al., 1993).

2.3.3. Hattuvaara Zone

Despite the discovery of sparse mineralized glacial boulders, the only confirmed gold deposit in the central part of the belt, in the Hattuvaara zone (Fig. 2.3.), is the Rämepuro deposit. It is located 8 km north of Muurinsuo (Nurmi et al., 1993). The ore is situated along the boundary between two distinct supracrustal units and a tonalite dike. Drilling conducted by Outokumpu in 1985-1987 and more recent work have confirmed that the mineralization extends for at least 500 meters along the strike (Pekkarinen, 1988; Endomines, 2014). The units to the west of the dike consist of well-preserved graywackes, featuring numerous intercalations of polymictic conglomeratic rocks (Ojala et al., 1990). On the eastern side of the dike, there is a prevalence of uniform, fine-grained intermediate schists that include thin BIF layers.

Gold is found within dynamically recrystallized quartz-tourmaline-sulfide veins. Native gold is fine-grained, in proximity to, between quartz and tourmaline grains, together

with pyrite, and lesser pyrrhotite, chalcopyrite and sphalerite, whereas metallic bismuth and hedleyite are characteristically present (Kojonen et al., 1993).

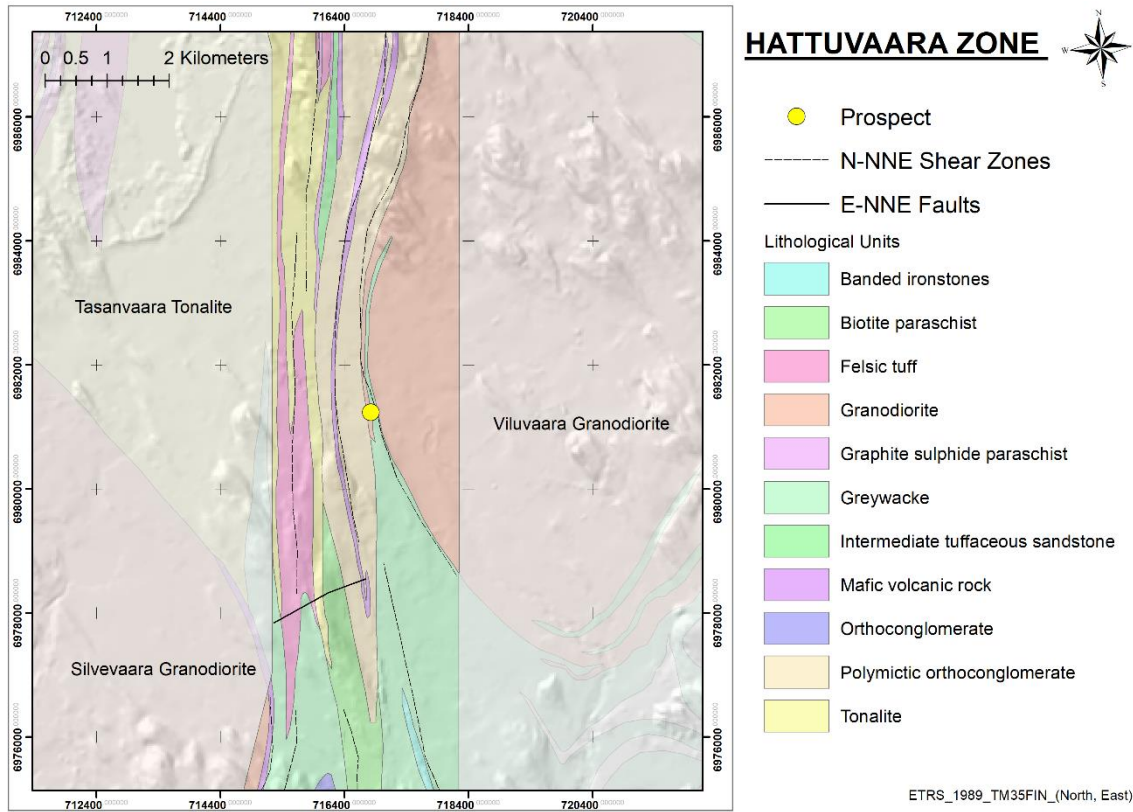


Fig. 2.3. The central part of the HSB showing the Hattuvaara ore zone that includes the single deposit of Rämepuro.

Rämepuro stands out among the limited occurrences of gold in the HSB as it does not display significant till anomaly patterns on geochemical maps, even with a high sampling density of 16 samples per square kilometer (Hartikainen and Nurmi, 1993; Hartikainen and Niskanen, 2001).

2.3.4. Pampalo Zone

The Pampalo ore zone is considered highly prospective and contains the active Pampalo mine. It is 1 to 2 km wide and is characterized by the presence of ultramafic rocks along much of its length (Fig. 2.4). This zone coincides with prominent Ni- and As-till geochemical anomalies (Nurmi et al., 1993). The Pampalo zone has a prominent

northwesterly orientation compared to the Hattuvaara zone and has been extensively researched due to its high gold potential. Several gold occurrences have been identified close to the Pampalo deposit, such as the Pampalo Northwest and Pampalo East (Nurmi et al., 1993).

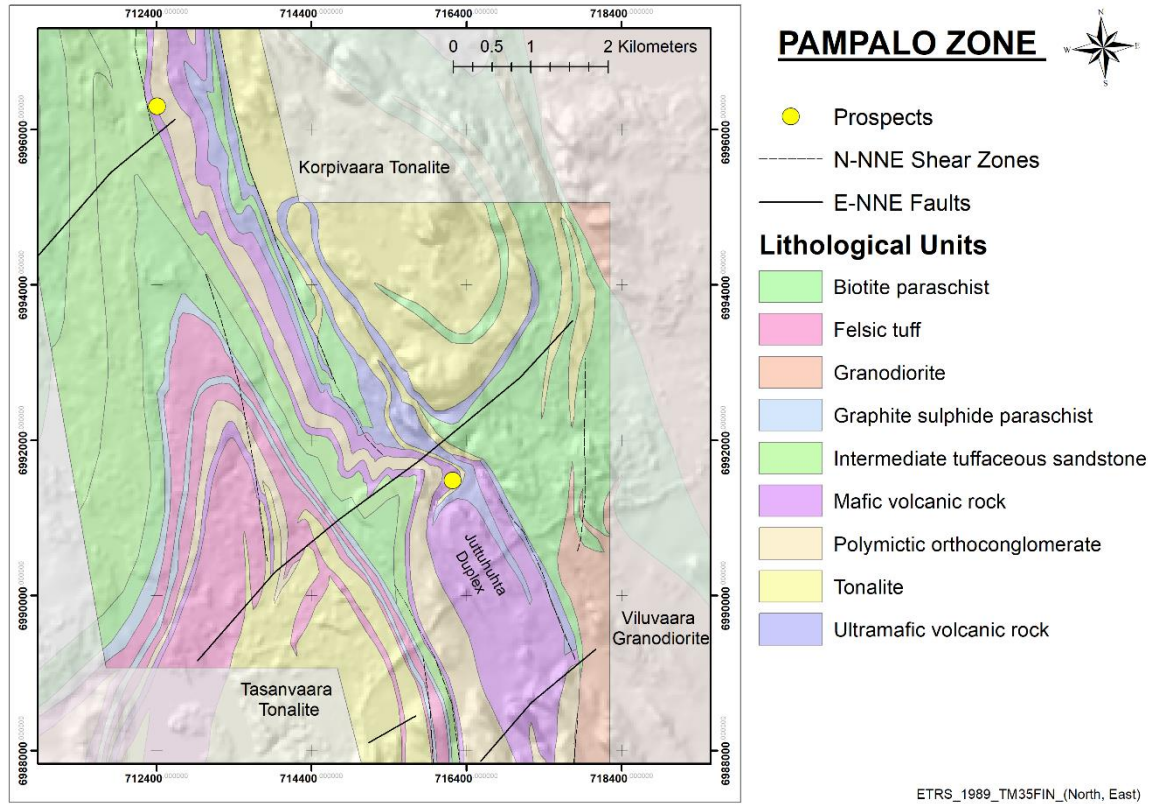


Fig. 2.4. The Pampalo zone is situated in the northern central part of the HSB and includes the prospects of Pampalo, Kuivisto and Korpilampi.

The ore mineralization runs in a northeastern direction in contrast to the prevailing northwesterly trend of the Pampalo zone. The stratigraphically lowest unit in the deposit area consists of turbiditic greywackes and conglomerates of the Tiittalanvaara Formation overlain or intercalated by banded iron formation (sulfide facies). The succeeding stratigraphic unit consists of metabasalts overlaid by an intermediate andesitic tuff which hosts the majority of the mineralization (Sorjonen-Ward, 1993).

Gold is dispersed along with pyrite in dynamically recrystallized veins and fractures in porphyritic dikes, which shows differing mechanical behaviors between the two rock

types. The presence of isolated mineralized quartz veins is uncommon, indicating that pervasive sulfidation of the surrounding rock has played a more significant role than fluid mixing or phase separation (Nurmi et al., 1993). The main sulfide minerals associated with gold are pyrite, along with smaller amounts of pyrrhotite, chalcopyrite, galena, and sphalerite. Other minerals such as bismuth and Pb-, Ag-, and Au-tellurides are also common (Kojonen et al., 1993). Scheelite serves as an indicator of presence of ore.

Two kilometers north of Pampalo, drilling over till geochemical anomalies has uncovered gold mineralization within the same formation in sericitized feldspathic greywackes. This discovery has led to the identification of the Kuivisto and Kuivisto East mineralized zones, characterized by steep-dipping mineralization zones that are concordant with the surrounding lithological units (Heino et al., 1995).

The Korpilampi prospect is located between Kuivisto and Pampalo. The rocks consist of talc-chlorite schists and ultramafic rocks with pegmatites that showed evidence of extensive tourmaline alteration with presence of sulfides (Sorjonen-Ward et al., 2015). Gold predominantly occurs with bismuth and other minerals like pyrite, pyrrhotite, marcasite, sphalerite, and chalcopyrite (Kojonen et al., 1993). The Korpilampi prospect still has potential due to the till geochemical anomalies found on both sides of the outcrop and its lithological similarities with the Pampalo deposit (Sorjonen-Ward et al., 2015).

2.3.5. Hosko Zone

This ore zone makes up the northernmost part of the study area and is structurally and due to the high abundance of arsenopyrite distinct compared to other zones. The host rocks are composed of thin to thick-bedded turbidites with dark pelitic intercalations that exhibit different degrees of sericitic alteration (Fig. 2.5). Tourmaline is widespread in mineralized veins and pervasive in the pelitic layers. Other minerals include pyrrhotite, marcasite, and scheelite (Heino et al., 1995; Käpyaho et al., 2013).

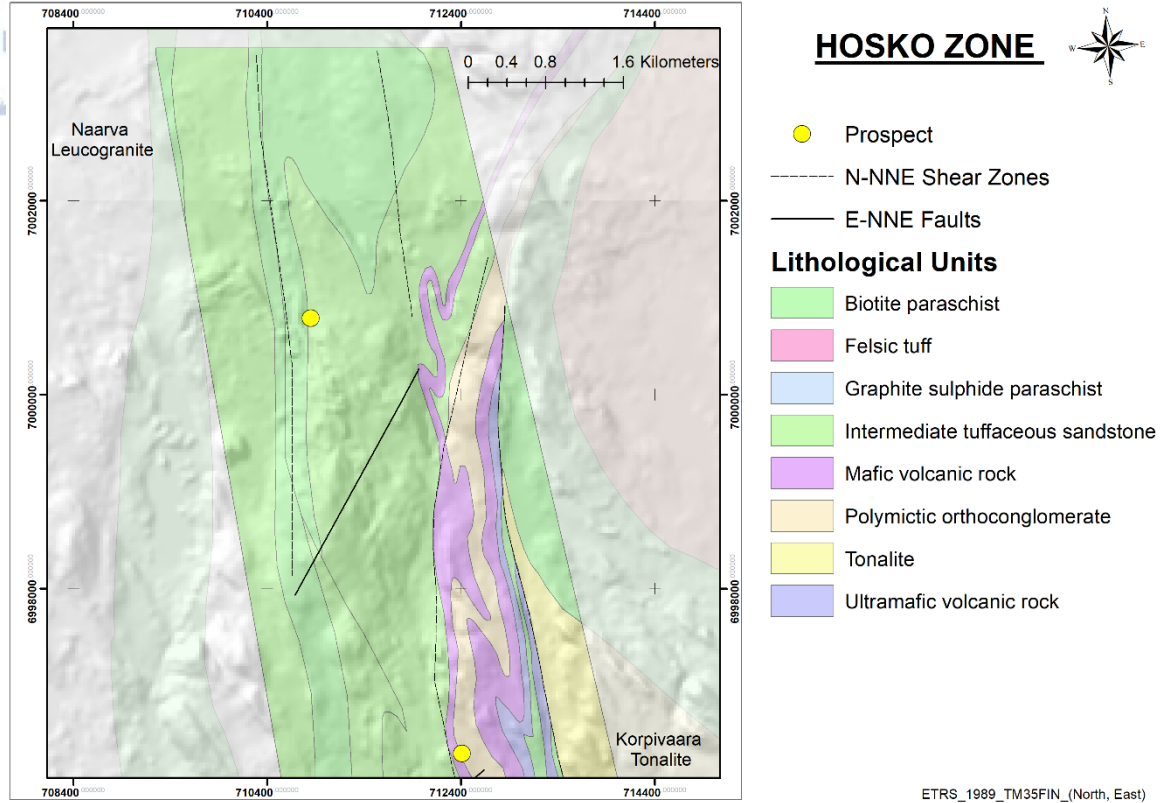


Fig. 2.5. The northern part of the Hattu Schist Belt including the Hosko deposit.

The mineralized area corresponds to a clear IP (inverse polarization) anomaly that can be followed southward from Hosko towards the Kuivisto deposit in the Pampalo area (Sorjonen-Ward et al., 2015). The gold reserves have been well established but due to the high nugget effect exploitation of the ore remains uncertain.



Chapter 3. Data and Software

Except of the base map which is obtained from the open-source data of the National Land Survey of Finland (NLS), all geospatial data used in this research work belong and were provided by the Endomines Oy company.

Endomines Oy is a Finnish mining and exploration company that operates in eastern Finland. Since February 2011, produces gold concentrate from the Pampalo underground mine. Exploitation by open pit mining of the adjacent Pampalo East deposit was initiated in January 2013. In September 2013, the company commenced open pit mining operations at the Rämepuro deposit, which is located approx. 15 km south of Pampalo. Initiation of mining operations at Hosko deposit (10 km north) is further planned. The plant capacity at the centrally located Pampalo plant is 420.000 tons and annual gold production is at 800 kg.

The Company's exploration program is focused on the Karelian Gold Line (KGL) where is the sole owner of a 40 km long, uninterrupted corridor of claim areas with mineral rights for 132 km² of claims & reservations (Fig. 3.1). The Karelian Gold Line is an almost linear, north-south trending, gold-hosting belt and covers the largest part of the Hattu greenschist belt, in Eastern Finland. It hosts an array of over 23 gold deposits and gold occurrences, including the active mines of Pampalo and Rämepuro.

All the available geological information is projected to the Finnish Coordinate Reference System, the ETRS_1989_TM35FIN_NE.

3.1. BASEMAP AND STUDY AREA

The study area is restricted into an elongated thin zone which extends from north to south approximately for 36 km and covers a major part of the Hattu schist belt. From east to west, the width of the zone averages at 3 km, while certain areas have a width up to 7.5 km (Fig. 3.1). The base map of the study area shown in Figure 3.1 includes a regional background map with the position of the villages and elevation contours with an interval of 10m.

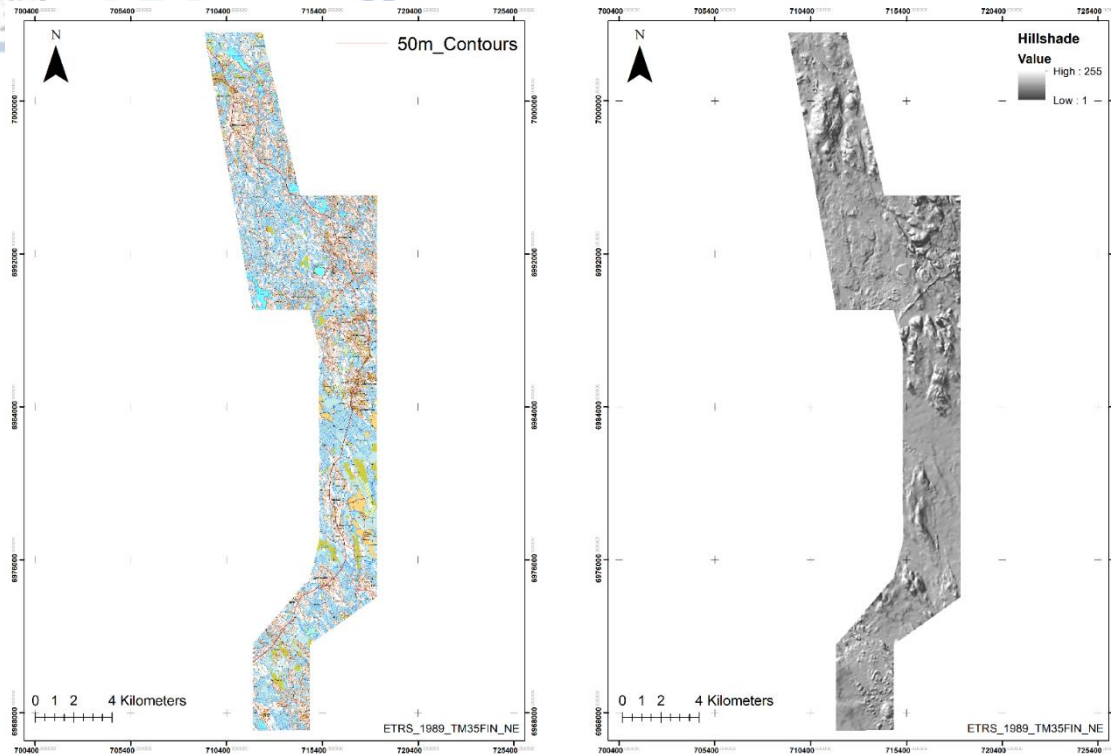


Fig. 3.1. The uninterrupted corridor of claim areas with mineral rights (study area) within the HSB owned by Endomines Oy. Shows the villages, the contours of 50 m and land cover (map obtained from the National Land survey of Finland).

The topography map includes a high-resolution hill shade map with a cell size of 4x4m for the study area. This map is the product of the analysis of an original DEM dataset map. The DEM data are the outcome from a geophysical survey over the study area conducted in 2011 by SkyTem for Endomines company (Fig. 3.1).

The resulting topographical dataset is a combination of three individual raster type files of 1-meter accuracy, and a vector type file of a 10-meter elevation interval of digitized contours. According to the map, the area features a smooth topography characterized by undulating terrain that is mainly defined by several lakes and swamps, situated at a base level of 145 m a.s.l. The elevation differences generally fall within the range of 30 to 75 meters with the highest point (283 m a.s.l.).

3.2. LITHOLOGY

The lithological formations of the study area were digitized in GIS and were clipped for the extent of the study area (Fig. 3.2). The lithological contacts were extracted based on small-scale geological maps included in the book of Nurmi et al. 1993 that were scanned for this task. The occurring 7 lithological formations and the 4 different intrusive rocks were digitized into a vector map. The lithologies are classified based on the two principal types of the belt, namely the Hattu Supersequence (e.g. Pampalo, Hosko or Korvilansuo Formations) and the distinct intrusion types (e.g. granodiorites, tonalites).

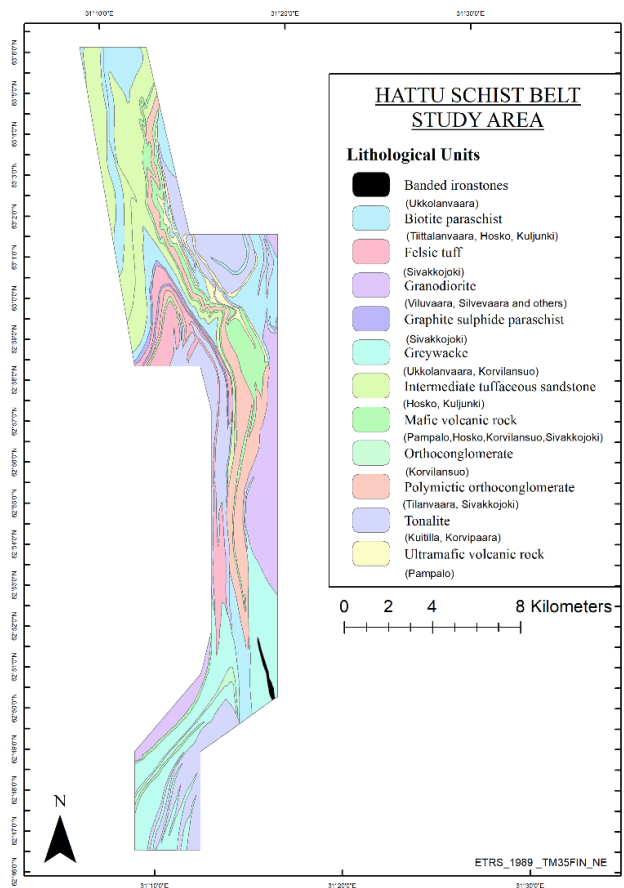


Fig. 3.2 The lithological map of the study area showing the 7 different lithologies of the Hattu Supersequence and the 4 intrusive rocks (map after Nurmi et al., 1993).

3.3. GEOCHEMISTRY

Two geochemical datasets were produced and made available by Endomines Oy; One includes gold concentrations from till (soil) samples, and the second from rock surface samples and projected to surface drill core gold data (Fig. 3.2). To this database the geochemical data from the publication of Nurmi et al. 1993 were depicted and added, as well as, from the open access database available at: https://hakku.gtk.fi/fi/locations/search?location_id=13.

The geochemical datasets were initially in Excel format presented as X, Y, and Zi values, where X and Y refer to longitude and latitude coordinates, while Zi refers to gold concentrations (in parts per million, ppm) at those coordinates. These data were stored in GIS as data layers (vector maps) of points with attribute table. The initial soil dataset contains in total 936 data points, while the lithology dataset contains 716 data points (Fig. 3.3).

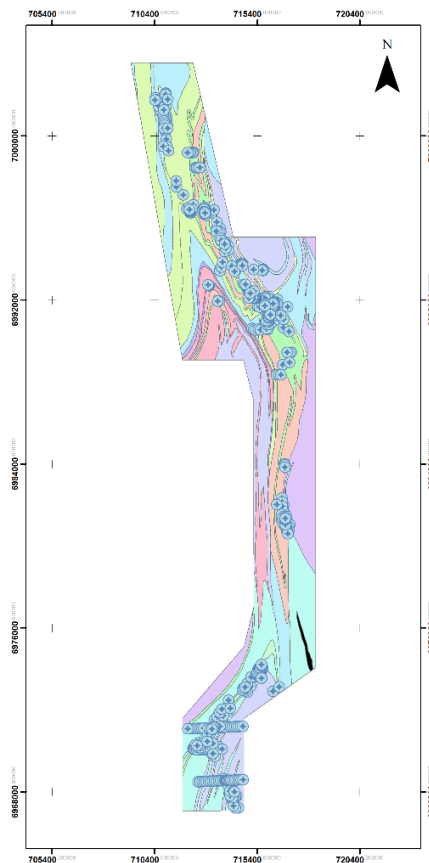


Fig. 3.3. The location of the soil and rock gold-geochemical samples from the study area.



3.3.1. Soil Samples

Till sampling was performed at three different scales in the belt. Initial low-resolution sampling on a regional scale with one composite sample per 16 km² for gold Au and one sample per 3-4 km² for Au (and other metals) in the Hattu schist belt by the GTK in the 1980's. Further, on a more local level with 16 samples per km² (by the GTK) and thirdly on a prospect level with varying density by Endomines company (Fig. 3.3). For the prospect-scale sampling (average depth of 5.6m), geochemical traverses were mainly conducted with the purpose of determining the most advantageous sites for drilling within anomalies that had been observed in prior larger sampling scales.

The samples from Endomines Oy were analyzed by the Fire assay method. Most of gold contents from the samples of GTK were quantified utilizing an atomic absorption spectrometer with a graphite furnace (GAAS). This study examines the gold content in units of parts per million (ppm), and the established minimum level of detection for the rock type is 0.0001 ppm.

3.3.2. Rock and drillcore samples

The drill-dataset contains 870 drill holes. The dataset is originally divided into 4 individuals excel type files, namely the collar, survey, lithology and assay files, each one containing information on hole-ID, coordinates, maximum and minimum depths, drill type, azimuth, dip, lithology and concentration of gold. This specific dataset is used for constructing the 3-D model of belt.

Surface rock samples from outcrops were collected by GTK and by the Endomines staff, either by hammer or by shallow diamond drilling. The samples were analyzed using the same method as for the soil samples. The detection limit for the lithology is set at 0.001 ppm.

3.4. AIRBORNE MAGNETICS

The study area's dataset includes an aeromagnetic geophysical tilt derivative map in a raster format with cell size of 15x15 m (Fig. 3.4).

Briefly, the tilt derivative (TD) could be described as a geometrical function of the vertical $\frac{d(F)}{d(Z)}$ and horizontal $\left(\frac{d(F)}{d(x)}\right), \left(\frac{d(F)}{d(y)}\right)$ derivatives of the total field F, which have values ranging between positive and negative $\pm\pi/2$. The TD as normally calculated is given by:

$$TD = \tan^{-1} \left\{ \frac{dF}{dZ} / \sqrt{\left(\frac{dF}{dx}\right)^2 + \left(\frac{dF}{dy}\right)^2} \right\} \quad (1)$$

This filter function is used for improving the identification of structural trends and lineations in magnetic grids (Stewart and Miller, 2018).

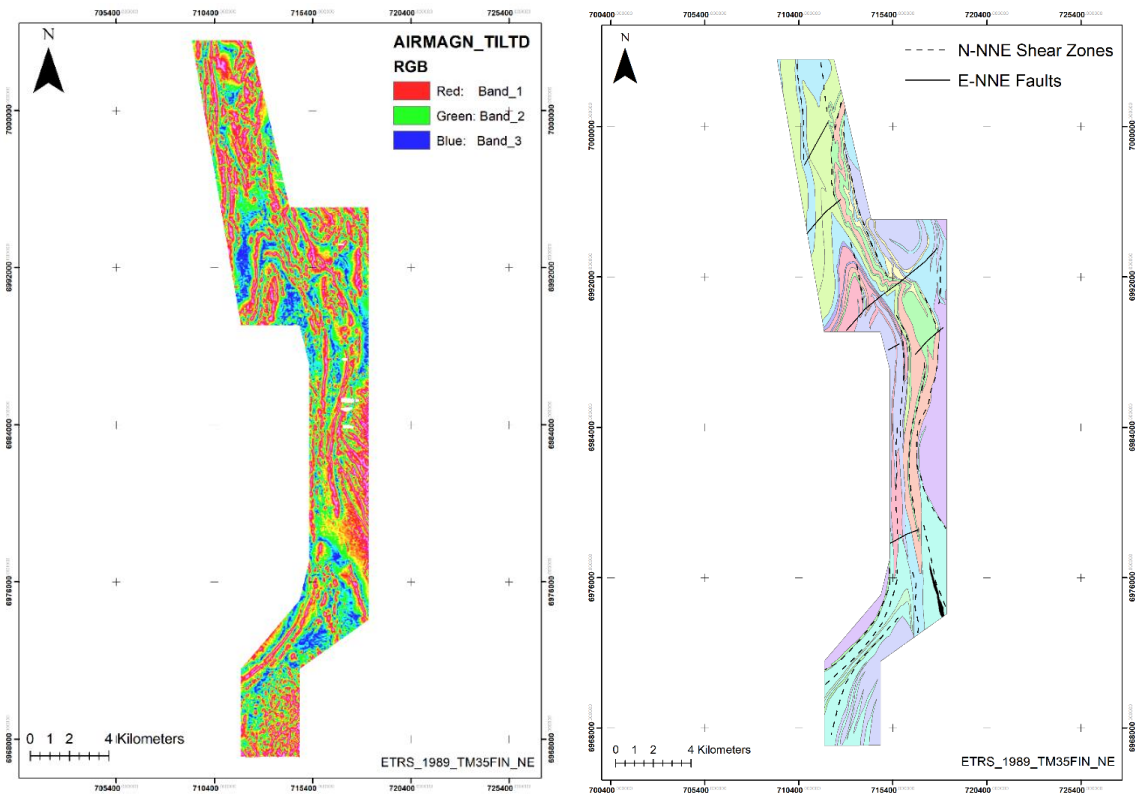
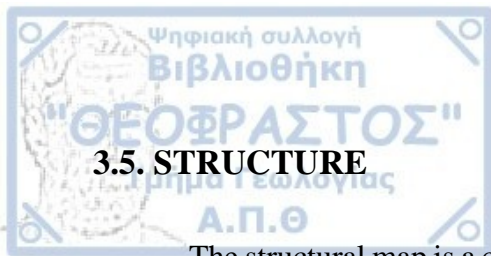


Fig. 3.4. Aeromagnetic geophysical tilt derivative map and the structural map showing the major N-NNE shear zones and secondary E-NNE normal faults.



3.5. STRUCTURE

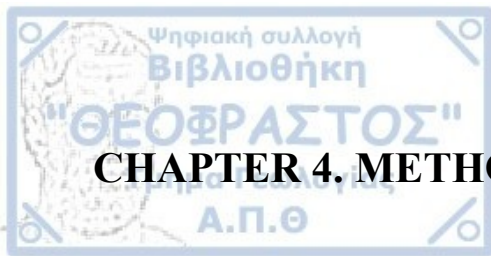
The structural map is a combination of structural work from Sorjonen-Ward (1993), Nurmi et al. (1993), and unpublished report from Sakellaris (2016). The structures were identified by field work, and interpretation of geophysical topographical and geological maps. The main structural features used for this study include the N-NNE shear zones and the E-NNE faults.

3.6. SOFTWARE

Three licensed software are used for the completion of the research. The primary statistical analysis of the gold concentration datasets was conducted using IBM SPSS Statistics 27.0. Computing descriptive statistics, histograms, Q-Q plots and boxplots, data transformation-inverse transformation and threshold estimation were some of the procedures carried out by SPSS.

The geospatial dataset was plotted and processed in the ArcMap 10.8.1 GIS software by ESRI. With the use of Spatial Analyst tool - Geostatistical Analyst, the interpolation methods of Inverse Distance Weighting (IDW) and Ordinary Kriging (OK) were done.

The third used-software was the Maptek Vulcan 2021.3 software, designed for 3D mine planning and geological modelling. The GIS geological information along with the drill hole data were imported into Vulcan for the construction and visualization of the 3D geological model.



CHAPTER 4. METHODOLOGY

4.1. TERMINOLOGY OF GEOCHEMICAL ANOMALY MAPPING

4.1.1. Background and Threshold Values

One of the fundamental tasks in using geochemical data for mineral exploration is to recognize and delineate geochemical anomalies from the background values. In geochemistry, the standard concentration of an element within a specific lithology is referred to as geochemical background value (Hawkes and Webb, 1962; Reinmann and Garrett, 2005). The background value is usually defined as a range of values rather than a single value because the distribution of any element in a lithological unit is often not uniform and can vary from one region to another, and from one type of material to another. The highest value within the range of background values is known as threshold value (Garrett, 1991).

4.1.2. Geochemical Anomaly Values

Anomalies in element concentrations (i.e. gold, silver, lead etc.) may suggest the presence of a potential deposit. The content above the threshold value is referred as geochemical anomaly (Hawkes and Webb, 1962). Traditional methods of modeling geochemical anomalies can be divided into two categories: i) analyzing frequency distributions of uni-element concentrations (Levinson, 1974) and ii) analyzing multi-element associations using multivariate statistical methods (Rose et al., 1979). A common statistical technique for estimating threshold values is the use of the mean plus or minus twice the standard deviation ($\text{mean} \pm 2\text{SDEV}$), and the method assumes that the data being analyzed are independent and follows a normal distribution.

4.1.3. Outlier Values

A typical gold-geochemical dataset consists of numerous small concentrations interspersed with a few extremely large ones, referred to as outliers (Reimann and Filzmoser, 2000).

4.2. STATISTICAL ANALYSIS OF GOLD CONCENTRATIONS

The flowchart in Figure 4.1 illustrates the overall procedure followed to produce accurate geochemical gold anomaly maps for the study area from different databases (soil, rock) by applying different interpolation methods.

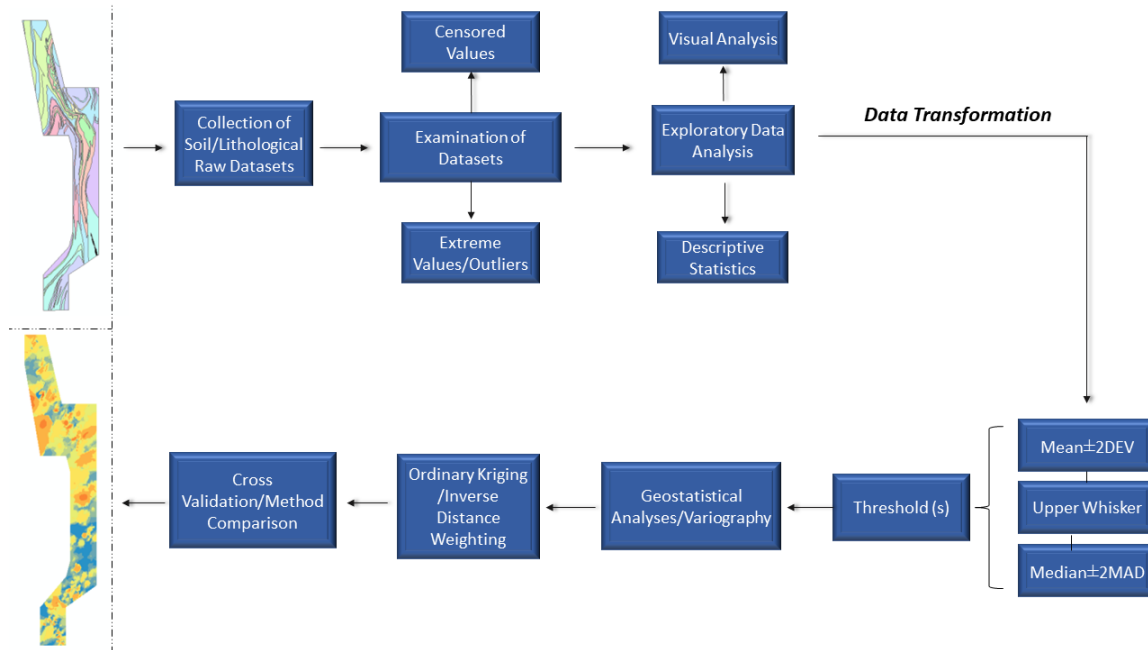


Fig 4.1. Flowchart that illustrates the methodology used to generate the geochemical map(s) for the Hattu Schist Belt. Most of these steps can be applied for mapping geochemical anomalies, with the flexibility to explore alternative methods for determining thresholds (Exploratory Data Analysis) and employing various interpolation techniques (Ordinary Kriging and Inverse Distance Weighting) for producing the final spatial distribution maps.

4.2.1. Exploratory Data Analysis

The concept of Exploratory Data Analysis (EDA) was proposed in the late 1970s, and it is a technique for examining and interpreting univariate data that does not adhere to a normal distribution model (Tukey 1977; Chambers et al., 1983; Kürzl, 1988; Reimann et al., 2005). It comprises a set of techniques that use descriptive statistics and graphical tools to uncover patterns, identify important variables, detect outliers and anomalies, generate hypotheses, develop models, and ultimately guide the interpretation and treatment of the

data. Unlike traditional methods, this method does not rely on assumptions about the data distribution model but instead uses the data itself to define statistics and identify outliers (Carranza, 2009).

4.2.2 EDA Graphical Tools

EDA utilizes graphical methods that are commonly used in conjunction with a histogram and include the boxplot, Quantile-Quantile (Q-Q) plots, one dimensional scatter plots and density traces. Combining a histogram (Fig. 4.2. a) with EDA graphics provides a more comprehensive understanding of the data than a histogram alone.

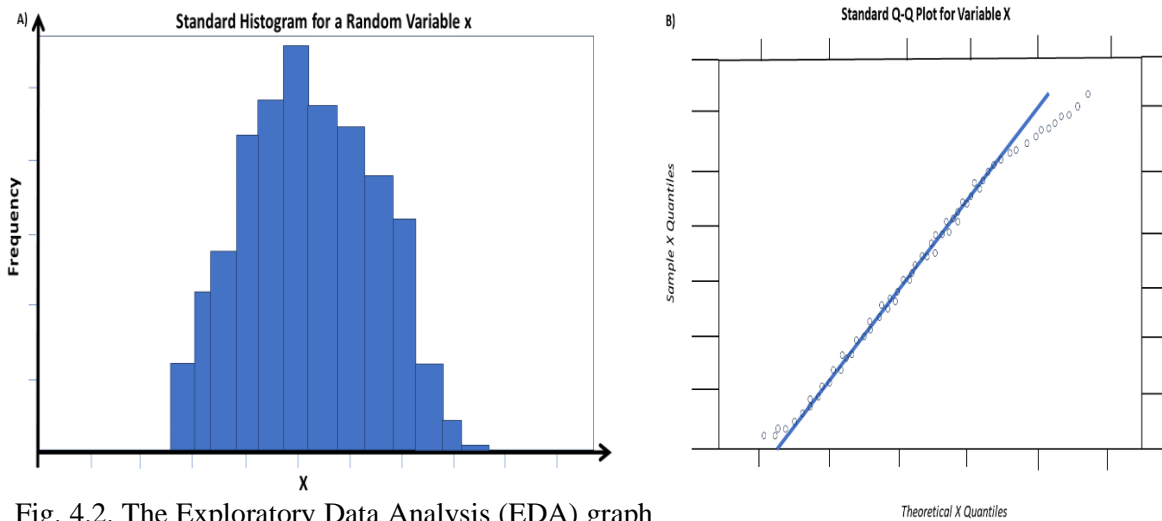


Fig. 4.2. The Exploratory Data Analysis (EDA) graph plot (Fig. 4.2 b).

In a standard Q-Q plot, the closer the data points are to the 45-degree line, the more closely the data resembles a normal distribution (Fig. 4.2. b). It can reveal outliers and identify anomaly in the data that may not be immediately apparent from a histogram. It can also be used to establish the classes (Kürzl, 1988).

4.2.3 Boxplot

A boxplot is a graphical representation of a dataset (Fig 4.3) and is created by ordering the data values from the smallest to the largest (Kürzl, 1988). The boxplot is capable of clearly displaying information describing the key characteristics about the central tendency, spread, and other characteristics of a univariate data set and is probably the most useful tool in geochemical data analysis. The median value is calculated by counting halfway through the univariate dataset from the smallest to the largest or vice versa, dividing it into two equal parts. When the median is positioned at the center of the boxplot, it indicates a normal distribution and, if the median is located far from the center, it suggests that the distribution is skewed (Carranza, 2009).

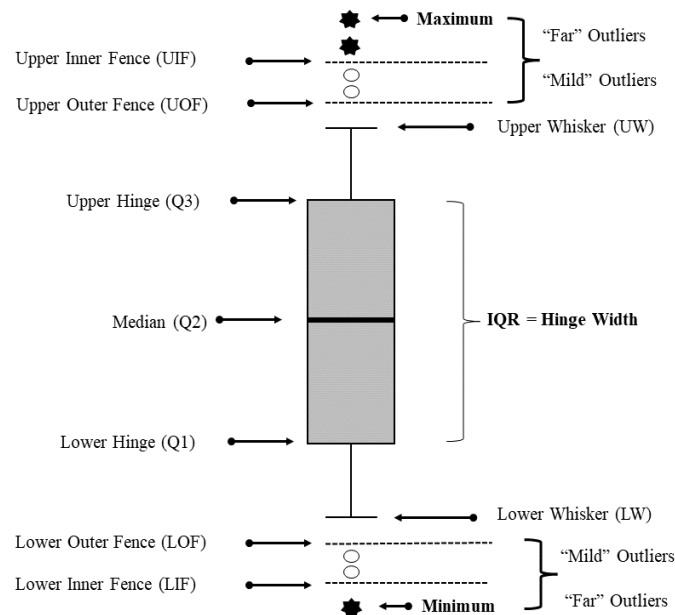


Fig. 4.3. Schematic representation of a boxplot along with its features illustrating the most significant characteristics for a univariate data set.

As seen in Fig. 4.3 it illustrates five of the most important statistical values, namely the median of distribution, the minimum and maximum value of a dataset, the lower and upper hinge (LH-UH). In a boxplot, the outliers do not significantly impact the median, the hinges or the inner fences. This makes it resilient and robust when it comes to extreme outliers in a univariate dataset (Carranza, 2008; Nazarpour et al., 2015).



The lower hinge (LH) and upper hinge (UH) values are determined by counting halfway from the minimum to the median and from the maximum to the median, respectively. These values, along with the median, divide the dataset into four approximately equal parts called quartiles. The 1st quartile (Q1) consists of values from the minimum to the lower hinge, the 2nd quartile (Q2) from the lower hinge to the median, the 3rd quartile (Q3) from the median to the upper hinge, and the 4th quartile (Q4) from the upper hinge to the maximum.

With the quartiles calculated it is possible to calculate the interquartile range (IQR) or hinge width (1). In a dataset, the IQR is a measure of statistical dispersion that represents the range between the first quartile (Q1) and the third quartile (Q3) and can be represented as the difference between the values at the LH and UH (Reimann, 2005; Shuguang et al., 2015).

$$\text{Interquartile Range (IQR)} = \text{Lower Hinge (LH)} - \text{Upper Hinge (UH)} \quad (2)$$

The lower inner fence (LIF), the lower outer fence (LOF), the upper inner fence (UIF) and the upper outer fence (UOF), and their values (X) can be estimated as:

$$X(\text{LIF}) = X(\text{LH}) - (1.5 * \text{IQR}) \quad (3)$$

$$X(\text{LOF}) = X(\text{LH}) - (3 * \text{IQR}) \quad (4)$$

$$X(\text{UIF}) = X(\text{LH}) + (1.5 * \text{IQR}) \quad (5)$$

$$X(\text{UOF}) = X(\text{LH}) + (3 * \text{IQR}) \quad (6)$$

The values (X) of the lower whisker (LW) and the upper whisker (UW) features can be determined from these two last equations (Carranza, 2009).

$$X(\text{LW}) = \min[X\{X > X(\text{LIF})\}] \quad (7)$$

$$X(\text{UW}) = \max[X\{X < X(\text{UIF})\}] \quad (8)$$

The values that exceed the inner fences are classified as outliers and are presented separately from the rest of the dataset, enabling the application of parametric statistical testing (Harris et al., 2001). Values falling between the inner and outer fences are labeled as 'mild' outliers, while values surpassing the outer fences are classified as 'far' or extreme outliers, denoting highly uncommon values (Kotz and Johnson, 1985).

4.2.4 Dealing with censored-extreme (outliers) values

Addressing outlier values involves their removal or replacement and can prevent the underestimation of the overall descriptive statistics. Censored values, which refer to values falling below the analytical detection are usually removed, especially if they represent a single population (Grünfeld, 2005; Carranza, 2009). Generally, if the number of samples containing values below the lower detection limit becomes substantial, it indicates that the detection limit is set too high to obtain trustworthy data, thus is recommended to exclude these samples from the statistical analysis (Rawlings et al., 2002).

Extreme values should be handled with similar approaches. In data analysis, the decision about removing or replacing the outliers is challenging, as it requires making decisions that potentially could remove valuable information. The initial consideration involves how to distinguish the unusual outliers and those that are characteristic of geochemical patterns and the second to determining the appropriate number of outliers that need to be eliminated from the dataset (Grünfeld, 2005).

According to various methodologies in regional geochemical data, geochemical values exceeding 97.5% are generally considered to deviate from the natural geochemical baseline (Rawlings et al., 2002). Traditional approaches in handling outliers deal with the identification and removal of specific samples with the highest concentrations. Geostatistical tools like variograms can be used to identify errors and unusual outliers (Grünfeld, 2005).

4.2.5. Threshold value estimation with EDA statistics and boxplot

A number of statistical methods exist for choosing threshold levels and to detect outliers (Hawkes and Webb 1962). For instance, the 90th, 95th or 98th percentiles are considered to represent the threshold value and all values greater than thresholds indicate geochemical anomalies (Ander et al., 2013; Wilde et al., 2004; Reinman and De Caritat, 2017).

In EDA, the mean absolute deviation (MAD) is similar to the standard deviation, therefore, the threshold of median +2MAD is analogous to the threshold of mean + 2SDEV. The mean absolute deviation can be calculated by taking the median of the absolute



differences between each data value (X_i) and the median of the data itself as shown below (Tukey, 1977).

$$MAD = \text{median}\{|X_i - \text{median}(X_i)|\} \quad (9)$$

If the nature of the individual uni-element data sets is right-skewed, the mean-2SDEV and the median -2MAD may contain predominantly negative values. The negative values indicate that the mean and median estimates in the raw uni-element data sets are statistically insignificant. As a result, using the mean $\pm 2SDEV$ and by extension the median $\pm 2MAD$ as a threshold for estimating geochemical anomalies can result in misleading models and would not yield meaningful results (Carranza, 2009). The median $\pm 2MAD$ method does not rely on assumptions of normality; however, asymmetric distributions require applying appropriate transformations to the data should exhibit a more symmetrical distribution before utilizing any threshold estimation techniques (Reimann et al., 2005).

Except EDA statistics, threshold values can be defined through the boxplot. By examining the boxplot, it is possible to categorize a geochemical data set into five distinct groups. (1) The exceptionally low background values ranging from the minimum value to the Lower Whisker, (2) The low background values ranging from Lower Whisker to Lower Hinge class, (3) The background values which belong to the Lower Hinge–Upper Hinge class, and the following (4) high background values which refer to the Upper Hinge-Upper Whisker class. Outliers that fall beyond the Upper Whisker indicate anomalies (Carranza 2009). In various circumstances the upper inner fence (UIF) is commonly used as the threshold to distinguish the background and anomalous values (Bounessah and Atkin, 2003; Reimann et al., 2005), whereas the Upper Outer Fence (UOF) can also serve as an alternative threshold (Yusta et al., 1998).

According to Reimann et al. (2005) the boxplot function provides the most valuable information when the actual number of outliers is less than 10%. In practical applications, utilizing the boxplot as an initial step for class selection and visualizing spatial data structure has proven to be a highly effective tool for identifying the significant geochemical processes underlying a data distribution. If the proportion of the outliers exceeds 15%, only the median +2MAD method will yield satisfactory results, until the point where the outlier population begins to dominate the dataset.



4.2.6. Data transformations

Various numerical transformation functions can be utilized in order to lessen skewness characteristics and decrease the distribution asymmetry (Miesch, 1977; Garrett et al., 1980; Joseph and Bhaumik, 1997). There are several recommended transformations available for this purpose such as i) Additive log-ratio (alr) (Aitchison, 1986), ii) Centered log-ratio (clr) (Aitchison, 1986) and iii) Isometric log-ratio (ilr) (Egozcue et al., 2003). Despite these, it is often challenging to achieve the ideal distribution for geochemical data, and particularly when applying the median +2MAD method. (Vural, 2019). Once the dataset transformation has been applied, resulting in a dataset that exhibits distributions that are more symmetrical than the raw dataset, the estimated threshold values of mean $\pm 2SDEV$ and the median $\pm 2MAD$ methods are applicable for use in generating geochemical maps (Carranza, 2009).

4.3. SPATIAL PREDICTION

Spatial interpolation is used in a variety of fields and involves using the data from known geographical locations to estimate the values at unknown locations achieving the creation of a continuous-data surface. Spatial analysis is typically done using a Geographic Information System (GIS) which offers several geoprocessing tools. There are two main categories of interpolation methods: the deterministic and the geostatistical (Fig. 4.4).

4.3.1. Deterministic methods

Deterministic methods like Inverse Distance Weighting (IDW) or Radial Basis Functions generate surfaces from observed data points, either by calculating the extent of similarity or the degree of smoothing. Similar methods are triangulated irregular network (TIN) global and local polynomial interpolations. The deterministic methods can be further separated into two categories. Global methods involve using the entire dataset to calculate predictions, whereas local methods focus on the measured points within specific, smaller areas within the larger study region.

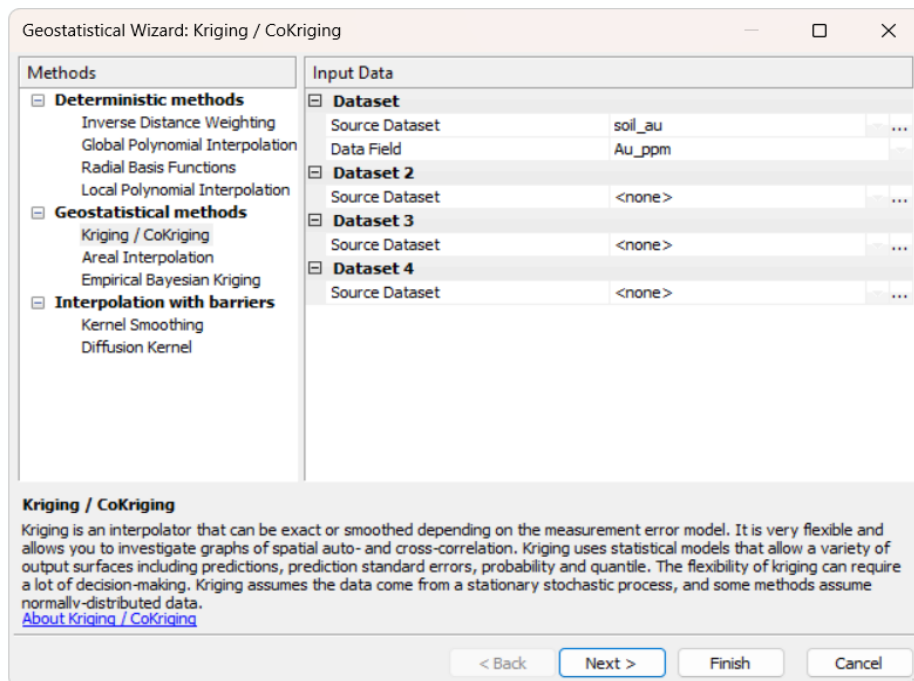


Fig. 4.4. The Geostatistical Analyst/Geostatistical Wizard tool in ArcGIS 10.8.1 showcasing the available interpolation methods, including Kriging and Inverse Distance Weighting.

4.3.2 Inverse Distance Weighting (IDW)

The Inverse Distance Weighting (IDW) interpolation probably represents the earliest spatial prediction technique and is considered as the most straightforward deterministic interpolation method (Shepard, 1964, 1968). The process of IDW interpolation involves estimating values at locations that were not sampled by assigning weights to the known values of nearby sampled points within a specified distance. The general formula for IDW interpolation is (Johnston et al. 2003; Robinson and Metternich, 2006):

$$\hat{Z}(x_0) = \sum_{i=1}^N \lambda_i Z(x_i) \quad (10)$$

Variable \hat{Z} is the seeking predicted value for the location (x_0), variable N refers to the quantity of observed data points around the predicted location. The weights assigned to each observed point are denoted as λ_i and Z is the observed value at a given location (x_i).

IDW interpolation operates on the assumption that the measured values nearest to the predicted location exert a more significant influence on the predicted value than those located at a greater distance. The algorithm assigns weights to these points based on their distances from the predicted location, giving higher weights to points that are closer (Li and Heap 2008; Zhang 2023). The equation used to determine the weights for the interpolation is:

$$\lambda_i = \frac{d_{i0}^{-p}}{\sum_{i=1}^N d_{i0}^{-p}} \quad (11)$$

In this equation, the quantity d_{i0} represents the distance between the predicted location $\hat{Z}(x_0)$ and each of the measured locations $Z(x_i)$. The weights assigned to the measured locations, which will be utilized in the prediction, are adjusted proportionally to ensure that their cumulative sum equals 1.

$$\sum_{i=1}^N \lambda_i = 1 \quad (12)$$

The IDW method relies on two crucial parameters that significantly impact its accuracy: the power parameter (p) and the number of neighbors (Burrough and McDonnell, 1998; Zhang et al., 2011). As the distance between the measured sample locations and the prediction location increases, the weight assigned to each measured point in the prediction decreases exponentially. The rate at which weights decrease with distance depends on the specific value of p (Xie et al., 2011). For instance, if $p = 0$ (Fig. 4.5), there is no decrease in weight with distance, resulting in equal weights for each point. When the value of p increases, the weights assigned to distant points decrease rapidly, however, if p is too high, only a small number of nearby points will have a significant impact on the prediction.

In the Geostatistical Analyst tool, the power parameter the default value is $p=2$, and there is no standard theoretical value (Johnston et al., 2003). It is important to thoroughly investigate the results and examine the validation statistics with the objective of minimizing the error as much as possible.

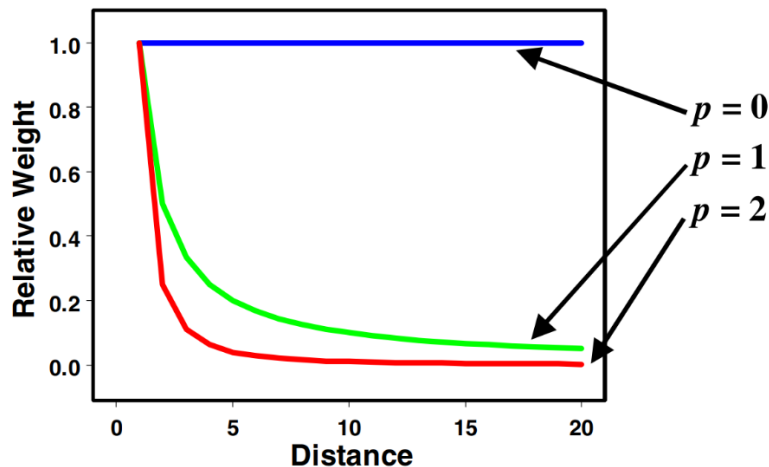
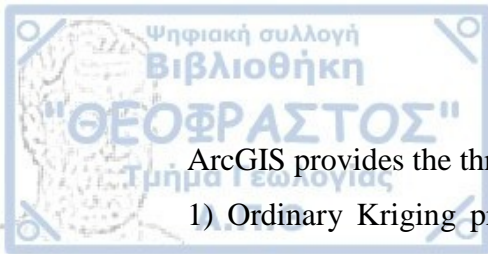


Fig. 4.5. The figure represents visually the variations in the power parameter for three different scenarios: $p=0$, $p=1$, and $p=2$. It also showcases the gradual decay of relative weights as the distance increases (modified after Johnston et al. 2003).

If there is a directional influence, it should be considered in the analysis. For the IDW method, directional influence in the data can be attributed to various factors such as geological structures. In such cases is advisable to adjust the shape of the neighborhood to resemble an ellipse with the major axis aligned parallel to those structures (Johnston et al., 2003). In ArcGIS, it is also crucial to determine the maximum and minimum number of neighbors to use and choose which of the 4 neighborhood distinct sectors (one sector, 4 sectors, 4 sectors with 45 and 8 sectors) is the most optimal. There is no universally accepted standard for determining the optimal parameters in this context (Xu and Zhang, 2023).

4.3.3 Geostatistical Methods

The term Geostatistics also known as 'kriging' originate from the French mathematician G. Matheron and South African mining engineer D.G. Krige, who developed an optimal interpolation procedure based on regionalized gold concentrations for application in gold mining. Geostatistical techniques are based in the principles of statistical spatial autocorrelation. They are applied when the variation within the samples is too large to be modeled by deterministic methods. An additional advantage is that these contain an estimate of the interpolation error (Burrough and McDonnell, 1998).



ArcGIS provides the three most common kriging methods:

1) Ordinary Kriging produces interpolation values by assuming a constant but unknown mean value, 2) Simple kriging produces interpolation values by assuming a constant but known mean value, and 3) Universal Kriging produces interpolation values by assuming a trend surface with unknown coefficients.

4.3.4. The essential assumptions of Random Variables and Stationarity

Random function is a collection of random variables or regionalized variables (i.e. gold content) that are defined within a specific spatial domain (Deutsch, 2003). The assumption of stationarity forms the foundation of geostatistics and allows to handle data as if they exhibit consistent levels of variation across the region of interest. The observed outcomes are treated as if they arise from correlated random processes, assuming stationarity. The random process can be represented using the model

$$Z(x) = \mu + \varepsilon(x) \quad (13)$$

The process can be described by μ , which represents its mean, while the $\varepsilon(x)$ is a random variable with an average of zero and covariance.

Variation is often considered as second-order stationary and can be represented using covariance functions. A covariance function typically decreases as the distance between locations increases (Fig. 4.6.), reflecting a decrease in similarity or correlation, and it provides information about how the values of the random process vary with spatial separation.

$$C(h) = E\{\varepsilon(x)\varepsilon(x+h)\} \quad (14)$$

This is equivalent to saying that the given equation is the same as

$$C(h) = E\{[Z(x) - \mu] [Z(x+h) - \mu]\} = E\{[E(x)] [Z(x+h)] - \mu^2\} \quad (15)$$

In this case, h means lag distance, $Z(x)$ and $Z(x+h)$ represent the values of the random variable Z at locations x and $x+h$, respectively. The term "E" refers to the expectation. The covariance between these values is dependent solely on the parameter h

and varies exclusively with h . The underlying assumption for this is the concept of second-order stationarity (Fig. 4.6).

Alternatively, the concept of a slightly weaker assumption of intrinsic stationarity (Matheron, 1963) allows for a more comprehensive analysis using the variogram (Fig. 4.7) as a tool and not covariance to describe the spatial variation. In this scenario, the expected differences are assumed to be zero.

$$E \{Z(x) - Z(x + h)\} = 0 \quad (16)$$

The covariance among the residuals is substituted with the variance of the differences as a measure of spatial relationships.

$$\text{var} \{Z(x) - Z(x + h)\} = E[\{Z(x) - Z(x + h)\}^2] = 2\gamma h \quad (17)$$

In this context, the semivariance is represented by $\gamma(h)$ at a specific lag h , and can be considered as the variogram when viewed as a function of h . The variogram depends on differences and its local validity is established by the equation (17) which makes the variogram function more generally useful than the covariance function (Oliver and Webster, 2015).

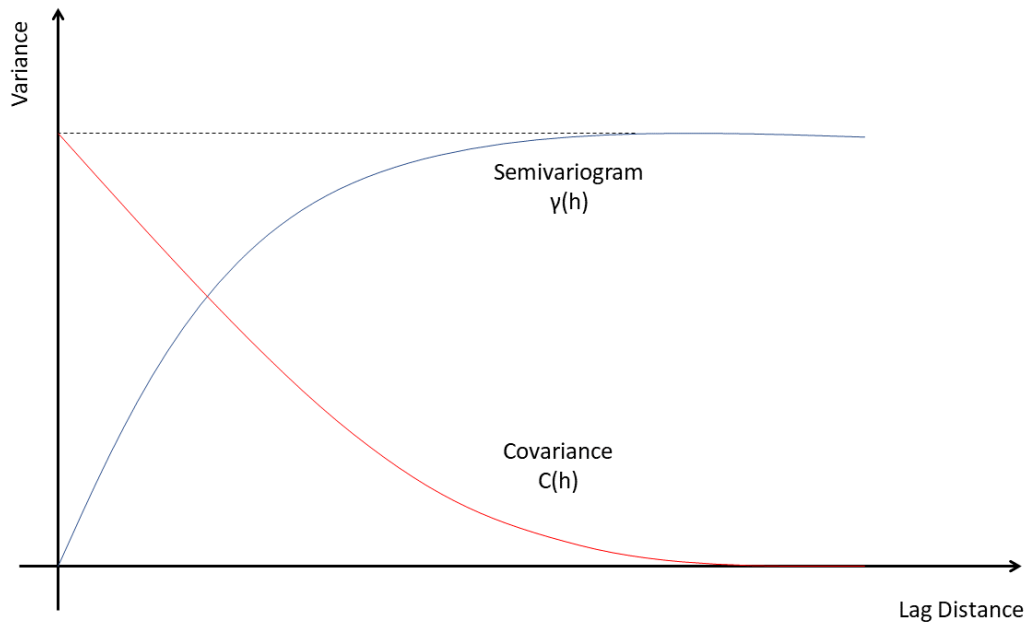
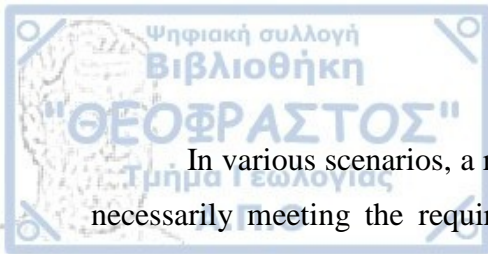


Fig. 4.6. The Covariance ($C(h)$) and Semivariance ($\gamma(h)$) functions as they vary with increasing lag distance, along with the relationship between these two functions.



In various scenarios, a random function can fulfill the intrinsic hypothesis without necessarily meeting the requirements of second-order stationarity (Myers, 1989). The intrinsic hypothesis is not only more general than second order stationarity, but it is also independent of the value μ , where the covariance function is relying on it and separate estimation is required which introduced bias (Myers, 1989; Bårdossy, 1997). Apart from these advantages, this study will focus on the variogram function as it is also more commonly used and applied in geochemical exploration.

To conclude, geostatistical analysis is approached with two primary methods. The variogram or covariance is modeled to investigate the spatial autocorrelation of the data and, kriging is later utilized to forecast values at unsampled locations (Johnston et al., 2003).

4.3.5. The Experimental Variogram

The term "variogram" is used to refer to the graph that shows the experimental or theoretical spatial variability of a particular attribute. It describes the mathematical function, denoted as $\gamma(h)$, that characterizes the semivariance between pairs of data points at varying distances or lags (h).

The commonly used equation for calculating the variogram is the method of moments (MoM) estimator (Matheron, 1965) and depends on the spatial arrangement of the geochemical data.

$$\hat{\gamma}(h) = \frac{1}{2m(h)} \sum_{i=1}^{m(h)} \{z(x_i) - z(x_i + h)\}^2 \quad (18)$$

The $z(x_i)$ and $z(x_i + h)$ represent the observed values of z at random places x_i , $x_i + h$, while $m(h)$ denotes the number of paired comparisons at a specific lag distance h . By varying the lag h , we can generate a sequence of semi variances $\gamma(h)$ in a specific order, which form the experimental or sample variogram.

In figure 4.7 it is apparent that there is an upper limit referred to as the sill variance, towards which the values of x approach asymptotically. This indicates that at greater distances, there is no spatial correlation observed between the points.

The range of spatial correlation is the limit where the spatial correlation reaches zero, indicating the point at which autocorrelation no longer exists. The curve of variogram increases until it reaches the sill, where it reaches its maximum value at a distance defined by the range. This curve represents the spatial dependence between points and indicates the range within the differences between points are correlated.

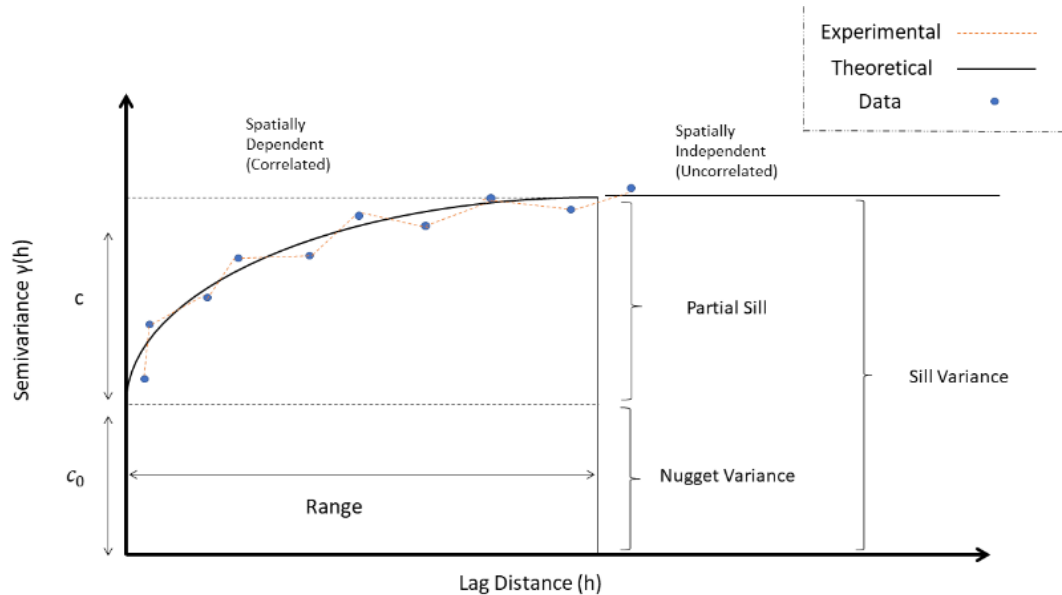


Fig. 4.7. The figure showcases the fitting of a theoretical variogram to an experimental variogram, highlighting the most significant parameters and characteristics of the variogram.

The variogram typically approaches a positive intercept at the y-axis, called the nugget variance. When the lag distance is zero, ideally the semivariance should also be zero. The term "nugget" was derived from gold mining, where it describes the occurrence of gold nuggets in a random and independent manner. These nuggets signify a disruption in the pattern of variation and represent an uncorrelated component. This means that the gold content at a particular site is not influenced by the gold content at nearby sites, indicating a lack of spatial correlation (Oliver and Webster, 2015).

If the variogram exhibits a horizontal line, indicating only nugget variances, it suggests the absence of spatial autocorrelation. Conversely, if the variogram displays widely scattered dispersion values, it indicates that the estimation of the parameter "c" was based on a small sample size, which is going to be explained in detail in factors.

4.3.6 Factors that affect the Experimental Variogram

The accuracy of the variogram relies on the sufficient amount of data at an appropriate density or interval. Variograms computed on small sets of data are unreliable, so the sample size but also the sampling interval play a vital role in the accuracy of a variogram (Webster and Oliver, 1992).

The selection of lag and sampling interval can significantly impact the quality of a variogram. If the selection of the lag interval is false, the variogram will fail to capture the correlated structure and therefore cannot sufficiently describe the spatial variation. Generally, if the lag interval surpasses half of the range or effective range of variation, it is probable that the resulting variogram will appear flat (Oliver and Webster, 1987).

If a geochemical dataset deviates significantly from a near-normal distribution, with a skewness coefficient exceeding the limits of ± 1 due to a long tail, may lead to erroneous variography results. Hence, it is needed to apply data transformations (Webster and Oliver, 2015). Kerry and Oliver (2007a) conducted a study that focused on how different levels of skewness and sample size influence. When utilizing a sample size of 1,600 data points and more on a 5-meter grid, the impact of increasing asymmetry on the variogram's shape was relatively minor, even when the skewness value reached up to 5.

The variogram is extremely sensitive to outliers since these influences the average values (Tukey, 1977). It is recommended to exclude outliers before calculating the variogram, and due to the fact that this recommendation assumes that the outliers are randomly distributed, they will not be included for subsequent kriging analysis (Kerry and Oliver 2007a).

Regarding data transformation, it is advisable to utilize the original data, even if its distribution is not normal and that the accuracy of estimates using the original non-normally distributed data was found to be higher compared to estimates using normally distributed data (Goovaerts, 1997).

Spatial variation can exhibit different patterns and magnitudes in different directions, indicating anisotropy (Fig. 4.8). In the case of an anisotropic process, variogram estimates can be computed in different directions by selecting specific directions and averaging the lag distances (h) that are sufficiently apart within the chosen direction and

the variogram displays significant changes in the direction of range or sill (Mory and Deutsch, 1989; Isaaks and Srivastava, 1989).

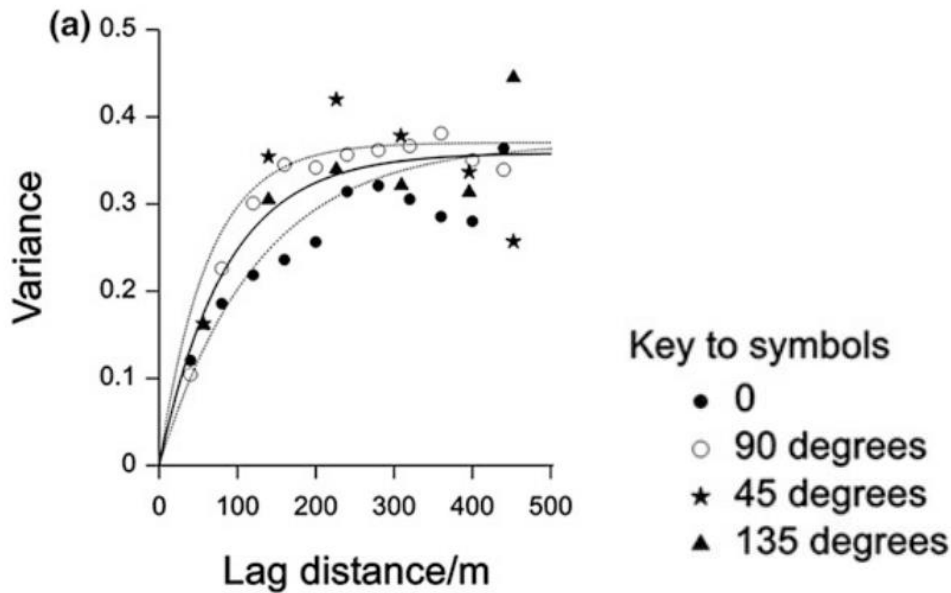


Fig. 4.8. Experimental variograms in four different directions (0, 45, 90 and 135 degrees) to investigate the presence of anisotropy.

Zonal anisotropy occurs when there are preferentially oriented zones with different means, leading to changes of the variation as the direction changes (Bardossy, 1997). This directional impact can be taken into consideration and examined in ArcGIS, by enabling the option of search direction tool to analyze the differences. The variogram can be examined separately in each principal direction, however, it does not affect the final output (Johnston et al., 2003). The determination of these directions considers the azimuth and dip angles, which are determined based on the geological characteristics of the area (Deutsch, 2015).

The selection of lag parameters, such as lag spacing and tolerance, is based on the domain size and data spacing, while the choice of angle tolerances and bandwidths considers the variability in calculation directions and the sampling configuration. All these parameters, including lag parameters, angle tolerances, and bandwidths (Fig. 4.9), are combined to establish the final definition of the variogram in a specific direction.

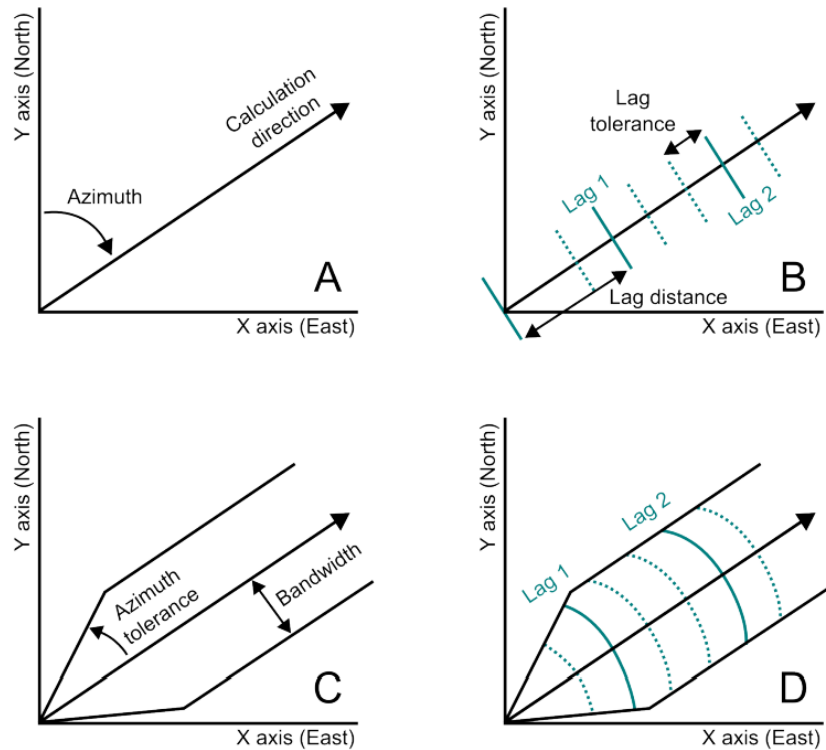


Fig. 4.9. Illustration of the typical tolerance parameters for experimental variograms (Deutsch 2015).

A trend represents a smooth and systematic nonrandom variation. A trend can manifest as regional variation, meaning it is consistent across the entire area of interest, or as local variation, occurring from one point to another within the region. If the presence of trend is confirmed, the variogram deviates from being solely determined by a random variable and as a consequence, this violates the assumption of stationarity. The data should be then analyzed by applying basic linear and quadratic polynomial fitting on the coordinates (Oliver and Webster, 2015).

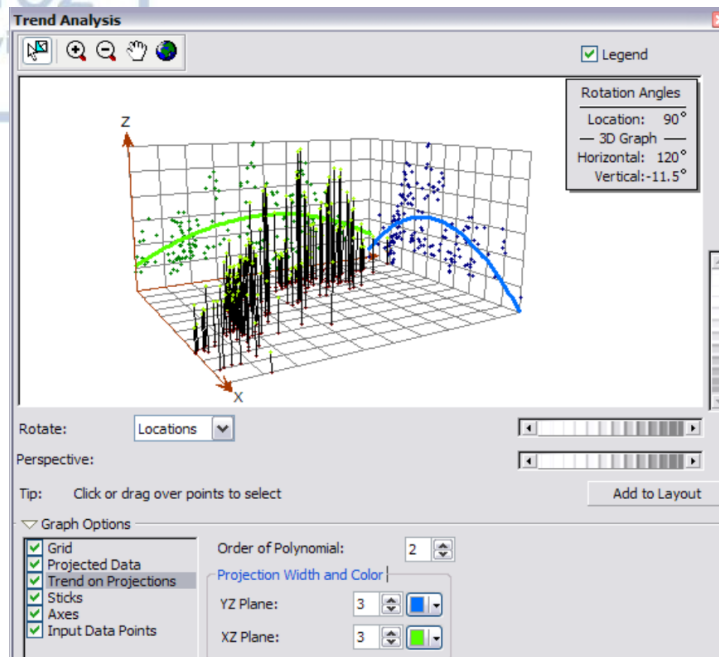


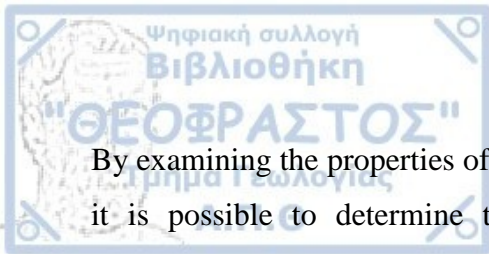
Fig. 4.10. Trend analysis conducted in ArcGIS using the Trend Analysis tool. The curved lines represent the projection data points indicating the existence of a discernible trend (Johnston et al., 2003).

In ArcGIS, trend in data can be analyzed using the trend analysis tool (Fig. 4.10). The points of the data are projected as lines and if the line remains constant in any direction (e.g. N-S or E-W), it suggests that there is no discernible pattern or a noticeable trend in the data (Johnston et al., 2003). For instance, if a curve or shape resembling a parabola is observed, it would indicate a second-degree trend (Biernacik et al., 2023). In this case, it can be eliminated by employing polynomials of various orders, such as constant, 1st, 2nd, or 3rd order trend removal.

4.3.7 Variogram models

The process of fitting the experimental variogram to a theoretical one requires a combination of knowledge, experience, and statistical techniques.

Theoretical variogram models include the spherical, exponential, linear and Gaussian models (Fig. 4.11). The selection of these different models is not a subjective or arbitrary task, but rather follows specific mathematical assumptions (Isaaks and Srivastava, 1989).



By examining the properties of the variogram such as the sill, range, and nugget variance, it is possible to determine the most suitable model (Cressie 1993; Burrough and McDonnell, 1998).

i) Spherical Model:

$$\gamma(h) = \begin{cases} c_0 + c\{3h/2r - 1/2(h/r)^3\} & \text{for } 0 < h \leq r \\ c_0 + c & \text{for } h > r \\ 0 & \text{for } h = 0 \end{cases}$$

When the nugget variance is significant but not excessively large, and there is a distinct range and sill, the spherical model often provides a good fit to the variogram curve.

ii) Exponential Model:

$$\gamma(h) = \begin{cases} c_0 + c\{1 - \exp(-h/a)\} & \text{for } h > 0 \\ 0 & \text{for } h = 0 \end{cases}$$

When there is a noticeable nugget and sill, but the range gradually increases, the exponential model is favored.

iii) Gaussian Model:

$$\gamma(h) = \begin{cases} c_0 + c[1 - \exp\{-(h/a)^2\}] & \text{for } h > 0 \\ 0 & \text{for } h = 0 \end{cases}$$

If the variation is exceptionally smooth and the nugget variance is significantly smaller compared to the random spatial variation, the variogram is often best fitted by a curve that exhibits an inflection point, such as the Gaussian model.

iv) Linear Model:

$$\gamma(h) = (c_0 + c) + \beta h$$

In these models, c_0 is defined as the nugget variance, c represents the variance of the spatially correlated component. The combination of $c_0 + c$ is called sill variance. The range parameter, denoted as r , while a is the distance parameter that represents the spatial lag or distance between pairs of observations. Finally, b is the slope parameter in linear model (Oliver and Webster, 2015).

The aforementioned models are referred to as "transitive" variograms since the spatial correlation structure changes with the distance, h . On the other hand, "non-transitive" variograms do not exhibit a sill within the sampled area and can be represented better by the linear model (Koutsopoulos, 2017).

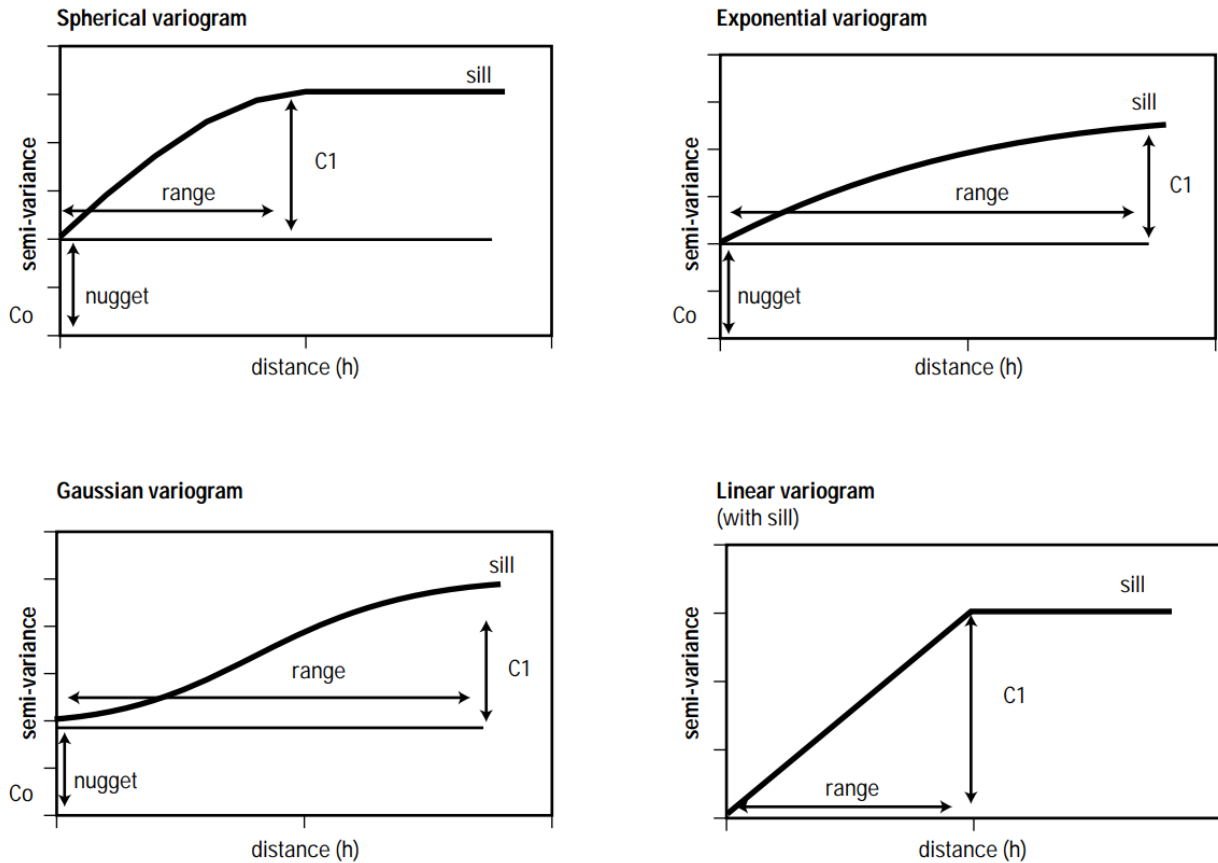
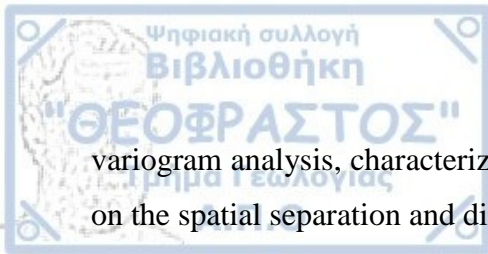


Fig. 4.11. The most commonly used variogram models (Hartkamp et al., 1991).

4.3.8. Ordinary Kriging

Kriging is commonly known as the Best Unbiased Linear Estimator (B.L.U.E.). Kriging uses a stochastic model of continuous spatial variation to make predictions at unvisited locations based on limited sample data. It accomplishes this by considering the spatial variation information represented in the variogram or covariance function (Oliver and Webster, 2015).

One commonly used form of Kriging is known as Ordinary Kriging (OK) is the most popular and widely used form of kriging due to its simplicity and capability of providing accurate estimations in various scenarios by relying solely on the measurements and their geographic coordinates. OK is founded on the assumption that variability follows a random and spatially correlated pattern, and that the underlying random process follows the intrinsic stationarity. These assumptions align with the fundamental principles of



variogram analysis, characterized by a consistent average and a variance that relies solely on the spatial separation and direction between locations (Oliver and Webster, 2015).

The prediction of the value $Z^*(x_0)$ at an unmeasured point x_0 in the spatial domain is achieved by estimating it as a linear combination of the observed values (e.g. x_1, x_2, \dots, x_i) and it is presented in concise and straightforward description of OK using the following formula (Isaaks and Srivastava, 1989; Cressie, 1993).

$$\hat{Z}(x_0) = \sum_{i=1}^N \lambda_i z(x_i) \quad (18)$$

Where, $Z^*(x_0)$ refers to the estimation or prediction of the value at the unmeasured position x_0 in the spatial domain and $Z(x_i)$ represents the value that has been measured or observed at a specific position x_i . Next, the λ_i are the coefficients that determine the weight or influence of each measured position x_i on the prediction at the unmeasured position x_0 . The weights are set to sum to 1 in order to guarantee accuracy in the estimate. Finally, the n denotes the number of positions within the nearby neighborhood that are considered when making the prediction (Hengl, 2007).

4.3.9. Results Quality and Validity Assessment of IDW/OK Analyses

Prior to creating a final interpolation surface, it is essential to assess the accuracy of the model in predicting values at locations that are unknown or not previously observed. One common way to achieve this is by predicting values using an independent set of sampling points.

An alternative is to perform model comparisons in order to assess the performance and suitability of OK method. Cross-validation allows for efficient evaluation of models without the need for an independent set of sampling points. Cross-validation utilizes the entirety of the available data to estimate models. It systematically eliminates each data location, one at a time, and predicts the corresponding data value using the remaining points (Johnston et al., 2003). The Geostatistical Analyst tool in ArcGIS offers this cross-validation feature and allows to compare various models and choose the most suitable by utilizing these performance indicators.

The comparison is between the kriged values ($\hat{Z}(x_i)$) with the observed values ($z(x_i)$) in a number of observations N and $\hat{\sigma}(x_i)$. The $\hat{\sigma}(x_i)$ represents the standard error of prediction for the location x_i and can be evaluated by utilizing estimation quality

statistics of Mean Error (ME), Root Mean Square Error (RMSE), Mean Standardized Error (MSE), Root Mean Square Standardized Error (RMSSE) and the Average Standard Error (ASE) (Johnston et al. 2003).

$$ME = \frac{1}{N} \sum_{i=1}^N z(x_i) - \hat{Z}(x_i) \quad (19)$$

$$RMSE = \sqrt{\sum_{i=1}^N \frac{(\hat{Z}(x_i) - z(x_i))^2}{N}} \quad (20)$$

$$MSE = \frac{\sum_{i=1}^N (\hat{Z}(x_i) - z(x_i)) / \sigma^{\wedge}(x_i)}{N} \quad (21)$$

$$RMSEE = \sqrt{\frac{\sum_{i=1}^N \{(\hat{Z}(x_i) - z(x_i)) / \sigma^{\wedge}(x_i)\}^2}{N}} \quad (22)$$

$$ASE = \sqrt{\frac{\sum_{i=1}^N \sigma^{\wedge}(x_i)}{N}} \quad (23)$$

The ideal scenario is for the ME to be zero, which indicates that Kriging is unbiased. Similarly, the objective is to reduce the ASE to the greatest extent possible, however, none of them are as effective at differentiation as the RMSEE and RMSE. Ideally, the squared errors should be equal to their respective kriging variances, resulting in an RMSEE of 1. Additionally, if ASE is closely aligned with the RMSE, it is inferred that the model accurately assesses the variability in predictions. If ASE is less than RMSE, it suggests an underestimation of prediction variability, and vice versa. As an alternative, if RMSE is greater than 1, the variability may be characterized as underestimated, while if it's less than 1, it could be considered overestimated (Johnston et al., 2003). For OK, the assessment of spatial autocorrelation can be further characterized based on the nugget to sill ratio. If the ratio is less than 0.25, it is considered high, if it fell between 0.25 and 0.75, it is deemed medium and if it exceeded 0.75, it is regarded as low (Cambardella et al., 1994).

The validation procedure for IDW is also straightforward, similar to the original implementation of the method. The Geostatistical Analyst tool in ArcGIS provides two performance indicators, namely ME and RMSPE, to assess the performance of the IDW interpolation method (Johnston et al., 2003) The RMSPE in IDW is equivalent to the RMSE in OK. To prevent terminology misunderstandings, the term RMSE will be consistently used throughout. Similar to OK, it is desirable for the ME and RMSE metrics



to be as close to zero as possible, with the RMSE being the most valuable and reliable diagnostic for the IDW interpolation.

In addition to the earlier validation diagnostics, another valuable and powerful approach for assessing the reliability of the final geochemical anomaly map(s) is to cross-reference it with well-established gold occurrences in the study area. This method allows for evaluating how well the geochemical anomalies indicated by the map align with these known occurrences.

4.3.10. Interpolation Map

The final step is to visualize the results of the variography or the IDW interpolation and produce a surface of predicted values. The final output for each method in ArcGIS is a raster database type geochemical anomaly map that needs visual adjustments to improve the cartographic representation of the data, as well as further refinement and processing of the classification results based on threshold values. Then, it is be feasible to compare the distribution results of the different interpolation methods and determine if one performs better than the other based on the available data and knowledge.

4.4. 3-DIMENSIONAL MODELLING

4.4.1. Explicit and implicit modelling techniques

Geological processes occur in a 3-D environment and early attempts of 3-D mapping involved the interpretation of stacked geologic sections as shown in Fig. 4.12 (Zhu, 1997). Examining these cross-sections collectively provides only a limited visual understanding of the 3-D layout of important geological features.

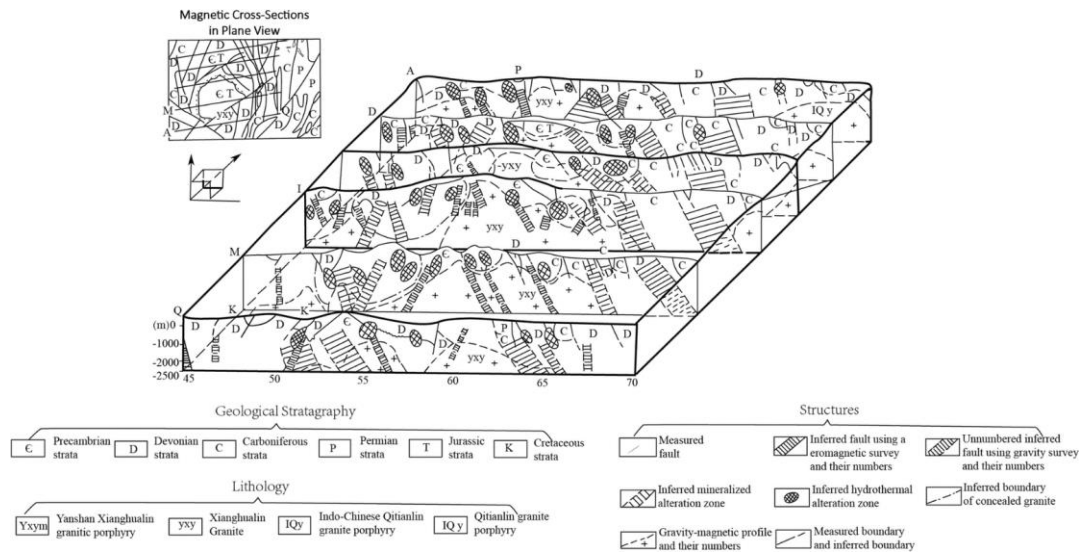
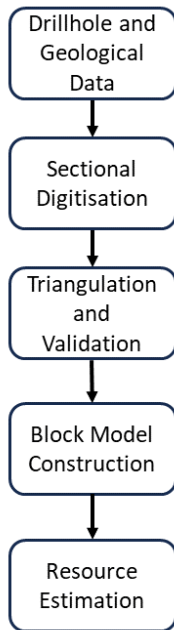


Fig. 4.12. A traditional approach to 3D prospectivity mapping that relies on the use of intersecting cross sections (Zhu 1997).

In 3-D modeling, two main approaches are primarily employed (Fig. 4.13) termed as explicit and implicit modelling techniques (Cowan et al., 2003). 3-D explicit modeling, which is often referred to as geometric, can be characterized as a knowledge-driven method, which involves the manual digitization of geological sections or surface maps, which are linked to representing wireframes of 3-D geological surfaces and bodies (Vollgger et al. 2015, Stoch et al., 2018). In explicit modeling geoscientists shape surfaces according to their interpretation which leads to the creation of unique and non-reproducible models, due to the subjective nature of interpretations.

Explicit Modelling Workflow



Implicit Modelling Workflow

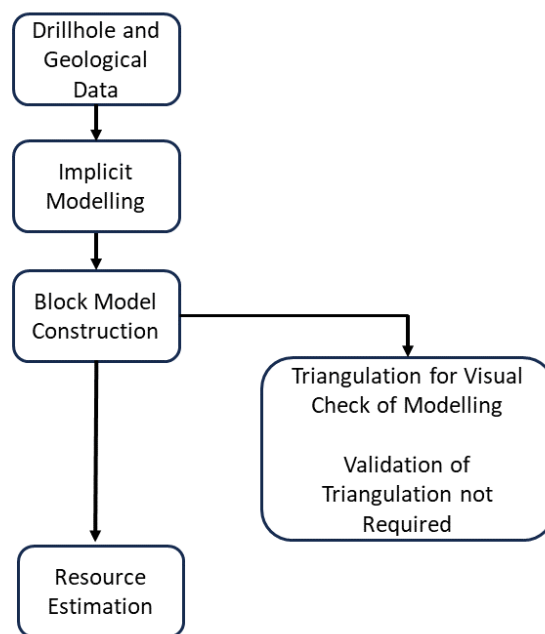


Fig. 4.13. Workflows for 3,D explicit and implicit modelling methods, presenting the differences between the two methods (Cowan et al., 2011).

3,D implicit modeling approach relies on data-driven approach and was formulated to generate geological models directly from mining and exploration drill core database, eliminating the necessity for extensive digitization (Cowan et al., 2002, 2003, 2011). Radial basis function (RBF) stands out as the predominant method for surface generation and in its initial stages, RBF interpolation was applied to compute elevation contour lines using irregular topographical data (Hardy, 1971). The advantages include a lack of time-consuming and reproducible tasks and a direct connection between data and the 3D model, making updates and changes straightforward. Disadvantages include when surfaces calculated will consistently aim for a smooth fit, given the nature of RBF-based spatial interpolation or that the model's outcome will be influenced by the type of RBF (Jessell et al., 2014).

4.4.2. 3-D Modeling Workflow

The straightforward explicit 3-D modeling workflow as shown in Fig. 4.13 and 4.14 is implemented to develop the 3D geological model.

The initial phase includes gathering, validating and preparing the available (e.g. geological, geochemical structural, drill core and topographical) data. The dataset undergoes further modification, and exportation into various file formats which are compatible with Vulcan version 2021.3 by Maptek modeling software. Then, these are imported into the software in the form of points and polylines, following their validation for erroneous values (e.g. correction or elimination of data) and classification.

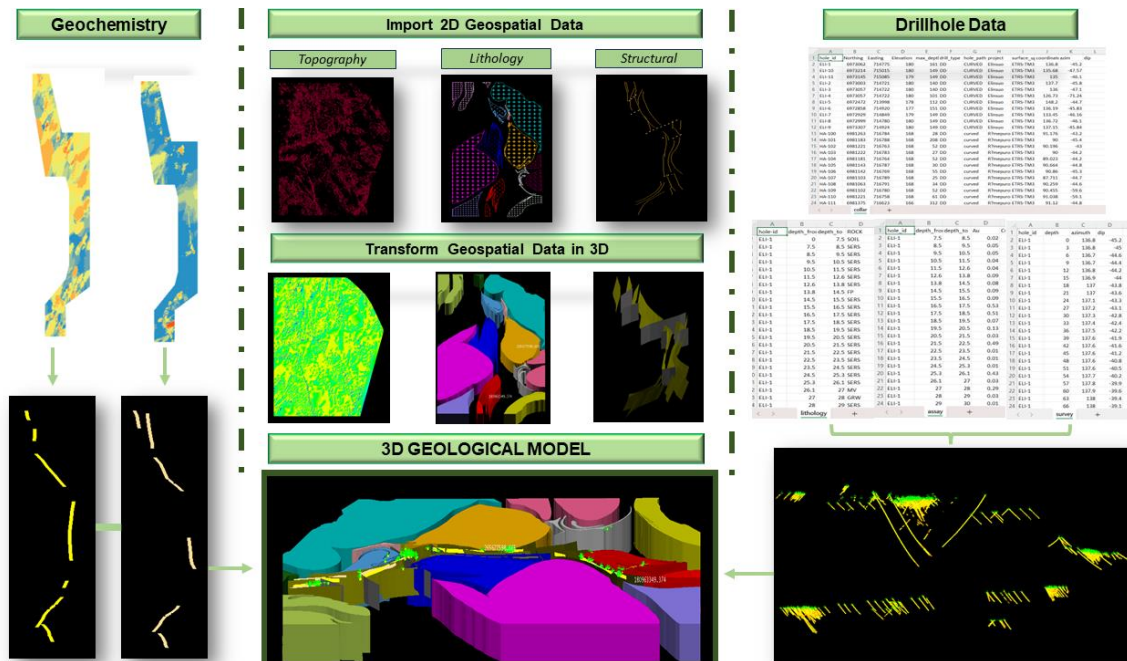
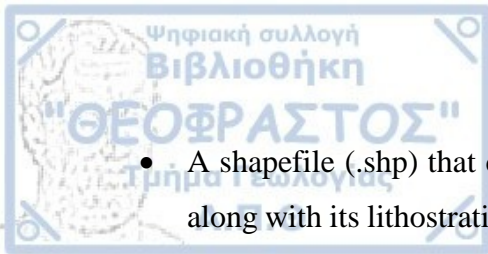


Fig. 4.14. The workflow that shows the methodology gradually incorporating topographical geological, geochemical, geophysical structural and drillhole data employed for generation of the final -3D geological model for Hattu schist belt.

4.4.3 Data import and file formats

In order to build the 3-D model the following data were imported into the Vulcan software in the order presented.

- A shapefile (.shp) that includes a 50-m interval elevation of digitized contours, along with the merge raster file (.TIFF) showcasing the topography of HSB. The data were conducted by the Geological Survey of Finland (GTK) for a broader part of Finland and was clipped to cover only the extent of HSB.



- A shapefile (.shp) that comprises the geological map sheet 1:200.000 of the HSB along with its lithostratigraphic units, which has been initially constructed from the Geological Survey of Finland (GTK) and further classified for the purpose of this thesis that showcases the lithology of each desired rock unit.
- A shapefile (.shp) containing digitized dashed and normal black lines representing the significant N-S, NE-SW shear zones and minor E-W minor normal faults of HSB, that was produced as part of this study.
- A shapefile (.shp) which incorporates the gold geochemical anomalies with the greatest importance in soil and lithology.
- Four distinct but interconnected with equal importance excel (.csv) type files containing the drill-core data.



CHAPTER 5. RESULTS

The first section of this chapter shows the results from the statistical analysis of the gold geochemical datasets. These datasets were initially carefully examined for inaccuracies, duplicates etc., and further subjected to data reduction to eliminate any outliers or erroneous data points. Various statistical analyses were applied in order to describe the gold distribution and to determine the threshold value of the geochemical anomaly. The second section focuses on illustrating the results of the two interpolation methods in order to produce continuous gold-concentration maps of the study area. Two interpolation methods were applied, one deterministic (Inverse Distance Weighting) and one geostatistical (Ordinary Kriging) along with their validation. The third part shows the detailed 3-D dimensional lithological and structural model of the HSB produced by the interpretation and digitization of the surface and drill core data.

5.1. DATA ANALYSIS

5.1.1. Data Reduction

In accordance with the recommendation by Reimann and Filzmoser (2000), a detailed examination of the distribution of each dataset was carried out along with the identification of censored values and outliers (Fig. 5.1). The censored values (points with gold concentrations below detection limit) were excluded from the geochemical datasets resulting in a database of 224 samples for soil and 504 samples for lithology.

5.1.2. Outliers

The detection of outliers involved performing descriptive statistical analysis and utilizing graphical analysis through a boxplot (Fig. 5.1). According to the boxplot, an abundance of far and mild outliers was revealed, with positive extreme values existing for both soil and lithological samples, while no negative extreme values observed (Table 5.1).

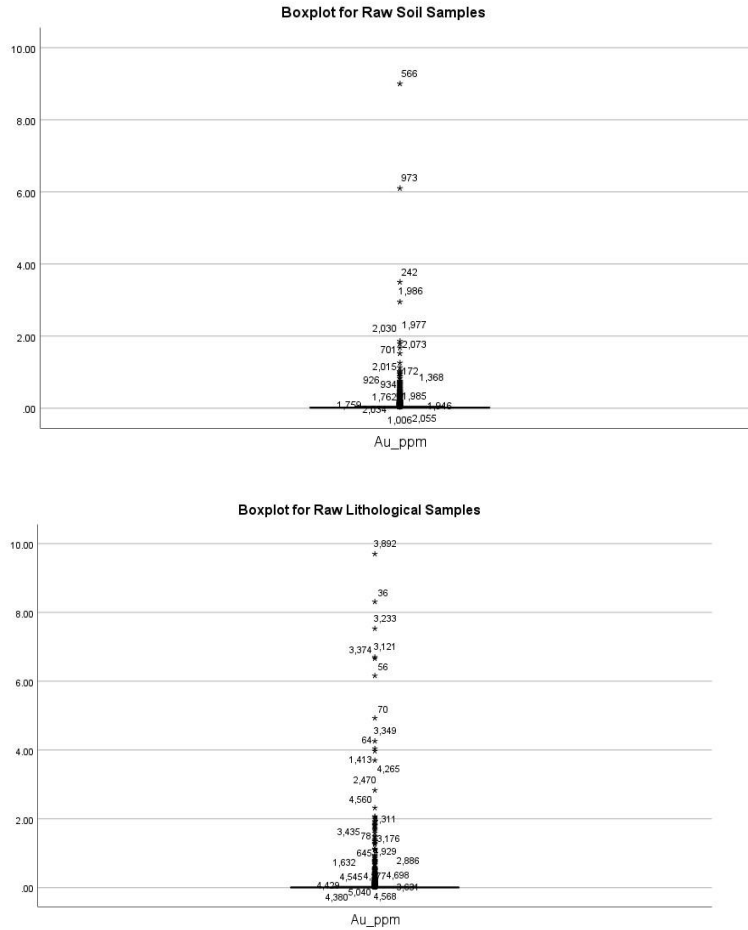


Fig. 5.1. Boxplots for the soil and lithological samples. The boxplot is barely visible due to the dataset's high positive distribution.

The addressing outliers were used firstly, in determining the threshold value, and secondly, for calculating the experimental variogram in the geostatistical analysis. The outliers that have a negative impact on the experimental variogram are also the ones that will be eliminated from the threshold analysis.

Based on repetitive analysis and testing several datasets containing each time different outliers, it has been determined that the data points associated with sample IDs 566, 973, and 242 from the soil samples should be excluded (Table 5.1). By removing these data points, a more accurate representation of the spatial autocorrelation and structure was obtained.

Table 5.1.

Detection of positive extreme values/far outliers in the initial raw data of Au (ppm) for soil and lithological samples analyzed using SPSS software version 27.0.

SOIL		LITHOLOGY	
Sample ID	Content of gold (ppm)	Sample ID	Content of gold (ppm)
566	9.00	3892	9.70
973	6.10	36	8.31
242	3.5	3233	7.53
1986	2.95	3121	6.70
701	1.86	3374	6.66

The remaining outliers do not exert a significant influence on their respective variograms, as a result, these outliers were retained in the analysis. By addressing these outliers appropriately, the reliability and accuracy of the variogram analysis is enhanced.

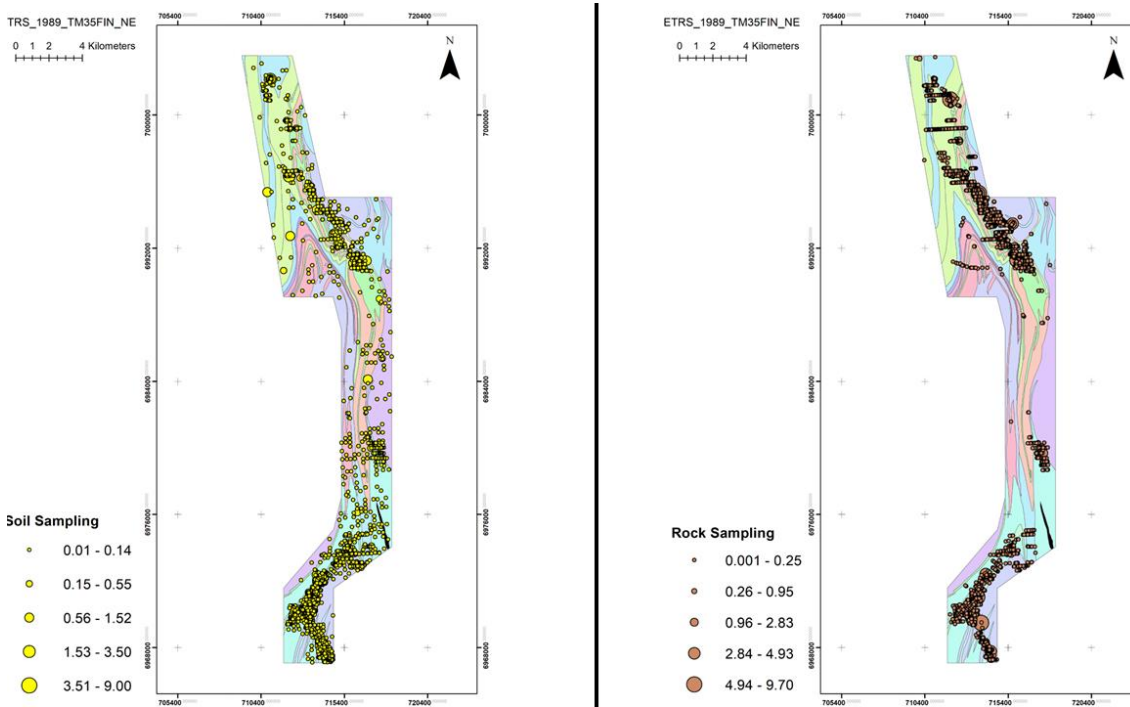


Fig. 5.2. Soil and lithology remaining samples following the data reduction and statistical – geostatistical analyses.



5.1.3 Descriptive Statistics

Descriptive statistics provided a shortcut to visualize the distribution of gold geochemical data (Table 5.2).

Table 5.2.

Descriptive Statistics of gold dataset Au (ppm) for soil and lithological samples, excluding censored/extreme values.

Au (ppm)	Soil (till)	Lithology
Samples (N)	223	504
Mean	0.046	0.045
Standard Error Mean	0.002	0.004
Standard Deviation (SDEV)	0.13	0.32
Median	0.014	0.008
Mode	0.01	0.01
Range	2.94	9.69
Min.	0.01	0.001
Max	2.95	9.69
Q1	0.01	0.002
Q2	0.014	0.014
Q3	0.03	0.016
Q3-Q1 (Interquartile Range)	0.02	0.01
Skewness	9.73	18.4
Kurtosis	136.86	412.19
Variance	0.019	0.10
Median Absolute Deviation (MAD)	0.04	0.006

As with most gold deposits, despite the removal of censored and extreme values, visually examination of the gold concentrations (in both datasets) indicates that the gold distributions are not symmetrical and do not conform to a normal distribution model (Gaussian).

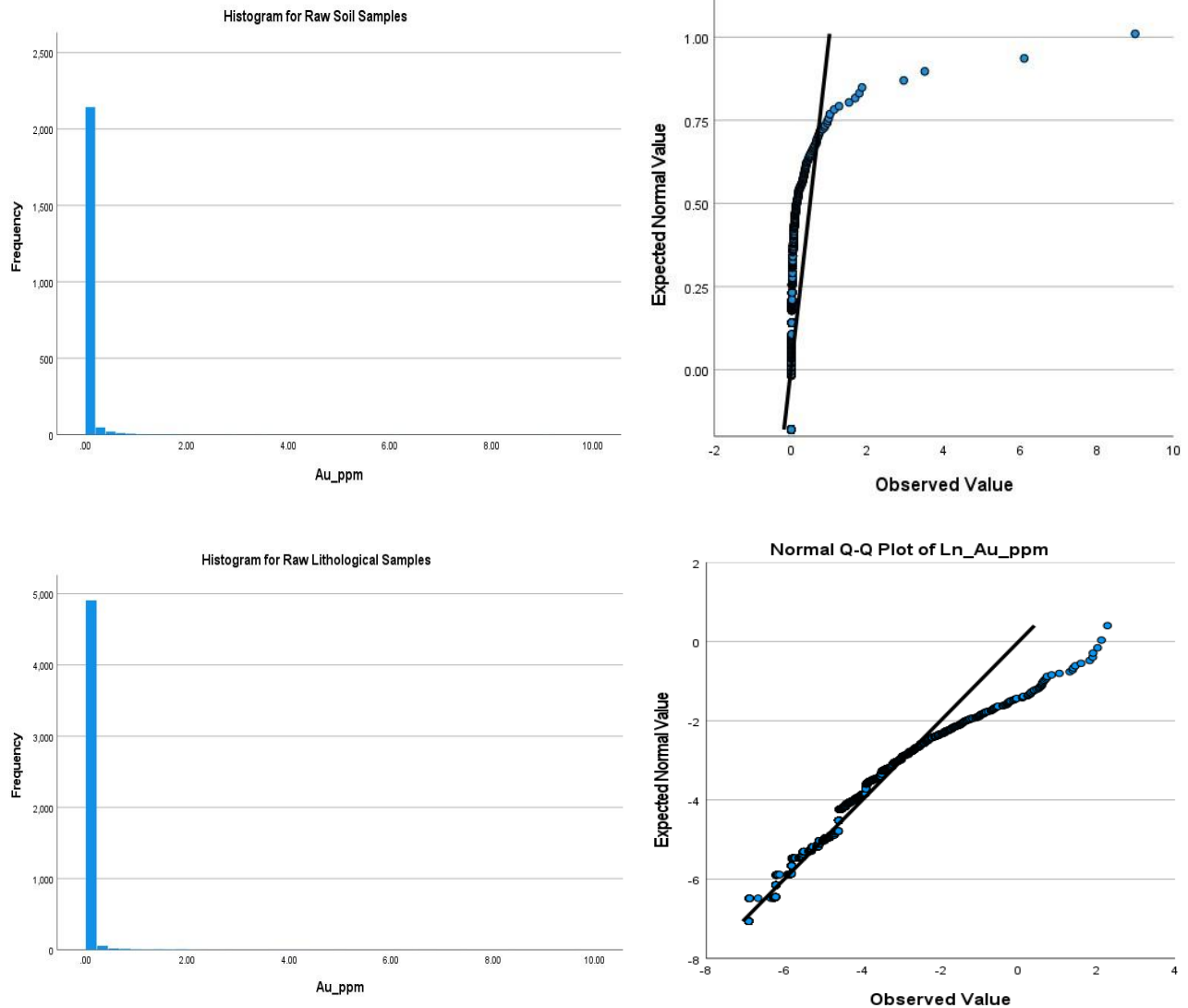
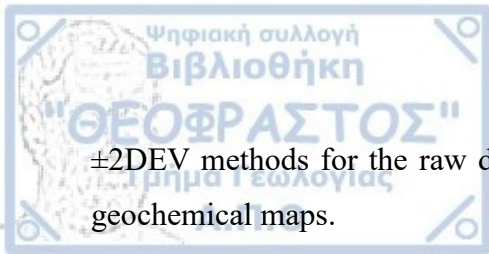


Fig. 5.3. Histograms and Q-Q plots of the raw datasets

Skewness and kurtosis coefficients are also used to examine quantitatively the distribution type of the geochemical data. Based on the high skewness and kurtosis values, it is clear that the distribution is skewed to the right or positively skewed. The mean values are larger than the median values and the standard deviation values are greater than the MAD's. Due to the right skewed nature of the gold data sets, the mean - 2DEV and median - 2MAD methods results in only negative values. Hence, using the median $\pm 2MAD$ or mean



$\pm 2\text{DEV}$ methods for the raw datasets in identifying a threshold could lead to erroneous geochemical maps.

5.1.4. Data Transformation

In order to deal with the positive skewness and to reduce the distributional asymmetry in the gold dataset a natural logarithm transformation was applied.

Table 5.3.

Descriptive statistics of natural logarithm transformed gold dataset for soil and lithological samples.

Au (ppm)	Soil (till)	Lithological
Samples (N)	223	504
Mean	-3.88	-4.91
Standard Error Mean	0.02	0.02
Standard Deviation (SDEV)	0.96	1.42
Median	-4.26	-4.82
Mode	-4.61	-4.61
Range	5.69	9.18
Min.	-4.61	-6.91
Max	1.08	2.27
Q1	-4.61	-6.19
Q2	-4.26	-4.82
Q3	-3.50	-4.10
Q3-Q1 (Interquartile Range)	1.10	2.09
Skewness	1.77	0.89
Kurtosis	3.28	1.57
Variance	0.93	2.1
Median Absolute Deviation (MAD)	0.34	0.98

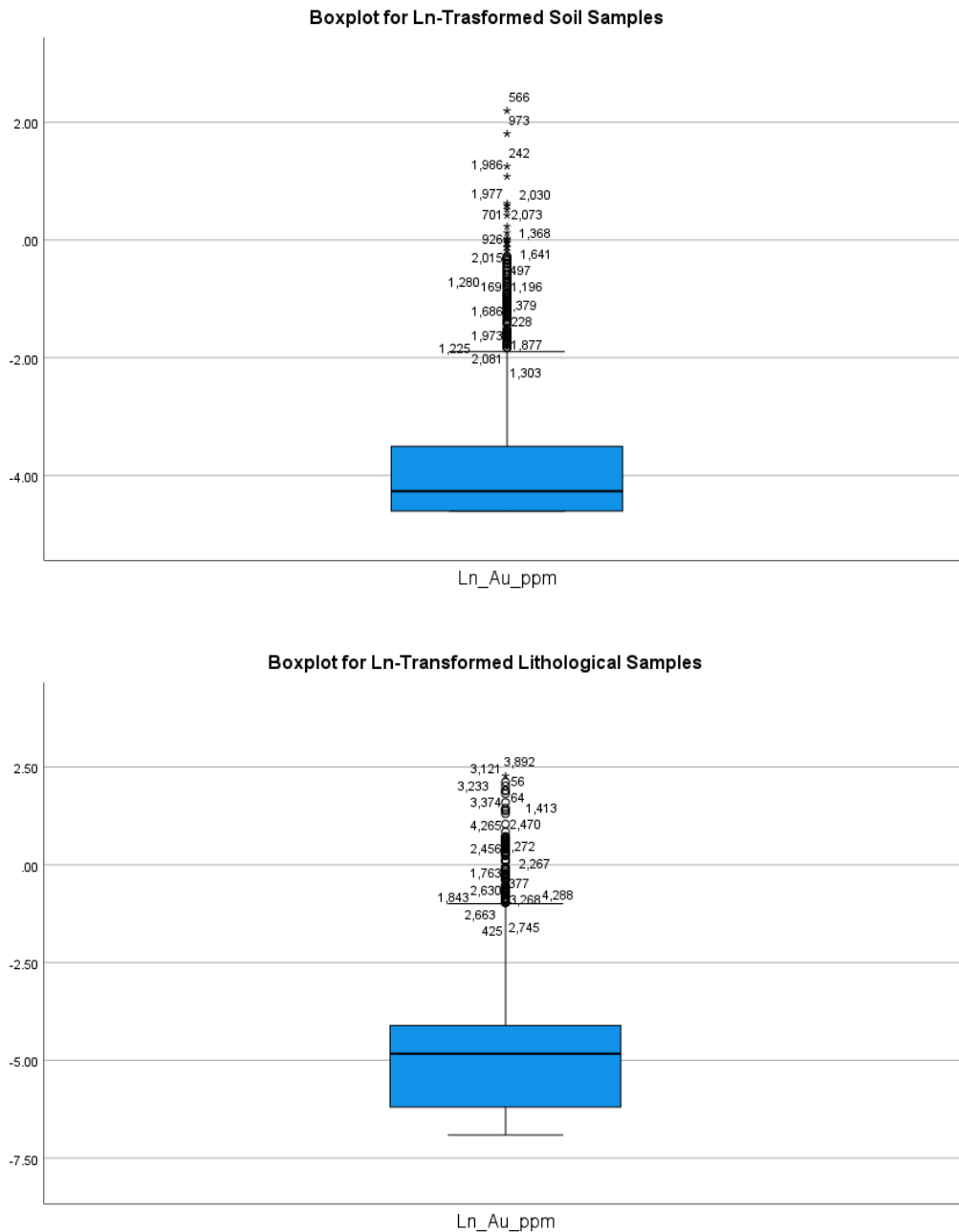


Fig. 5.4. Boxplots of natural logarithm transformed (soil and rock) datasets

The distributions of the transformed datasets exhibit improved symmetry compared to the raw data, however (Fig. 5.4 and 5.5), neither dataset adheres to a normal distribution. Improved symmetry is more evident in rock samples, and specifically in smaller skewness and kurtosis values (Table 5.3). The boxplots of the transformed data conform to the standard format of a boxplot with fewer outliers (Fig. 5.3). Such outcomes indicate that the

natural logarithm transformation has reduced the impact of the extremely low or high values, causing improved symmetry in the empirical density distributions of each dataset.

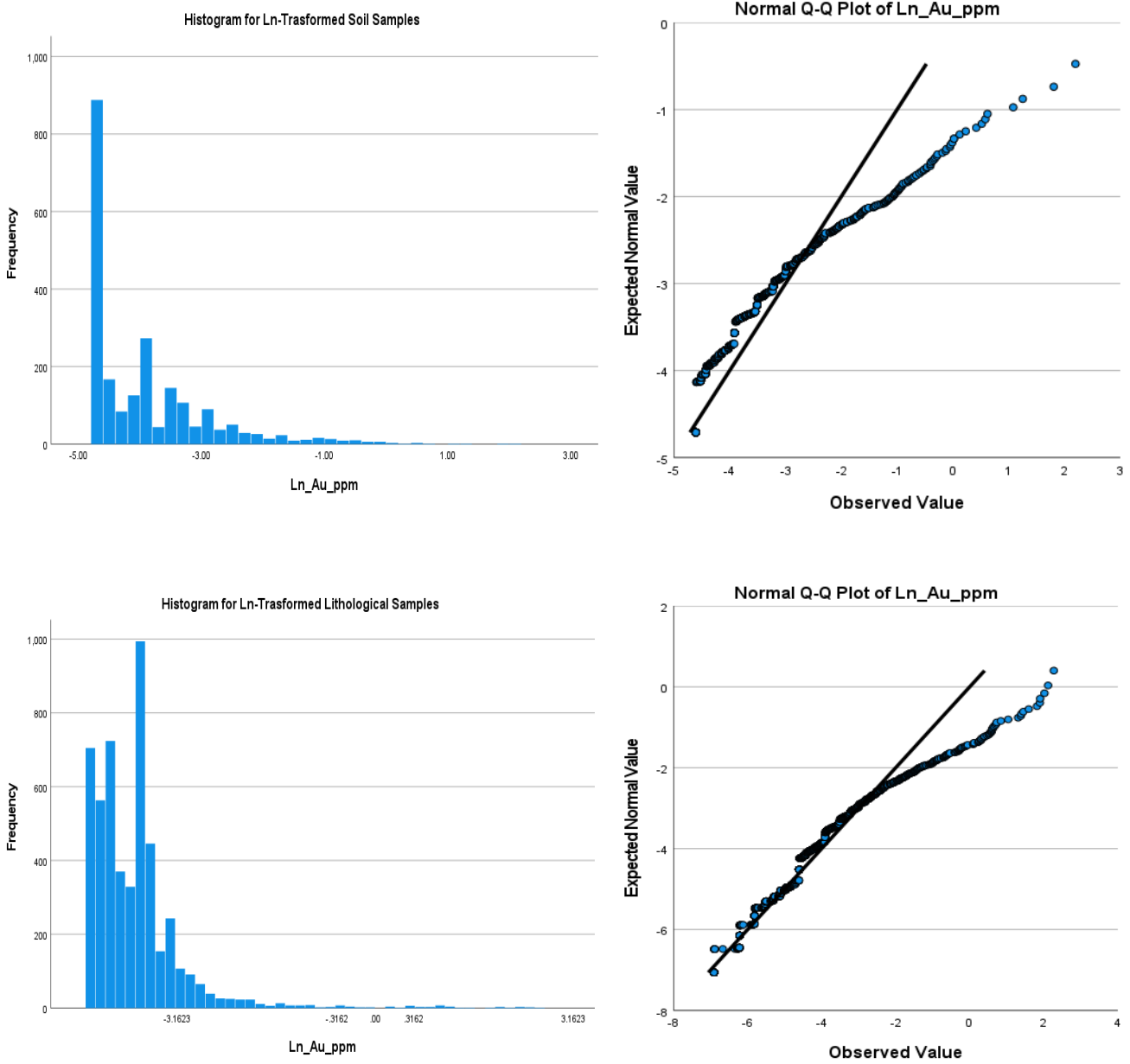


Fig. 5.5. Histograms and Q-Q plots of natural logarithm transformed datasets.



5.2. THRESHOLD EVALUATION

In order to compute the threshold values, both the mean $\pm 2SDEV$ and the median $\pm 2MAD$ techniques were tested. Since the datasets have been logarithmically transformed, when calculating the thresholds, negative threshold values were also obtained. The equations were initially calculated as if the data were normally distributed. To ensure that the final value is meaningful for the original non-transformed datasets, it was necessary to perform an inverse natural logarithm transformation and use those thresholds for the original datasets.

A third threshold technique (UW) was additionally applied, which was determined by the Upper Whisker (UW) method (Equation) of the boxplots. The results of these methods are presented and compared in Table 5.4.

Table 5.4.

Threshold values defined with three different threshold techniques of Exploratory Data Analysis (EDA), mean $+2SDEV$, median $+2MAD$ and boxplot UW of natural logarithm univariate data sets.

Au (ppm)	Median +2 MAD		Boxplot UP		Mean +2DEV	
	Soil	Lithology	Soil	Lithology	Soil	Lithology
Threshold	0.027	0.057	0.15	0.38	0.14	0.12

By analyzing the thresholds for each of the three methods (Table 5.4), it is obvious that the threshold values determined by the median $+2MAD$ are consistently the lowest for both lithology and soil followed by either the mean $+2DEV$ and the UW. This indicates that the median $+2MAD$ threshold values result in the highest number of geochemical anomalies. The observations of the study regarding the ranking of threshold values align with the findings reported by Reimann et al. (2005) and Carranza (2009).

5.3. VARIOGRAPHY

For the Ordinary kriging method, two variograms for each dataset were calculated, considering the direct and indirect factors that influence the variogram. The steps are shown as demonstrated in the methodology.

5.3.1. Trend analysis

With the Trend Analysis tool, it is evident that the projected points are represented by flat lines and do not exhibit any discernible trend in different directions (Fig. 5.6). From the trend analysis graph, it is clear that the green and blue lines are straight for soil and lithology. Hence, it is not mandatory to employ polynomials for removing trend. The absence of trend suggests that the assumption of stationarity is valid for the experimental variogram, allowing to proceed with further variogram analysis.

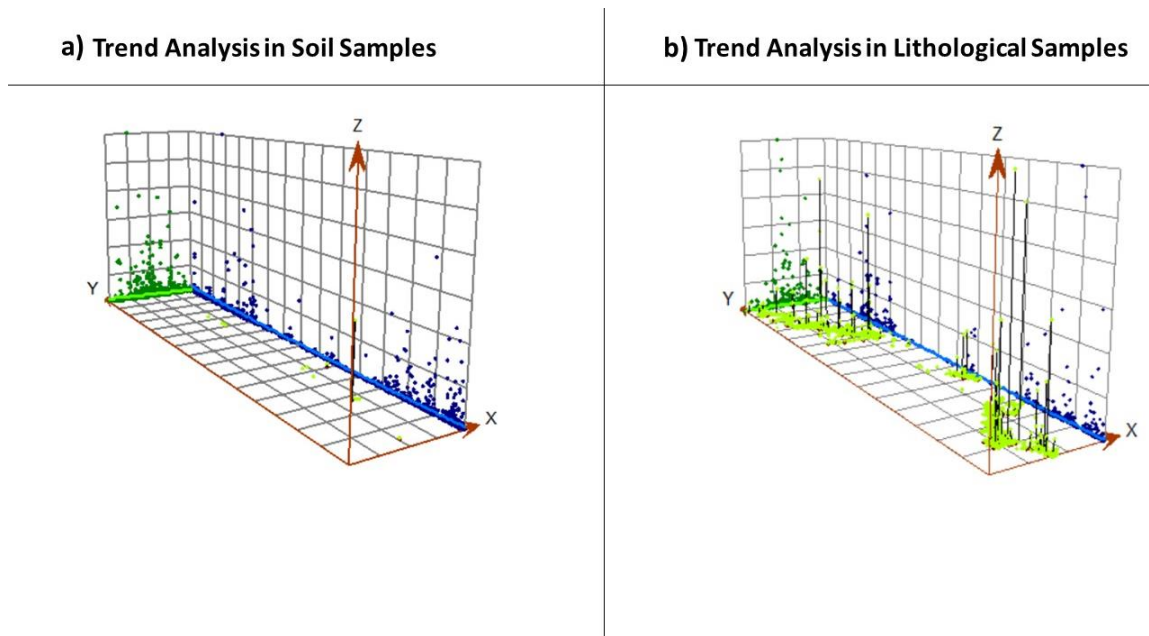


Fig. 5.6. Trend analysis as displayed in ArcGIS for soil and lithology, revealing that the projected points which are represented as lines remaining flat without any obvious trend in the N-S or E-W direction.

5.3.2. Variogram parameters and models

Table 5.5 shows the calculated variogram parameters and the Figure 5.7 their graphical representation. The variables exhibit a small nugget effect, measuring less than 1, namely 0.012 for soil and 0.04 for lithology. These numbers indicate a very small disruption or random variation in the pattern of data and have been considered in the analysis. Sills have also been evaluated as 0.028 and 0.061, so, in distances greater than the sill, there is no spatial correlation between the points. The range was defined as 33.868 and 2217 in meters, so sample locations within this value exhibit spatial autocorrelation,



while locations beyond the range do not display significant spatial correlation or none at all. With the availability of sill and nugget, it is feasible to assess spatial dependence or autocorrelation using the nugget to sill ratio. According to Cambardella et al. (1994), with a computed nugget to sill ratio of 0.42 and 0.65 for soil and lithology the assessment of spatial dependence in this area can be described as medium. The experimental variogram does not demonstrate an unbounded increase nor does it become progressively steeper while increasing lag distance.

With all the parameters calculated and after visual inspection of the experimental variogram for variations in directionality it was detected that the spatial variation exhibits diverse patterns in different directions, indicating the presence of anisotropy in different directions. The search process included testing and aligning the directional pointer with different axes (e.g. major or minor) of the anisotropic ellipse, but had no footprint at the final output. With several possibilities tested, by setting the maximum and minimum neighbors to 5 and 2 respectively, along with a four-sector configuration employing a 45-degree offset in lithology and one sector in soil, resulted in minimal prediction errors.

It was concluded that the theoretical Gaussian and Exponential models are appropriate for fitting (Fig. 5.7) and the most optimal number of lags for both soil and lithology cases was determined to be 11.

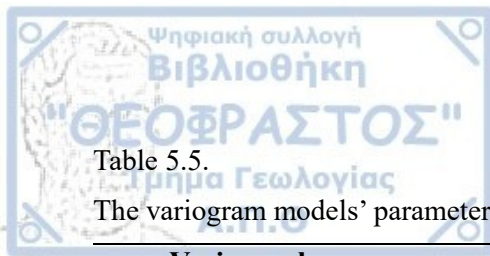
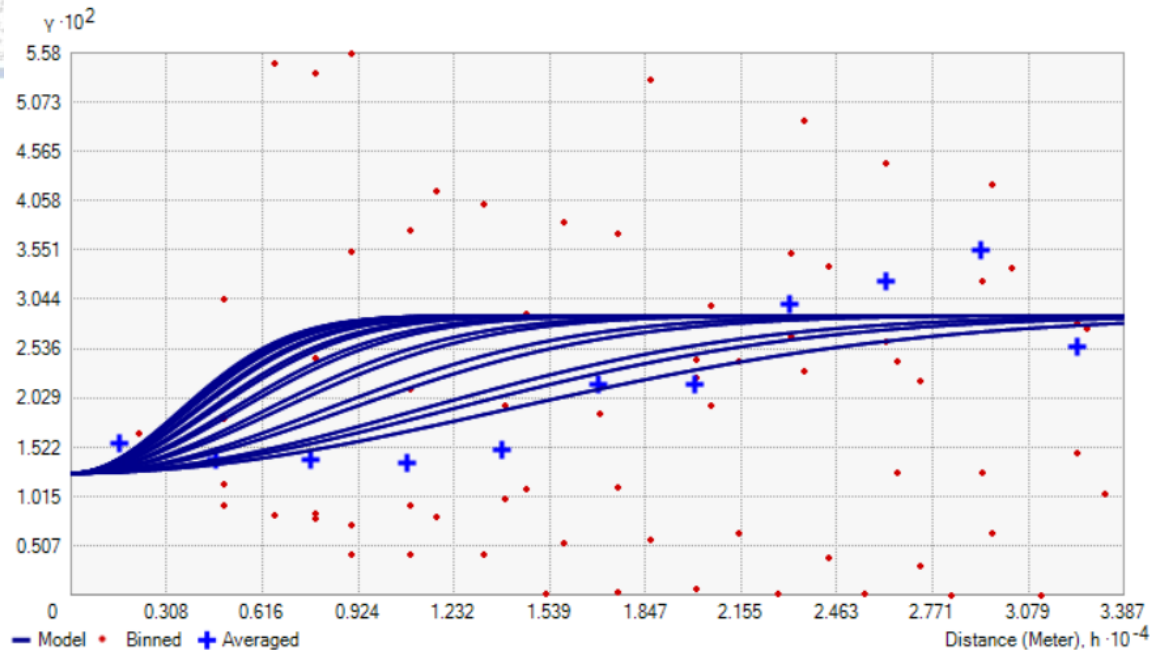


Table 5.5.
The variogram models' parameters for soil and lithology

Variography	Soil Parameters	Lithology Parameters
Kriging Method	Ordinary Kriging	Ordinary Kriging
Model Type	Gaussian	Exponential
Neighborhood Type	Standard	Standard
Maximum Neighbors	5	5
Minimum Neighbors	2	2
Sector Type	One Sector	Four Sectors with 45° Offset
Number of Lags	11	11
Lag Size	3078.96	201.59
Anisotropy	Yes	Yes
Nugget	0.012	0.04
Partial Sill	0.016	0.021
Sill	0.028	0.061
Range	33868	2217

Semivariogram



Semivariogram

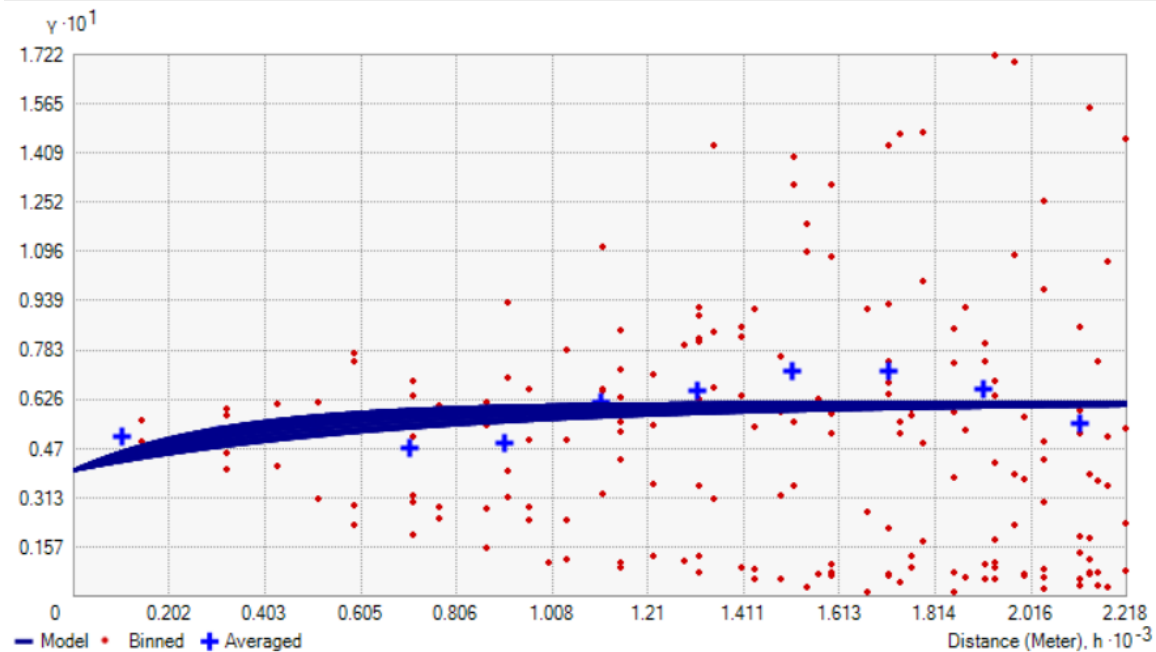


Fig. 5.7. Anisotropic variogram graphs computed in ArcMap 10.8.1 for soil (a) and lithology (b) dataset. The binned values are represented as red dots, obtained by grouping empirical semivariogram points using square cells that have a width of one lag and capture the local variation in semivariogram values. The average points, depicted as blue crosses, are generated by grouping semivariogram points falling within angular sectors and display a smoother variation in semivariogram values.

5.3.3. Ordinary Kriging's Cross-Validation

The diagnostic statistics of ME, MSE, RMSE, ASE are close to zero in both instances (Table 5.6). The RMSSE statistic, in soil samples is 1.22, and in bedrock samples is 1.01. Based on the diagnostics both are acceptable, but the lithology diagnostic is more optimal. These results, especially in lithology indicate that the models describe the variation without exhibiting biased predictions. Although the RMSE is also near zero, it doesn't match the ME closely, signifying that the predicted are often not correspond to the measured values. Alternatively, the lower value of the ASE diagnostic compared to the RMSE also implies an underestimation in soil sample predictions. Despite the RMSSE statistic being close to 1, its value exceeding 1 in both cases suggests another contributing factor to the overall underestimation of predictions.

OK yielded trustworthy outcomes for both cases. As a result, their models are kept in the analysis and the comparison will be between these, and the final models, extracted by the IDW method.

Table 5.6.

Cross validation summary diagnostics for Ordinary Kriging (OK).

Diagnostics	Soil Validation Statistics	Lithology Validation Statistics
Mean Error (ME)	0.0014	0.000098
Root Mean Square Error (RMSE)	0.14	0.21
Mean Standardized Error (MSE)	0.012	0.0049
Root Mean Square Standardized Error (RMSSE)	1.22	1.01
Average Standard Error (ASE)	0.11	0.2

5.3.4. Ordinary's Kriging Geochemical Maps

The prediction surfaces of the gold geochemical anomaly are displayed as spatial distribution maps (Fig. 6.4.). This outcome is the result of using the Geostatistical Analyst

tool, which interpolates the variable values based on the boundaries of the sampled data points.

The geochemical maps display the gold concentrations using the original scale, where filled contours connect regions with identical values and are colored accordingly. The blue color represents the lowest or no concentration, while the red color represents the maximum concentrations, and it was selected in such way where the blue progressively intensifies until it reaches the maximum content of gold. The threshold values, previously derived with EDA, highlight the most significant geochemical anomalies within the HSB.

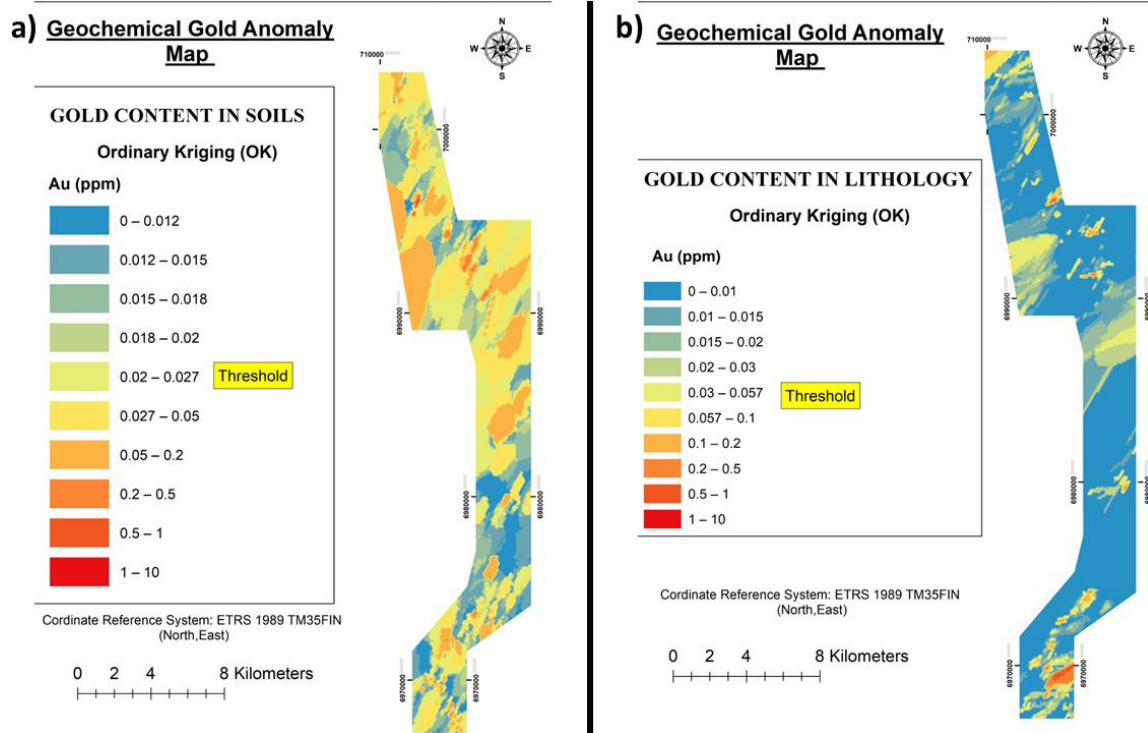


Fig. 5.8. The soil (a) and lithology (b) gold geochemical anomaly maps of Hattu Schist Belt generated with Ordinary Kriging (OK) interpolation, each map with its corresponding threshold value.



5.4. IDW INTERPOLATION

5.4.1. Characteristics of IDW

In the case of IDW the only factor to evaluate was the directional influence. The directional influence has already been addressed through OK, accordingly, and the same directional influence was applied for IDW analysis.

The power parameter plays a significant role in IDW analysis, and different models were tested, each with a different power parameter. The outcomes revealed that as the power parameter decreased, the analysis showed a greater reduction in RMSE compared to the models with higher p values (Table 5.7). Therefore, the model that uses $p=1$, appeared to be more accurate and was chosen for the creation of the geochemical anomaly maps. The two IDW models demonstrated optimal performance with a configuration in which the maximum neighbors were set to 5 and the minimum to 2. In order to minimize the prediction error, the soil model required a one-sector type, while the lithological model benefited from a 4-sector type with a 45-degree offset. Table 5.7. presents an overview of the unique parameters associated with the IDW interpolation.

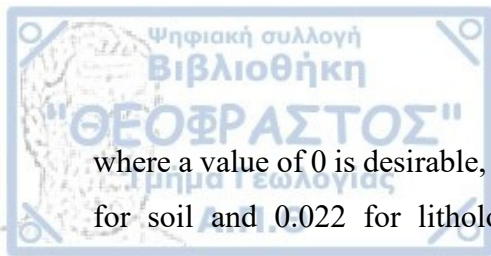
Table 6.7.

Parameters for IDW interpolation for soil and lithological samples.

IDW Analysis	Soil Parameters	Lithological Parameters
Method	Inverse Distance Weighting	Inverse Distance Weighting
Neighborhood Type	Standard	Standard
Power Parameter	1	1
Maximum Neighbors	5	5
Minimum Neighbors	2	2
Sector Type	One Sector	Four Sectors with 45° Offset
Angle	30°	30°

5.4.2. Inverse Distance Weighting's Cross-Validation

The diagnostics provided by ArcGIS are limited to two, yet these two diagnostics are consistent across both methods. The ME values for both analyses are closely centered around zero, specifically 0.03 for soil and 0.001 for lithology, underscoring once again the model's ability to generate adequate predictions. With regard to the RMSE diagnostic,



where a value of 0 is desirable, it is evident that both are in close proximity to zero, at 0.15 for soil and 0.022 for lithology. Consequently, the IDW analysis exhibited reliable outcomes (Table 5.8).

Table 5.8.

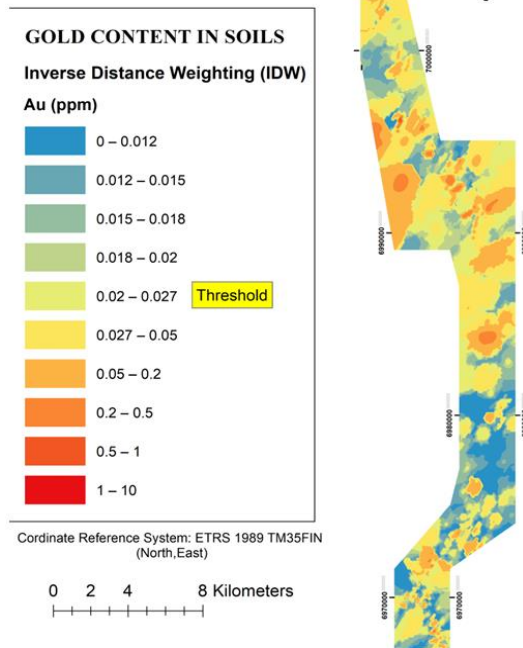
Cross validation summary diagnostics for Inverse Distance Weighting (IDW).

Diagnostics	Soil Validation Statistics	Lithology Validation Statistics
Mean Error (ME)	0.03	0.001
Root Mean Square Error (RMSE)	0.15	0.22

5.4.3. IDW's Geochemical Maps

The IDW geochemical anomaly raster maps (Fig. 5.9) are defined in ArcGIS as contours. The color scale depicting gold contents remains consistent across both methods. It transitions from blue, indicating zero or lower gold content, to red, symbolizing the higher concentrations. Gold concentrations are aligned with their initial original scale, and the threshold value for both soil and lithological samples highlights the significant geochemical anomalies.

a) Geochemical Gold Anomaly Map



b) Geochemical Gold Anomaly Map

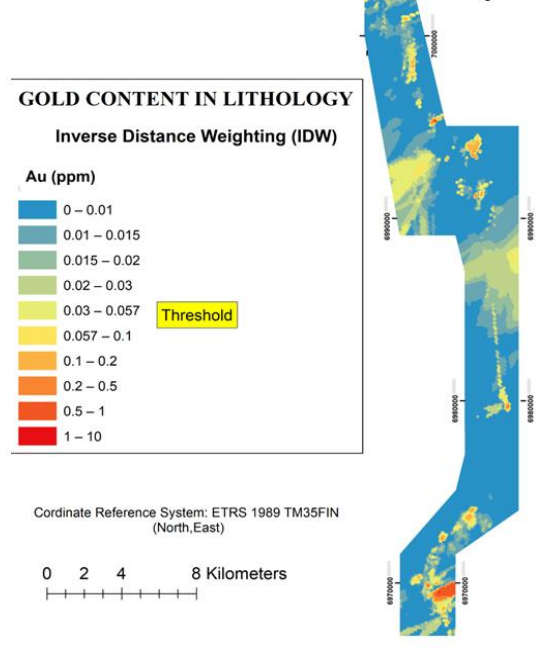


Fig. 5.9. The soil (a) and lithology (b) gold geochemical anomaly maps of Hattu Schist Belt generated with Inverse Distance Weighting (IDW) interpolation, each map with its corresponding threshold value.

5.4.4. Comparing Ordinary Kriging and Inverse Distance Weighting Methods

There are certain challenges that need to be considered when conducting geochemical mapping analysis with different interpolation methods. Kriging introduces a “smoothing effect,” potentially leading to the underestimation of high values and overestimation of low values., while IDW exhibits the “bull’s eye” effect, arising from localized high or low values (Zhang et al., 2021).

For HSB, it seems that when IDW and Ordinary Kriging methods applied the gold geochemical maps gave the same results, with a slight difference that the IDW method had more “satisfactory” optical results. In other words, the anomaly contrast resolution is higher in the distribution maps with the IDW method, especially for the soil geochemical maps. Visually, this resulted in broader generalizations and more distinct circular contour bands, compared to the less distinct bands of interpolated values around the same field sample points for the OK method.

In contrast, lithological geochemical maps do not provide evidence supporting this assumption, as there is no-worth mentioned differences when comparing the lithological geochemical maps of OK and IDW. These two maps depict the same geochemical target areas, demonstrating no substantial variations in gold content.

Since the IDW method comprises solely the RMSE and ME diagnostics, the cross-validation and comparison should be focused on these parameters (Table 5.9).

Table 5.9.

Comparison between the cross-validation diagnostics between Inverse Distance Weighting (IDW) and Ordinary Kriging (OK).

Comparison OK-IDW Method	Soil Validation Statistics		Lithology Validation Statistics	
	IDW	OK	IDW	OK
Mean Error (ME)	0.03	0.0014	0.001	0.000098
Root Mean Square Error (RMSE)	0.15	0.14	0.22	0.21

It appears that while the ME values consistently favor OK with a noticeable difference, the RMSE prediction errors are almost identical. Optimally, considering the minor differences in diagnostics, OK emerges as a slightly more favorable method over IDW for analyzing soil and lithology datasets.

In terms of validity, it appears that both methods underestimate the samples. This presumption can be verified through the diagnostic measures of ASE and RMSE in the OK method. In soil, the ASE diagnostic is lower than the RMSE indicating a significant underestimation of the samples. Such underestimation is not evident in lithology since the ASE and RMSE diagnostics are quite similar, making the lithology geochemical map of OK a more valid model.

HSB contains many well-established gold occurrences that can serve as testing points for the predicted values. IDW and OK had satisfactory outcomes in Pampalo and Kuittila zones, but neither method could confirm the prospects in Hosko and Hattuvaara zones. This additional validation method has no impact on the comparison of the two methods. Given the slightly better outcomes in optimal comparison, the geochemical maps generated by OK were kept for delineating the geochemical anomalies.



5.5. GEOCHEMICAL GOLD ANOMALY ZONES

Numerous scattered and discontinuous geochemical anomalies are identifiable throughout the extent of the belt. Some noteworthy major NE-SW trending and minor N-S semicontinuous linear geochemical anomalies are worthy of attention. The existence of these significant anomalies corresponds well with the early findings of till geochemistry, supporting that it is capable of demonstrating geochemical zones in HSB (Hartikainen and Nurmi, 1993). The most promising zones are primarily located in Kuittila and Pampalo zones and secondarily in Hosko and Hattuvaara zones.

At Kuittila zone, the majority of gold anomalies are following contact between the Kuittila tonalite and metasediments. This zone is approximately 5 km in length is the footprint of the intense hydrothermal alteration at Muurinsuo and Korvilansuo deposits (Fig. 5.10). The geochemical anomalies seem to follow the direction of the NE-SW dipping high strain zones.

At the central and northern part of the belt where the Ramepuro deposit is located, the gold anomalies are much lesser in number and intensity, only close to Rämepuro. The anomalies follow a N-S trend forming a 2 km straight line straight line which passes through the metasediments parallel to the N-S dipping high strain zones (Fig. 5.11).

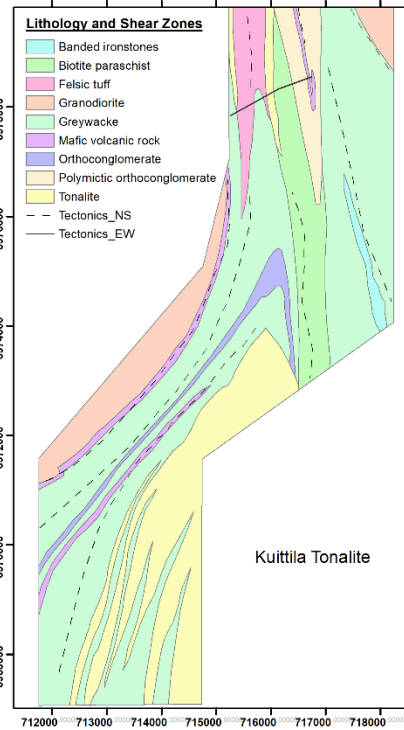
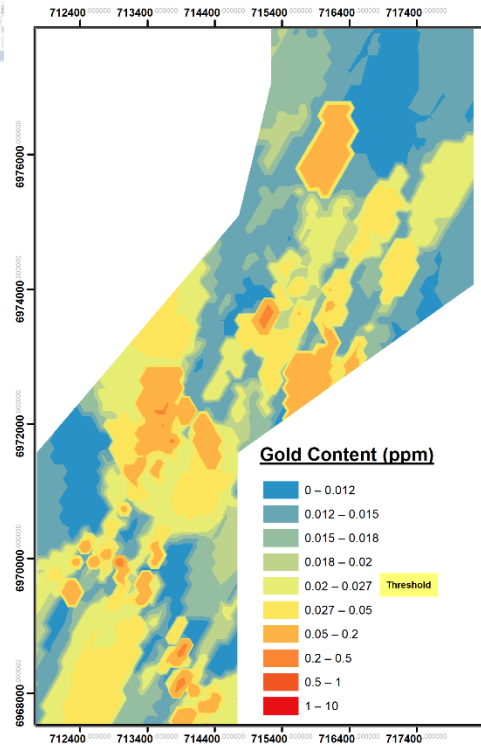
Pampalo zone produces the most notable intrigue (together with Kuittila zone), geochemical anomalies in both soil and bedrock. Gold exhibits noticeable NW-SE anomalies with the higher contents of gold in this region that creates a curved geochemical anomaly, spanning over 10 km (Fig. 5.12).

Similar to the Hattuvaara zone the Hosko zone presents only small gold anomalies over the Hosko deposit and more profound where the Kuivisto prospects are situated. The anomaly zone is less than 1 km long, trending N-S to NNW-SSE (Fig.5.13).

0 0.5 1 2 Kilometers

KUITTILA ZONE

ETRS_1989_TM35FIN_(North, East)



0 0.5 1 2 Kilometers

KUITTILA ZONE

ETRS_1989_TM35FIN_(North, East)

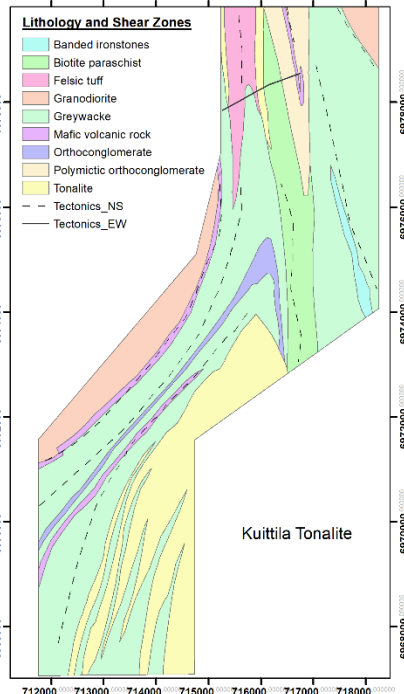
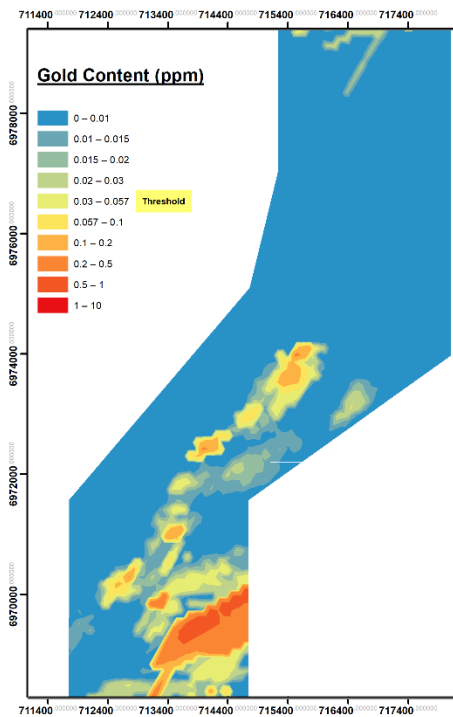


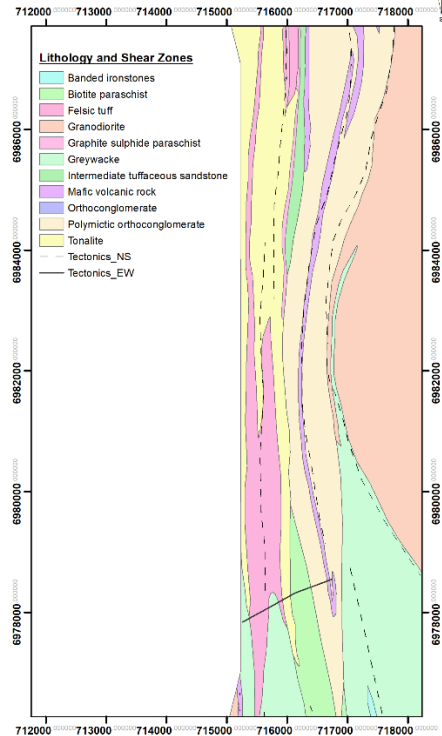
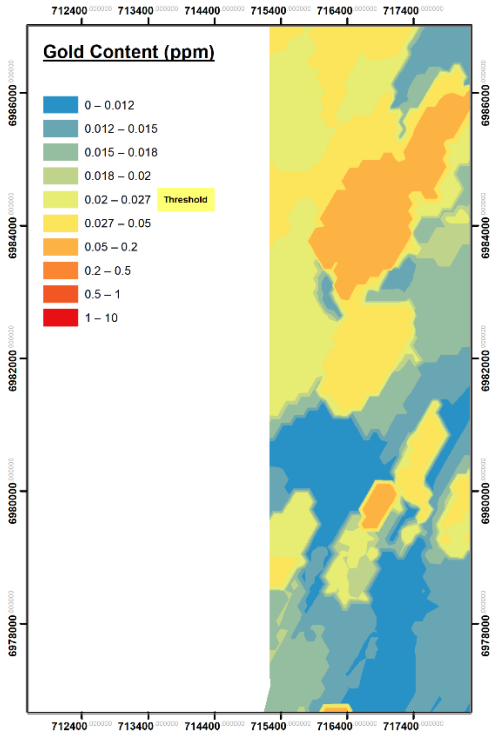
Fig. 5.10. Gold geochemical distribution maps for soil and bedrock in the Kuittila Zone.



0 0.5 1 2 Kilometer

HATTUVAARA ZONE

ETRS_1989_TM35FIN_(North, East)



0 0.5 1 2 Kilometer

HATTUVAARA ZONE

ETRS_1989_TM35FIN_(North, East)

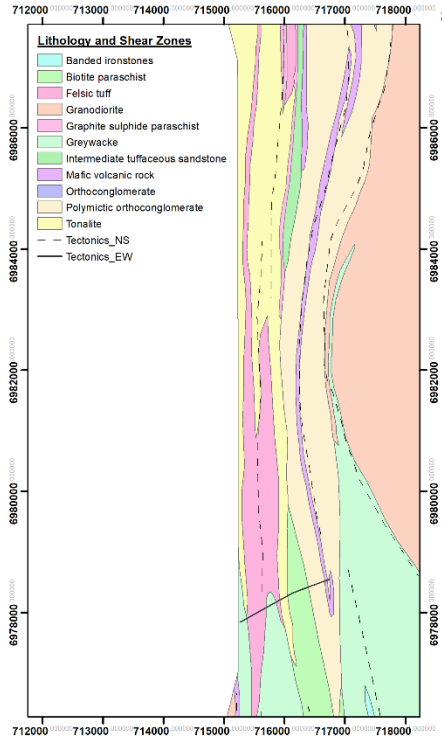
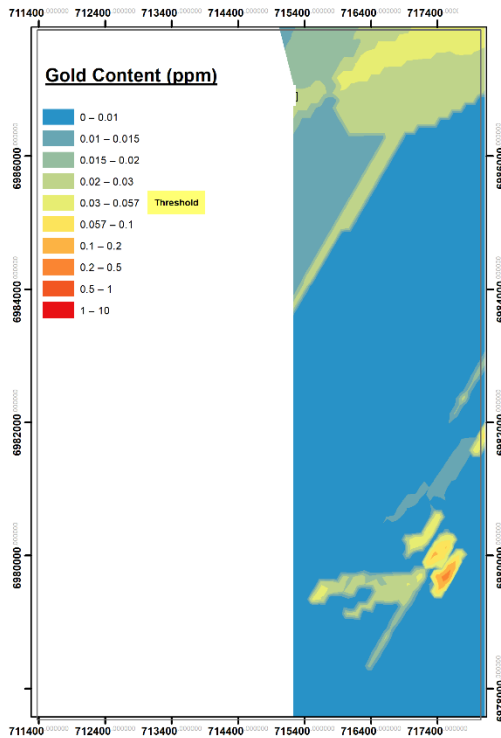
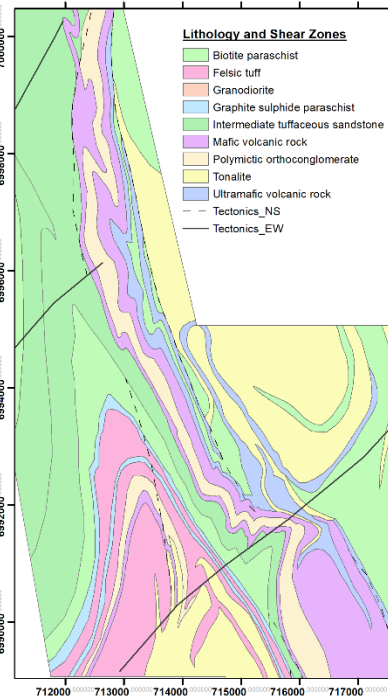
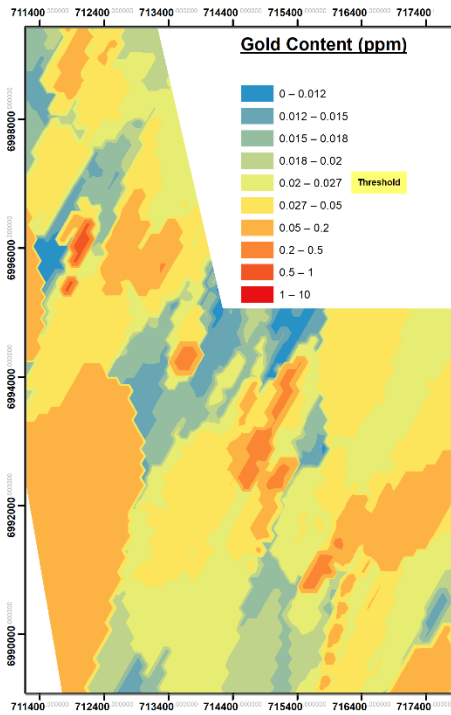


Fig. 5.11. Gold geochemical distribution maps for soil and bedrock in the Hattuvaara Zone.

0 0.5 1 2 Kilometers

PAMPALO ZONE

ETRS_1989_TM35FIN_(North, East)



0 0.5 1 2 Kilometers

PAMPALO ZONE

ETRS_1989_TM35FIN_(North, East)

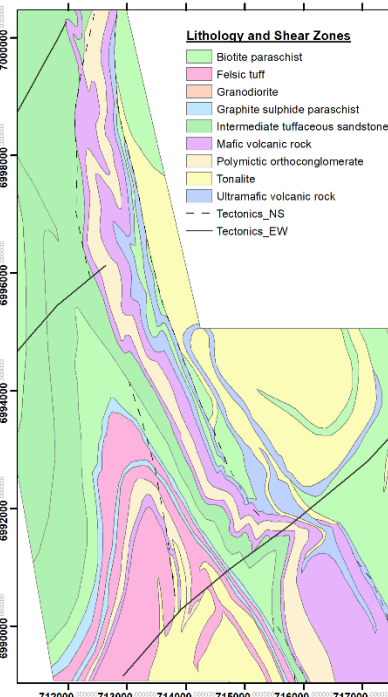
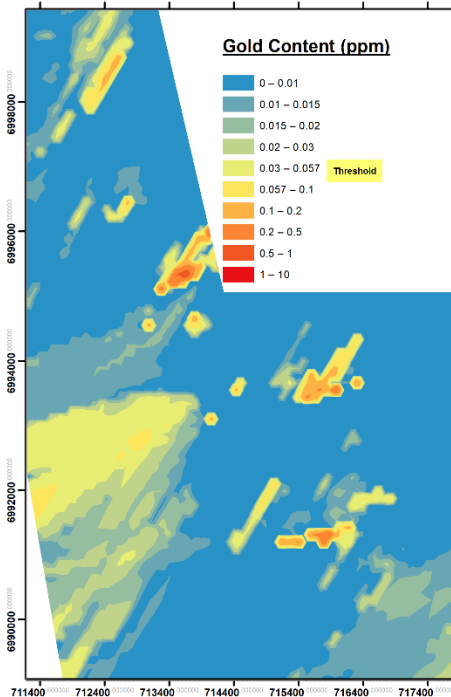


Fig. 5.12. Gold geochemical distribution maps for soil and bedrock in the Pampalo Zone.

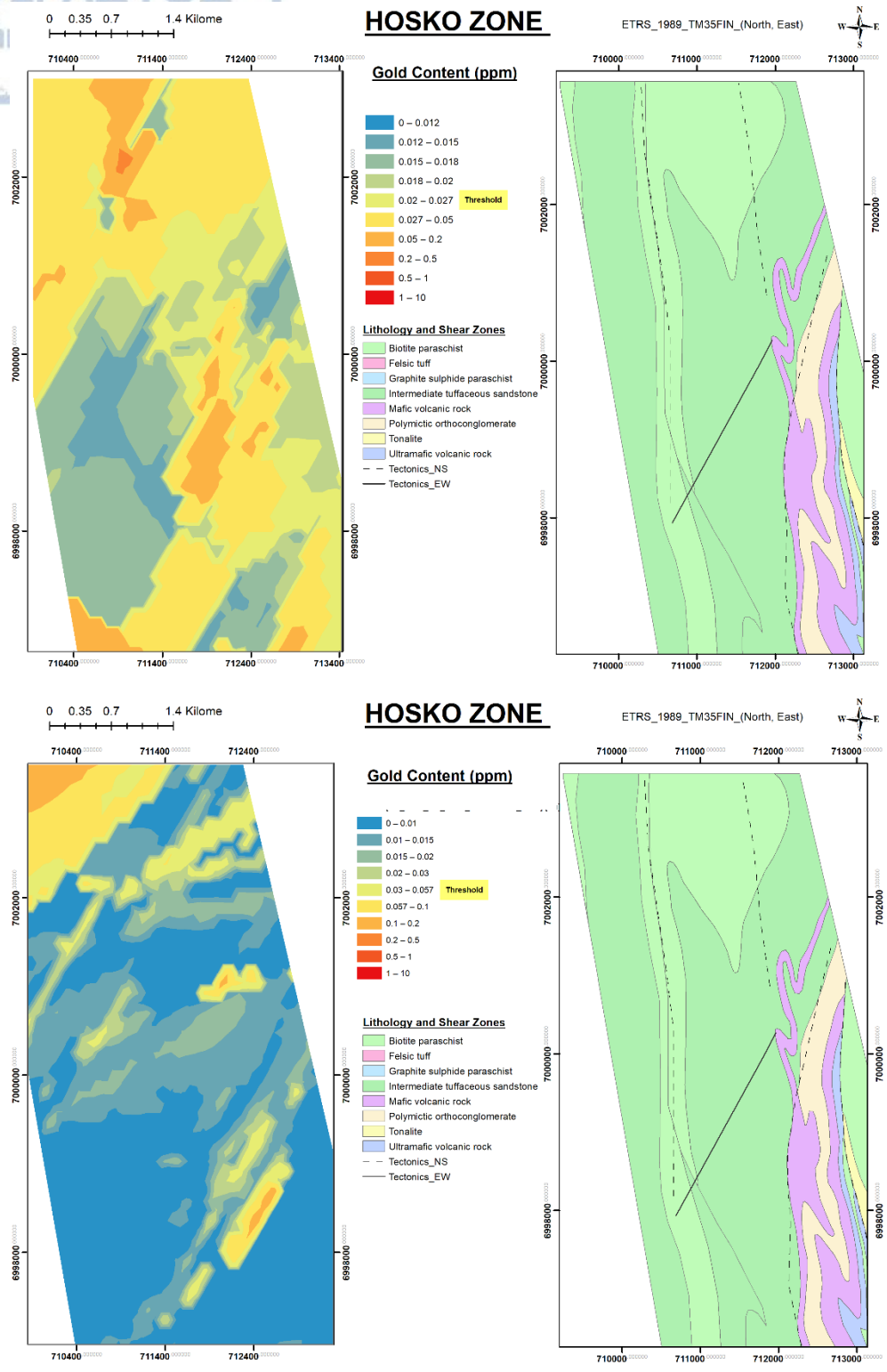


Fig. 5.13. Gold geochemical distribution maps for soil and bedrock in the Hosko Zone.

5.6. DELINEATION OF GOLD ANOMALY LINEAMENTS

Based on the geochemical anomaly maps supplementary lineaments were depicted and digitized in ArcGIS with the intention to bridge the geochemical anomalies that extend over the HSB. As seen in Figure 5.14 multiple coalescing gold anomaly zones are revealed from Hosko to the southern part of Kuittila Tonalite. These are situated within lithologies such as metasediments, mafic, ultramafic and volcanic rocks along the contacts to granitoids. The influence that the NE-SW high strain zones have in gold distribution is in no doubt, leading the gold anomalies aligning in this direction for many kilometers.

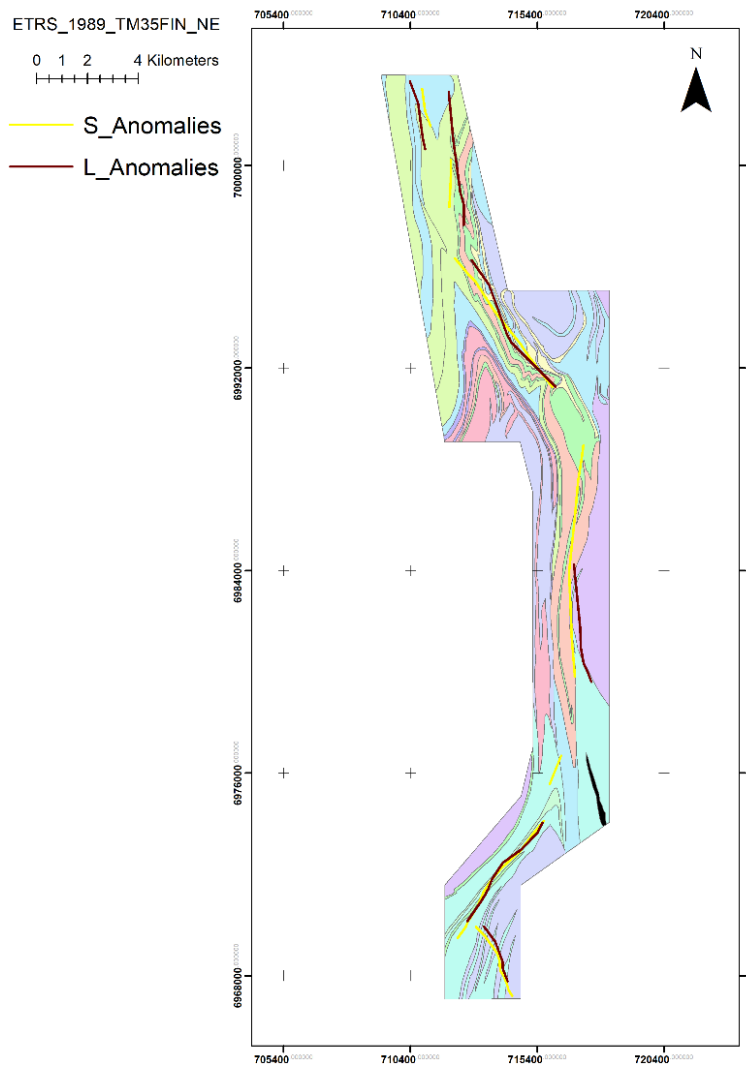


Fig. 5.14. Gold anomaly zones for soil and bedrock.

5.7. THREE-DIMENSIONAL (3-D) GEOLOGICAL MODELLING

The primordial phase of the 3-D modeling process in Vulcan involved the creation of a new project file (.dgl), with accurate coordinates of the area and the generation of a design file (.isis) that will comprise all the layers with the geological information.

5.7.1. 3-D Topography

The first element to be illustrated is the 3D topographical surface of the HSB. The topography shape file (.shp) containing elevation contours with 10-meter interval (Fig. 5.15). The produced topographic relief is a triangulation surface model. The 3-D generated surface changes color based on the Z-axis, showing no extreme high and variances. The topographical 3-D features have a key-role for in defining the elevation (z value) that all the upcoming geospatial data encompass.

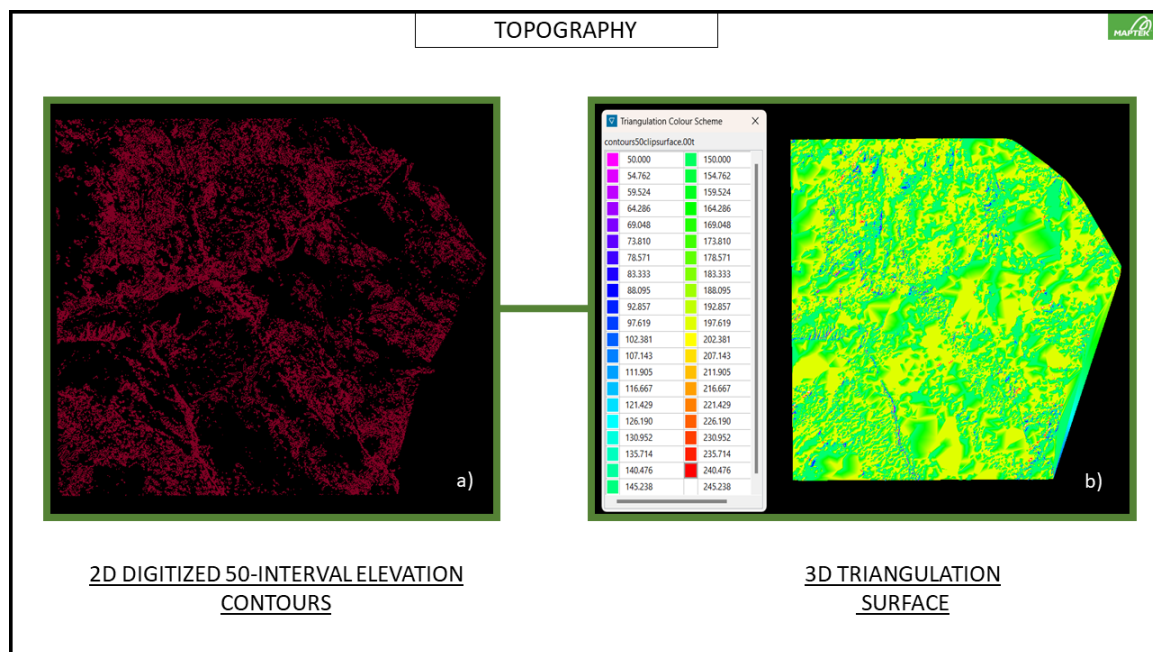


Fig. 5.15. 10m-elevation contours and topographical triangulation surface.

5.7.2. 3-D lithological model

Since the granitoid intrusive units envelope all other greenschist rocks, and occupy the largest part of the belt, these were modeled to represent the 3-D lithological map. 3-D model of the intrusive granitoid rocks and their classification is shown in Figure 5.16. The modelling involved a 2-D representation of the intrusive units as polygons, and by utilizing dip and strike information for the intrusions based on Sorjonen-Ward (1993) and unpublished report from Sakellaris (2016), these were extended into 3D.



Fig. 5.16. 3-D model of the intrusive granitoid rocks and their classification.

5.7.3. 3-D structural map

The most significant geological features that influence gold mineralization in the HSB are the major NE-SW and N-S high strain zones, along with the secondary, and equally important, E-W trending faults. Every 2-D polyline shape file was transformed into a fault surface utilizing the Fault Manipulation tool in Vulcan by assigning depth and dip value. These parameters were determined with reference to drilling information, cross-sections, and unpublished reports.

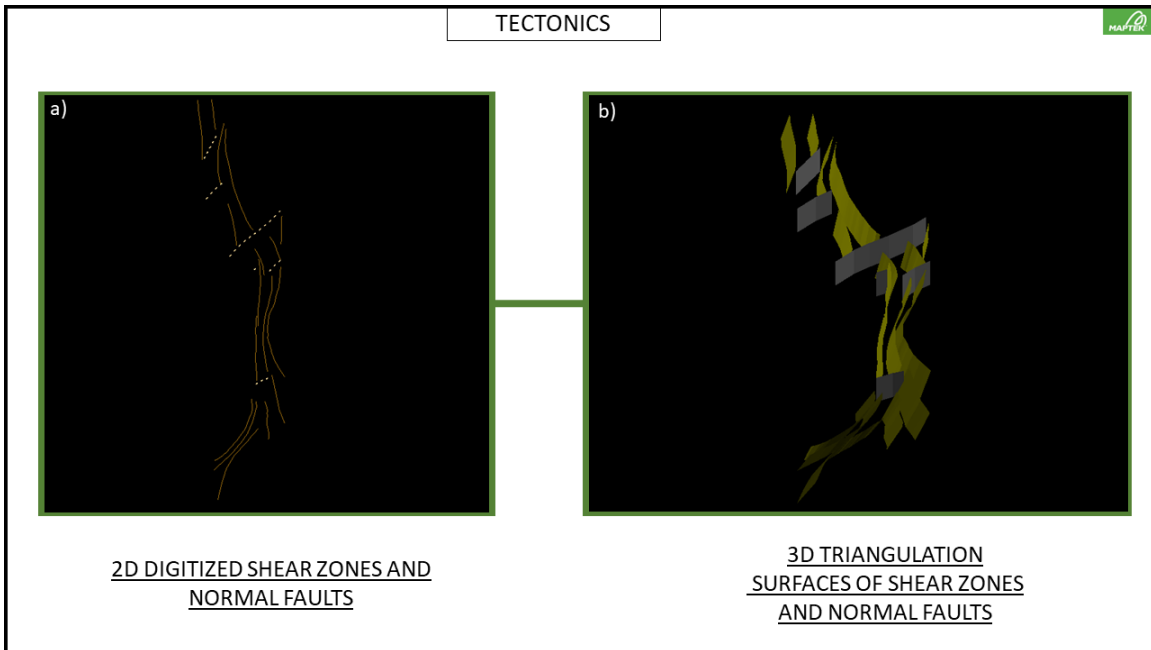


Fig. 5.17. 2-D N-S shear zones and E-W faults and their 3-D triangulation surfaces.

5.7.4. Geochemical data

The digitized surface geochemical anomaly lineaments were imported in the 3-D model. Two distinct polyline layers were created in Vulcan illustrating the digitized lines of geochemical anomalies for soil and lithology geochemistry (Fig. 5.18).

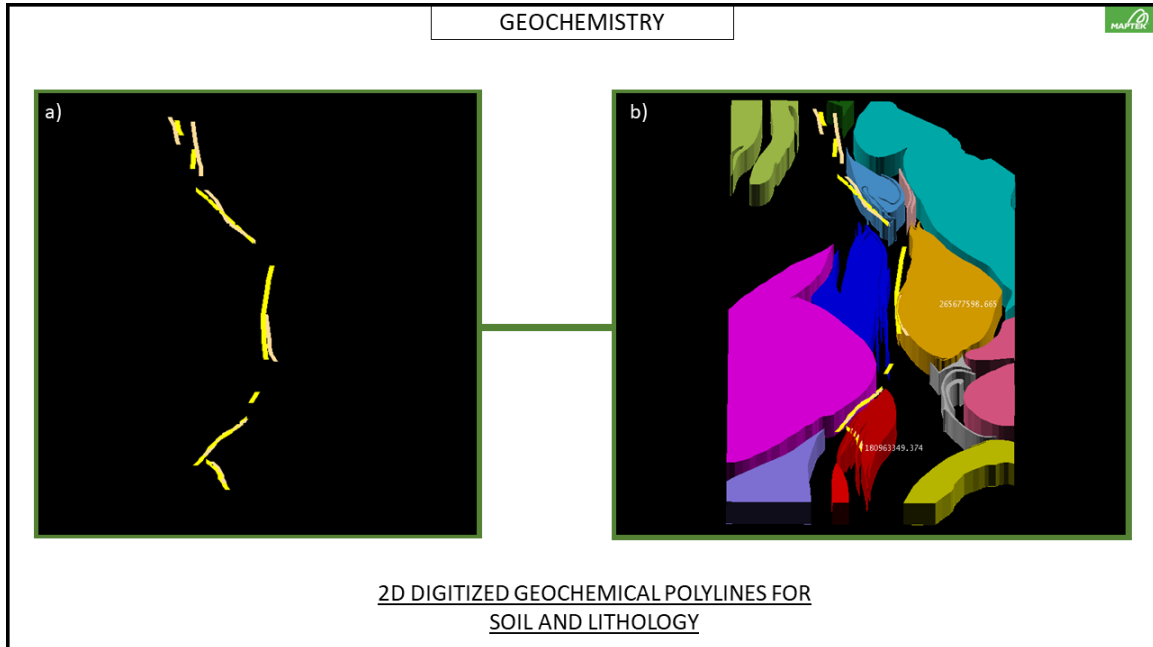


Fig. 5.18. Surface geochemical anomaly lineaments in Vulcan.

5.7.5. Drill hole data

The drill hole data were imported and visualized in the 3-D model for spatial comparison with the surface geochemical data. To import the drills into the software, the excel files which include details about collar, survey, lithology and assays were converted and imported as CSV databases and a new database (.dhd) was created.

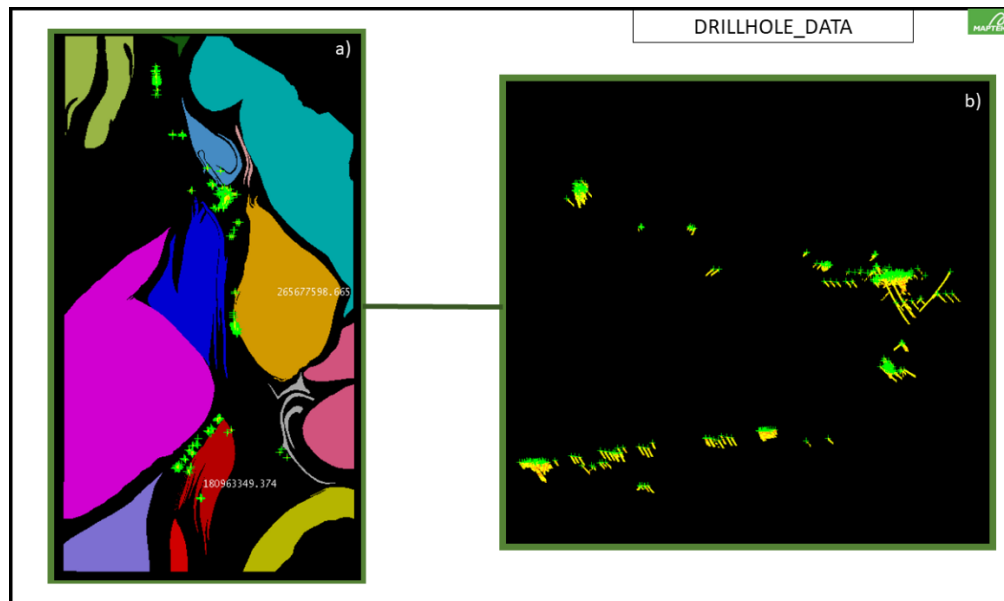


Fig. 5.19. Drillhole projection.

5.8. 3-D GEOLOGICAL MODEL AND GEOCHEMICAL ANOMALY MAP

All the available geological information was imported in the 3-D software and the 3-D geological model was created (Fig. 5.20). Examining the complete 3-D model, it is made clear that the geochemical anomalies are positioned into the Hattu Supersequence rocks. It is apparent that the intrusive units work as the boundary in which the gold geochemical anomalies cease. These intrusive units encircle the rest of the rock units, which include metasediments, mafic and volcanic rocks where the anomalies are positioned. The Kuittila prospect remains an exception as its gold distribution is vertically to the southern Kuittila Tonalite veins.

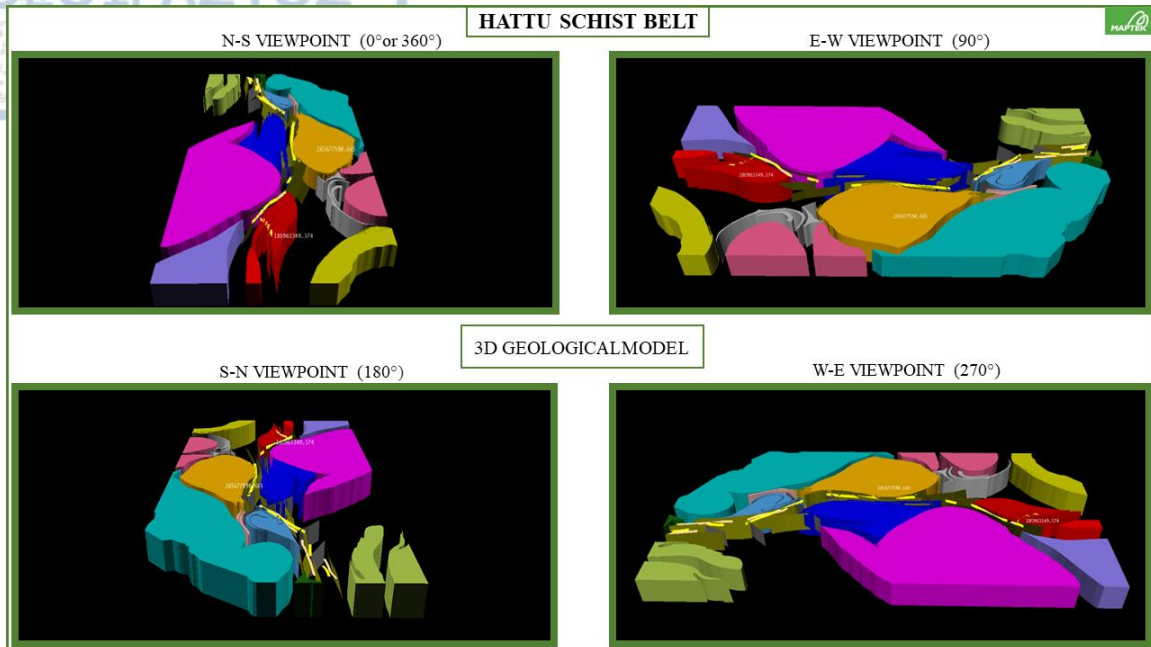
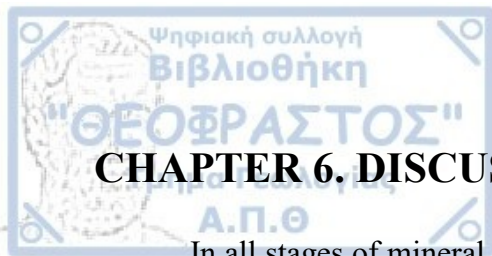


Fig. 5.20. Final 3-D geological model for HSB integrating all the geospatial information.

As highlighted in the 3-D model a number of geochemical anomalies are situated in the contact of the Viluvaara and Korpivaara intrusions within the metasediments. It is also likely to find gold distributed in the eastern parts of those intrusions, but its presence within them seems limited. The tectonic setting is more understandable and the directionality of the geochemical anomalies parallel to the shear zones and vertical to the normal faults is more pronounced in the 3-D model. As Nurmi (1993) stated, the Hattu schist belt could be considered as a crustal scale mineralizing system functioned for 40 km.



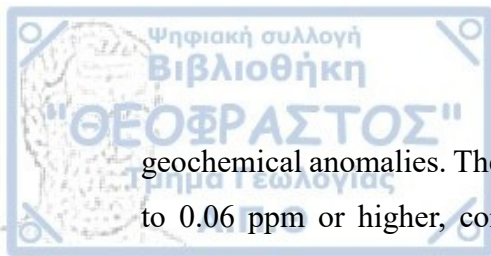
CHAPTER 6. DISCUSSION AND CONCLUSIONS

In all stages of mineral exploration, geological, geochemical and geophysical data are gathered constantly from the early stage of exploration to the latest stage of extraction, and resource update. Among the most crucial and challenging tasks of an exploration geologist is how geochemical data from field surveys and drilling campaigns are gathered, processed, interpreted and evaluated, in order to be used as a predictor for mineral prospectivity. Either in the first stages of exploration or during the production of a mine. For this study, a mature ore district area such this of the Hattu Belt was selected to test different statistical, geostatistical and interpolation methods in order to define the gold-element anomaly in the soil and bedrock.

6.1. STATISTICAL ANALYSES AND THRESHOLD ESTIMATION

Prior to threshold estimation and map visualization of the geochemical data, the dataset has been thoroughly checked for any inconsistencies, errors and censored values, which were removed from the database.

1. Both descriptive statistics and histograms, Q-Q plots and boxplots reveal that gold dataset is extremely positively skewed. This is common in gold deposits since only a small portion of the geochemical analysis is considered high grade where most gold contents range from low ppm to considerable ppb, in comparison to Fe-deposits which typically exhibit negative skewness. Statistical and geostatistical analyses in log-transformed (for threshold estimation) and non-transformed (for variography) and data, successfully identified the outliers that required removal, contributing to the improvement of both threshold estimation and variography procedures.
2. Three different threshold estimators were applied, namely the mean $\pm 2\text{DEV}$, the median $\pm 2\text{MAD}$ and the Upper Whisker (UW) methods. The extremely positive-skewed nature of the dataset proves the mean $\pm 2\text{DEV}$ method to be unreliable. The median $\pm \text{MAD}$ delivered more ideal and lower thresholds than the Upper Whisker (UW) method. The values obtained are 0.027 ppm for soil samples and 0.057 ppm for bedrock samples, resulting in the identification of numerous minor and major gold



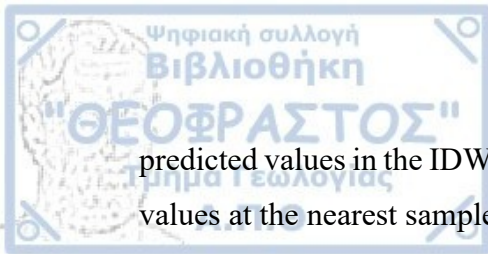
geochemical anomalies. These findings align well with the recommended range of 0.02 to 0.06 ppm or higher, commonly employed in reconnaissance sampling programs (Xuejing and Xueqiu, 1990), but also in earlier till geochemical anomaly mapping in the HSB.

What could contribute further to this part, is to evaluate the effectiveness of the EDA method along with other techniques or in a wider context to perform a multivariate geochemical anomaly analysis. Some of the most widely employed techniques include the cumulative probability plots (Sinclair, 1974), fractal and multifractal analysis (Cheng. et al., 1994, 2010, Youssefi and Carranza, 2015) Principal Components Analysis (PCA) or Robust Principal Components Analysis (RPCA) (Zuo et al., 2013) among others. This is because geochemical anomaly mapping is easier when pathfinder elements of gold are used in a multivariate geochemical anomaly mapping. These often present a normal distribution pattern. For the till and lithological geochemistry of the HSB, the most promising pathfinder elements of gold are the Te, Bi, Ag and to a minor degree Cu (Bornhorst and Rasilainen, 1993). These correlations align with what is observed in other orogenic gold districts (Nurmi et al., 1991).

6.2. SPATIAL INTERPOLATION

Two distinct interpolation techniques were applied in the HSB, the Ordinary Kriging and Inverse Distance Weighting. It was evident that both methods were able to map the gold geochemical anomalies and identify geochemical patterns in the area.

1. It is difficult to pick a single method that accomplished the anomaly mapping better than the other, since their interpolation results, their validation and the areas pointed out with significant geochemical anomalies are quite identical.
2. The deterministic IDW is more straightforward and can be generated much faster and easier than OK.
3. With IDW, the anomaly contrast resolution is higher in the soil distribution maps, resulting in broader generalizations and more distinct circular contour bands. The



predicted values in the IDW geochemical maps were notably influenced by the absolute values at the nearest sample point to the point being predicted.

4. The geostatistical OK is considered as the best linear unbiased estimator since it considers the spatial autocorrelation and fits a function model that represents better the spatial structure of the variable. Anisotropy was also identified during the variography and since there is no trend in the data, geological structures (e.g. shear zones) may be responsible for the presence of anisotropy in HSB. This is a feature that with the IDW would go unnoticed and clearly helped to reduce the OK prediction errors effectively. In bedrock geochemical anomaly maps of OK and IDW there are no major differences since they depict almost the same geochemical anomaly areas.
5. Various studies show that Kriging yields favorable outcomes with a small number of samples (tens to hundreds), while IDW generally produces satisfactory results for spatial distribution maps when the sample number (thousands) and density becomes larger (Xu and Zhang, 2023). This study corresponds with these statements, indicating that IDW performed better in the lithology dataset with a larger number of samples. For both methods, three important factors (optimality, validity and known occurrences) were reviewed.
6. Since the spatial distribution maps rely on spatial interpolation using estimated values., their interpretation should be approached with caution and their outcomes should be considered as “probable” values, rather than definitive “true” values (Zhang et al., 2021).
7. This study is a strong indicator that data transformation is not always mandatory as it stands in the published methodology. First, because the objective is prediction, hence, accurate prediction on the original scale of measurement is preferred, and secondly, any application of data transformation had unfavorable outcomes in variography such as absence of spatial autocorrelation, which may lead to a lack of recognition of geochemical anomalies.

The highly advanced tools that GIS software offers could add more to the interpolation results of this study. Except for OK and IDW, ArcGIS supplies the user with many interpolation methods such as the Radial Basis Function (RBF), Global Polynomial Interpolation (GPO) or several subdivisions of Kriging.



6.3. GEOCHEMICAL PREDICTION MAP

The geochemical anomaly maps for both soil and bedrock revealed some long and continuous zones along with smaller but also significant zones with encouraging gold contents.

1. The interpretation of the gold prediction maps revealed that the prospect zones share common characteristics. All prospect zones are situated within the schistose rocks of the Hattu Supersequence and not within the intrusive units. All geochemical anomalies are positioned along the contact of the intrusions (e.g. Viluvaara) with the metasediments. In addition, as expected in orogenic gold deposits, the geochemical anomalies are following (for many kilometers) the direction of the NE-SW high strain zones, while the impact of the minor E-W in the distribution of gold is noticeable. These patterns are followed throughout the extent of the belt from Hosko until the Kuittila zone.
2. Four continuous gold zones are identified. The most prominent continuous gold geochemical anomalies are located in the Kuittila and Pampalo zone. Weaker zones occur in Hosko and Hattuvaara zones, while the range of the anomalous zone fluctuates mostly from 5 to 10 km. The interpolation results coincide with many of the known gold occurrences in HSB. For instance, the Pampalo mine was discernible in the geochemical anomaly mapping, while the Kuittila prospects are clearly promising for drilling.
3. One unclarified subject is the absence of geochemical anomalies in Rämepuro and Hosko deposits. From early phases of till geochemistry was already known that the Rämepuro deposit was poorly reflected in geochemical anomalies (Hartikainen and Nurmi, 1993). The present observations demonstrate that the Hosko and Rämepuro deposits are convincing evidence that not all the gold deposits inevitably need to indicate any distinct till geochemical anomaly. Consequently, geochemical data indications should be interpreted with caution in conjunction with other geological, geophysical, structural observations etc. and cooperate for the selection of drilling targets.



6.4. 3-D GEOLOGICAL MODELLING

A detailed 3-D geological model of the area was constructed that revealed the subsurface geological architecture, structural geometry, and gold mineralization. The combination of the surface gold anomaly maps made feasible the spatial correlation between the gold dispersion in the soil and the exact position of the subsurface mineralization (from drill cores).

1. The direction of all gold anomaly zones is parallel to the major shear zones and vertical to the E-W normal faults of the area.
2. The location of most geochemical anomalies is within 500 meters west of major granitoid plutons within the schistose rocks of the Hattu Supersequence. They are further related to small feldspar porphyry intrusions.
3. The dispersion of the gold element in the soil is very narrow, being between 30 to 200 meters from the source rock.
4. The 3D integrated geological model of this study provides evidence that the Hattu schist belt can be characterized as a single crustal scale mineralizing system.

6.5. FURTHER WORK

The data produced in this work together with the presence of a solid conceptual model of the mineralization, can be combined with other geospatial data i.e. geophysical, radiometric, etc. in order to perform a mineral prospectivity analysis. Widely used data-driven modelling methods include the weights of evidence and logistic regression whereas common knowledge driven are the fuzzy logic, evidential-belief theory etc. Supervised machine learning algorithms like artificial neural networks and random forest classification and their variates comprise novel data-driven methods of MPM, rapidly developed in the last decade characterized by their advantage in recognizing patterns without previous knowledge of the area. Application of these methods could produce an updated exploration model and a gold prospectivity map for the Hattu belt area could dictate guidelines for future exploration for the discovery of concealed gold deposits.



Agterberg, F.P., 1989. Computer programs for mineral exploration. *Science* 245(4913): 76-81.

Airo, M.-L. 2007. Application of Aerogeophysical Data for Gold Exploration: Implications for Central Lapland Greenstone Belt. In: Ojala, J. V. (ed.) *Gold in the Central Lapland Greenstone Belt, Finland*. Geological Survey of Finland, Special Paper 44, 171–192.

Airo, M.-L. & Mertanen, S. 2008. Magnetic signatures related to orogenic gold mineralization, Central Lapland Greenstone Belt, Finland. *Journal of Applied Geophysics* 64, 14–24.

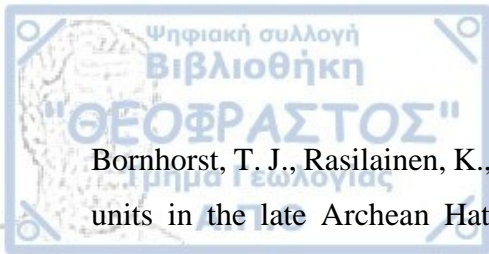
Aitchison, J., 1986. *The Statistical Analysis of Compositional Data*. Chapman and Hall, London, 416 pp.

Ander, E.L., Johnson, C.C., Cave, M.R., Palumbo-Roe, B., Nathanail, C.P., Lark, R.M., 2013. Methodology for the determination of normal background concentrations of contaminants in English soil. *Science of The Total Environment*, 454-455, 604–618.

Baker T., 2002. Emplacement depth and CO₂-rich fluid inclusions in intrusion-related gold deposits. *Econ Geol* 97:1109–1115

Bárdossy, A., 1997. Introduction to geostatistics. Institute of Hydraulic Engineering, University of Stuttgart, 28-32.

Biernacik, P., Kazimierski, W., Włodarczyk-Sielicka, M., 2023. Comparative Analysis of Selected Geostatistical Methods for Bottom Surface Modeling. *Sensors*, 23(8), 3941.



Bornhorst, T. J., Rasilainen, K., & Nurmi, P. A., 1993. Geochemical character of lithologic units in the late Archean Hattu schist belt, Ilomantsi, eastern Finland. Nurmi, PA & Sorjonen-Ward, P.(eds.), 133-145.

Bornhorst, T.J., Rasilainen, K., 1993. Mass transfer during hydrothermal alteration associated with Au mineralisation within the Late Archean Hattu schist belt, Ilomantsi, eastern Finland. Geological Survey of Finland, Special Paper 17, pp. 273–289

Bounessah, M., Atkin, B.P., 2003. An application of exploratory data analysis (EDA) as a robust non-parametric technique for geochemical mapping in a semi-arid climate. Applied Geochemistry 18(8): 1185–1195.

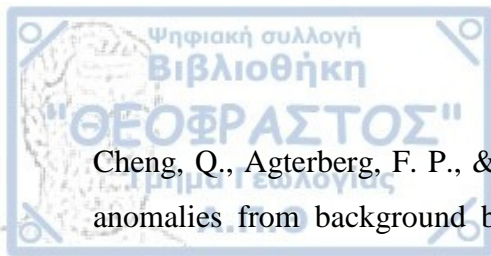
Burrough, P.A., 1987. Principles of Geographic Information Systems for Land Resource Assessment. Clarendon Press, Oxford.

Burrough, P.A. and McDonnell, R.A., 1998. Principles of Geographical Information Systems, Oxford, Oxford University Press, 330 pp.

Cambardella, C.A., Moorman, T.B., Novak, J.M., Parkin, T.B., Karlen, D.L., Turco, R. F., Konopka, A.E., 1994. Field-scale variability of soil properties in central Iowa soils. Soil Science Society of America Journal, 58(5), 1501-1511.

Carranza, E.J.M., 2009, Geochemical Anomaly and Mineral Prospectivity Mapping in GIS, Handbook of Exploration and Environmental Geochemistry, Vol. 11 (M. Hale, Editor). Elsevier, Amsterdam

Chambers, J.M., Cleveland, W.S., Kleiner, B. and Tukey, P.A., 1983 Graphical Methods for Data Analysis. Wadsworth International Group, Belmont, California, Duxbury Press, Boston.



Cheng, Q., Agterberg, F. P., & Ballantyne, S. B. (1994). The separation of geochemical anomalies from background by fractal methods. *Journal of Geochemical exploration*, 51(2), 109-130.

Cowan, E J, Beatson, R K, Ross, H J, Fright, W R, McLennan, T J and Mitchell, T J, 2002. Rapid geological modelling, in *Applied Structural Geology for Mineral Exploration and Mining, International Symposium Abstract Volume* (ed: S Vearnecombe), Australian Institute of Geoscientists Bulletin, 36:39-41

Cowan, E J, Beatson, R K, Ross, H J, Fright, W R, McLennan, T J, Evans, T R, Carr, J C, Lane, R G, Bright, D V, Gillman, A J, Oshust, P A and Titley, M, 2003. Practical implicit geological modelling, in *Proceedings Fifth International Mining Geology Conference*, pp 89-99 (The Australasian Institute of Mining and Metallurgy: Melbourne).

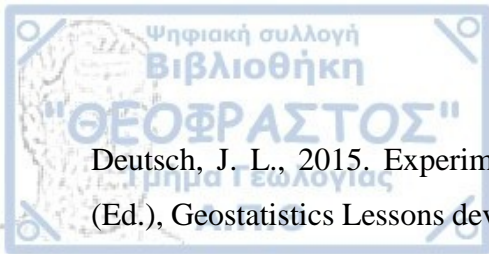
Cowan, E.J., Spragg, K.J., Everitt, M.R., 2011. Wireframe-free geological modelling—an oxymoron or a value proposition? In *Eighth international mining geology conference*. Australasian Institute of Mining and Metallurgy, Queenstown, New Zealand, pp. 247-260.

Cox, S. F., Etheridge, M. A., Cas, R. A. F., & Clifford, B. A. (1991). Deformational style of the Castlemaine area, Bendigo-Ballararat Zone: Implications for evolution of crustal structure in central Victoria. *Australian Journal of Earth Sciences*, 38(2), 151-170.

Cox, S.F., Knackstedt MA, Braun J (2001) Principles of structural control on permeability and fluid flow in hydrothermal systems. *Rev Econ Geol* 14:1–24

Cressie, N.A.C., 1993. *Statistics for spatial data*, revised edition. New York: Wiley.

Deutsch, C.V., 2003. Geostatistics. Ed(s): Meyers, R.A., *Encyclopedia of Physical Science and Technology* (Third Edition), Academic Press, p. 697-707.



Deutsch, J. L., 2015. Experimental Variogram Tolerance Parameters. In J. L. Deutsch (Ed.), *Geostatistics Lessons developments*. Journal of Geochemical Exploration 21(1): 41-61.

Eilu, P., Sorjonen-Ward, P., Nurmi, P., Niiranen, T., 2003. A review of gold mineralization styles in Finland. *Econ. Geol.* 98, 1329–1353

Eilu, P., 2015.: Overview on gold deposits in Finland, in: *Mineral Deposits of Finland*, edited by: Maier, W. D., O'Brien, H., Lahtinen, R., Elsevier, Amsterdam, 377–403.

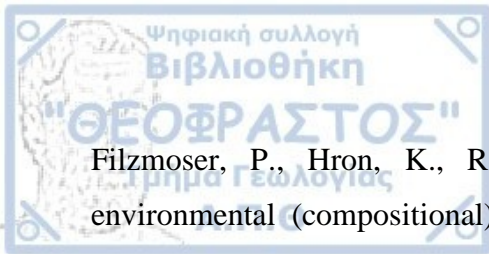
Eilu, P. (2011). *Metallic mineral resources of Fennoscandia*. Geological Survey of Finland: Special Paper, 49, 13-21.

Eilu, P., Rasilainen, K., Halkoaho, T., Huovinen, I., Kärkkäinen, N., Kontoniemi, O., Lepisto, K., Niiranen, T. & Sorjonen-Ward, P. 2015. Quantitative assessment of undiscovered resources in orogenic gold deposits in Finland. Geological Survey of Finland, Report of Investigation 216. 318 p.

Egozcue, J. J., Pawlowsky-Glahn, V., Mateu-Figueras, G., & Barcelo-Vidal, C. (2003). Isometric logratio transformations for compositional data analysis. *Mathematical geology*, 35(3), 279-300.

Dong, Y., & Santosh, M. (2016). Tectonic architecture and multiple orogeny of the Qinling Orogenic Belt, Central China. *Gondwana Research*, 29(1), 1-40.

Fan, H. R., Hu, F. F., Yang, J. H., Shen, K., & Zhai, M. G. (2005). Fluid evolution and large-scale gold metallogeny during Mesozoic tectonic transition in the eastern Shandong province. *Acta Petrologica Sinica*, 21(5), 1317-1328.



Filzmoser, P., Hron, K., Reimann, C., 2009b. Univariate statistical analysis of environmental (compositional) data: problems and possibilities. *Science of the Total Environment* 407, 6100–6108.

Frimmel, H.E., 2008. Earth's Continental Crustal Gold Endowment. *Earth and Planetary Science Letters*, 267, 45-55.

Fusswinkel, T., Wagner, T., Sakellaris, G. 2017. Fluid evolution of the Neoproterozoic Pampalo orogenic gold deposit (E Finland): Constraints from LA-ICPMS fluid inclusion microanalysis. *Chemical Geology* 450, pp. 96-121.

Fyfe WS, Price NJ, Thompson AB (1978) *Fluids in the Earth's crust*. Elsevier, Amsterdam 383 p

Garrett, R. G. 1991. The Management, Analysis and Display of Exploration Geochemical Data, *Exploration Geochemistry Workshop*. Geological Survey of Canada Open File 2390, Paper 9, 9-1 to 9-4.

Garrett, R.G., Kane, V.E., Zeigler, R.K., 1980. The management and analysis of regional geochemical data. *Journal of Geochemical Exploration* 13(2-3): 115-152

Gebre-Mariam M., Hagemann S.G., Groves D.I., 1995. A classification scheme for epigenetic Archean lode-gold deposits. *Mineral Deposita* 30:408–410

Goldfarb R.J., Groves D.I., Gardoll S., 2001. Orogenic gold and geologic time: a global synthesis. *Ore Geol Rev* 18:1–75

Goldfarb, R. J., & Santosh, M. (2014). The dilemma of the Jiaodong gold deposits: Are they unique?. *Geoscience Frontiers*, 5(2), 139-153.



Goldfarb R.J., Hart C.J.R., Marsh E.E., 2008. Orogenic gold and evolution of the Cordilleran orogeny. In: Spencer JE, Titley SR (eds) CircumPacific Tectonics, Geologic Evolution, and Ore Deposits, vol 22. Tucson Ariz Geol Soc Digest, Tucson, pp 311–323

Goldfarb R.J., Groves D.I., 2015. Orogenic gold: common vs evolving fluid and metal sources through time. *Lithos* 223:2–26

Goovaerts, P., 1997. *Geostatistics for Natural Resources Evaluation*. Oxford University

Groves D.I., 1993. The crustal continuum model for late-Archaean lode gold deposits of the Yilgarn block, Western Australia. *Mineral Deposita* 28:366–374

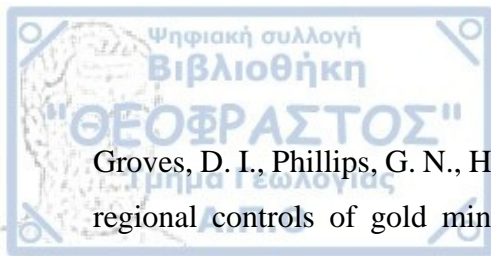
Groves, D. I., Phillips, G. N., Ho, S. E., Houstoun, S. M., & Standing, C. A. (1987). Craton-scale distribution of Archean greenstone gold deposits; predictive capacity of the metamorphic model. *Economic Geology*, 82(8), 2045-2058.

Groves, D. I., Goldfarb, R. J., Gebre-Mariam, M., Hagemann, S. G., & Robert, F. (1998). Orogenic gold deposits: a proposed classification in the context of their crustal distribution and relationship to other gold deposit types. *Ore geology reviews*, 13(1-5), 7-27.

Groves, D. I., Santosh, M., Deng, J., Wang, Q., Yang, L., & Zhang, L. (2020). A holistic model for the origin of orogenic gold deposits and its implications for exploration. *Mineralium Deposita*, 55, 275-292.

Groves, D. I., & Santosh, M. (2015). Province-scale commonalities of some world-class gold deposits: implications for mineral exploration. *Geoscience Frontiers*, 6(3), 389-399.

Groves, D. I., Santosh, M., Goldfarb, R. J., & Zhang, L. (2018). Structural geometry of orogenic gold deposits: Implications for exploration of world-class and giant deposits. *Geoscience Frontiers*, 9(4), 1163-1177.



Groves, D. I., Phillips, G. N., Ho, S. E., & Houstoun, S. M. (1985). The nature, genesis and regional controls of gold mineralization in Archaean greenstone belts of the Western Australian Shield; a brief review. *South African Journal of Geology*, 88(1), 135-148.

Groves, D.I. & Foster, R.P., 1991. Archaean lode gold deposits. In R.P. Foster (Editor), *Gold Metallogeny and Exploration*, Blackie and Son Ltd, Glasgow, 432 p

Groves D.I., Santosh M., 2016. The giant Jiaodong gold province: the key to a unified model for orogenic gold deposits? *Geosc Front* 7:409–418

Grünfeld, K., 2005. Dealing with outliers and censored values in multi-element geochemical data—a visualization approach using XmdvTool. *Applied Geochemistry*, 20(2), 341–352.

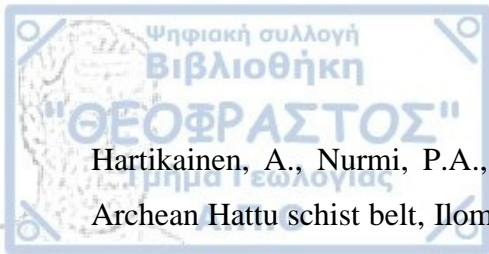
Hardy, R., 1971. Multiquadric equations of topography and other irregular surfaces.

Harris, J.R., Wilkinson, L., Grunsky, E., Heather, K., Ayer, J., 1999. Techniques for analysis and visualization of litho-geochemical data with applications to the Swayze greenstone belt, Ontario. *Journal of Geochemical Exploration* 67(1-3): 301-334.

Harris, J.R., Wilkinson, L., Bernier, M., 2001. Analysis of geochemical data for mineral exploration using a GIS – a case study from the Swayze greenstone belt, northern Ontario, Canada. In:

McClenaghan, M.B., Borrowsky, P.T., Hall, G.E.M., Cook, S.J. (Eds.), *Drift Exploration in Glaciated Terrain*, Geological Society, London, Special Publications 2001, 185: 165-200.

Hartikainen, A., Damstén, M., 1991. Applications of till geochemistry to gold exploration in Ilomantsi, Finland. *Journal of Geochemical Exploration* 39, 323–342.



Hartikainen, A., Nurmi, P.A., 1993. Till geochemistry in gold exploration in the late Archean Hattu schist belt, Ilomantsi, eastern Finland. In: Nurmi, P.A., Sorjonen-Ward, P. (Eds.), Geological Development, Gold Mineralization and Exploration Methods in the Late Archean Hattu Schist Belt, Ilomantsi, Eastern Finland, Geological Survey of Finland, Special Paper 17, 323–352.

Hartikainen, A., Salminen, R., 1982. Tohmajärven karttalehtialueen geokemiallisen kartoituksen tulokset. Summary: The results of the geochemical survey in the Tohmajärvi map-sheet area. Geologian Tutkimuslaitos, Geokemiallisten karttojen selitykset, Lehti 4232. Geological Survey of Finland, Explanatory Notes to Geochemical Maps, Sheet 4232, p. 57.

Hartkamp, A.D., De Beurs, K., Stein, A., White, J.W., 1999. Interpolation Techniques for Climate Variables. NRG-GIS Series 99-01. Mexico, D.F.: CIMMYT.

Haslett, J., Bradley, R., Craig, P., Unwin, A., Wills, G., 1991. Dynamic graphics for exploration spatial data with application to locating global and local anomalies. The American Statistician 45(3): 234-242.

Hauptfleisch, M., Putniņš, T. J., & Lucey, B. (2016). Who sets the price of gold? London or New York. Journal of Futures Markets, 36(6), 564-586.

Hawkes, H.E., and Webb, J.S., 1962 Geochemistry in Mineral Exploration. (pp. 1–415). New York: Harper & Row.

Hedenquist J.W., Lowenstern J.R., 1994. The role of magmas in the formation of hydrothermal ore deposits. Nature 370:519–527

Heino, T., Hartikainen, A., Koistinen, E., Niskanen, M. 1995. Report on exploration in Ilomantsi in 1992–1995. Geological Survey of Finland. Unpublished report M06/4333/-95/1/10, p. 17.



Hengl, T., 2007. A Practical Guide to Geostatistical Mapping of Environmental Variables. JRC Scientific and Technical Reports. Office for Official Publication of the European Communities, Luxembourg.

Hölttä, P., Heilimo, E., Huhma, H., Juopperi, H., Kontinen, A., Konnunaho, H., Lauri, L., Mikkola, P., Paavola, J. & Sorjonen-Ward, P. 2012. Archaean complexes of the Karelia Province in Finland. Geological Survey of Finland, Special Paper 54, 9–20

Hölttä, P., Lehtonen, E., Lahaye, Y. & Sorjonen-Ward, P. 2017. Metamorphic evolution of the Ilomantsi greenstone belt in the Archaean Karelia Province, eastern Finland. In: Halla, J., Whitehouse, M., Ahmad, T. & Bagai, Z. (eds) Crust–Mantle Interactions and Granitoid diversification: Insights from Archaean Cratons. Geological Society Special Publications 449, 231-250

Huhma, H., O'Brien, H., Lahaye, Y., & Mänttari, I. (2011). Isotope geology and Fennoscandian lithosphere evolution. Geological Survey of Finland, Special Paper, 49, 35-48.

Huhma, H., Mänttari, I., Peltonen, P., Kontinen, A., Halkoaho, T., Hanski, E., et al., 2012. The age of the Archaean greenstone belts in Finland. Geological Survey of Finland, Special Paper 54, 74–175.

Hughes M.J., Phillips G.N., Gregory L.M., 1997. Mineralogical domains in the Victorian gold province, Maldon, and Carlin-style potential. Australas Instit Min Metall, Ann Conf Melbourne, pp 215–227

Isaaks, E.H., Srivastava, R.M., 1989. An introduction to applied geostatistics. Oxford University Press, Oxford



Jessell, M., Aillères, L., De Kemp, E., Lindsay, M., Wellmann, F., Hillier, M., Laurent, G., Carmichael, T., & Martin, R., 2014. Next Generation Three-Dimensional Geologic Modeling and Inversion. In Society of Economic Geologists Special Publication 18: Building Exploration Capability for the 21st Century. Vol. 18, pp. 261-272.

Johnston, K., Ver Hoef, J.M., Krivoruchko, K., Lucas, N., 2003. The principles of geostatistical analysis, Using ArcGIS geostatistical Anal., ESRI, Redlands, CA pp. 4980.

Joseph, I., Bhaumik, B.K., 1997. Improved estimation of the Box-Cox transform parameter and its application to hydrogeochemical data. *Mathematical Geology* 29(8): 963-976.

Journal of Geophysical Research 76, 1905–1915.

Kalliomäki, H., Wagner, T., Fusswinkel, T., & Schultze, D. (2019). Textural evolution and trace element chemistry of hydrothermal calcites from Archean gold deposits in the Hattu schist belt, eastern Finland: indicators of the ore-forming environment. *Ore Geology Reviews*, 112, 103006.

Käpyaho, A., Hölttä, P., Whitehouse, M.J., 2007. U-Pb zircon geochronology of selected Archean migmatites in eastern Finland. *Bulletin of the Geological Society of Finland* 78, 121–141.

Käpyaho, A., Molnár, F., Sakellaris, G., 2013. Mineralogical characteristics of a metasedimentary hosted Hosko gold deposit from the Archean Hattu schist belt, eastern Finland. In: *Mineral Deposit Research for a High-Tech World. Proceedings of the 12th Biennial SGA Meeting, August 12–15, Uppsala, pp. 1120–1123, Sweden*

Kerrick, R. (1983). Geochemistry of gold deposits in the Abitibi greenstone belt. *Can. Inst. Mining Metall. Spec.*, 27, 75.

Kerry, R., & Oliver, M. A. (2007a). Determining the effect of asymmetric data on the variogram. I. Underlying asymmetry. *Computers & Geosciences*, 33, 1212–1232.



Kojonen, K., Johanson, B., O'Brien, H.E., Pakkanen, L., 1993. Mineralogy of gold occurrences in the late Archaean Hattu schist belt, Ilomantsi, eastern Finland. Geological Survey of Finland, Special Paper 17, 233–271.

Kontak D.J., & Kerrich R., (1995), Geological and geochemical studies of a metaturbidite-hosted lode gold deposit—the Beaver Dam deposit, Nova Scotia—II. Isotopic studies. *Econ Geol* 90:885–901.

Khoshnaw F.M., 2012. *Petroleum and Mineral Resources*. WIT press, Southampton.

Kotz, S., Johnson, N.L., 1985. *Encyclopedia of Statistical Sciences*, Volume 3, John Wiley & Sons, New York.

Koutsopoulos, K., 2017. *Geographic Information Systems & Spatial Analysis*

Krige, D. G., 1951. A statistical approach to some basic mine valuation problems on the Witwatersrand. *Journal of the Southern African Institute of Mining and Metallurgy*, 52(6), 119-139.

Kürzl, H., 1988. Exploratory data analysis: recent advances for the interpretation of geochemical data. *Journal of Geochemical Exploration* 30(1-3): 309-322.

Lahtinen, R., Hölttä, P., Kontinen, A., Niiranen, T., Nironen, M., Saalman, K., SorjonenWard, P., 2011. Tectonic and metallogenic evolution of the Fennoscandian Shield: key questions with emphasis on Finland. *Geol. Surv. Finland Spec. Pap.* 49, 23–33.

Levinson, A.A., 1974. *Introduction to Exploration Geochemistry*, Applied Publishing Ltd., Calgary.



Li, J., Heap, A.D., 2008. A Review of Spatial Interpolation Methods for Environmental

Mc Keag S.A, Craw D., 1989. Contrasting fluids in gold-bearing quartz vein systems formed progressively in a rising metamorphic belt Otago Schist, New Zealand. *Econ Geol* 84:22–33

Matheron, G., 1963. *Les variables régionalisées et leur estimation*. Paris: Masson.

Matheron, G., 1965. Principles of geostatistics. *Economic geology*, 58(8), 1246-1266.

Meyer, M., & Saager, R. (1985). The gold content of some Archaean rocks and their possible relationship to epigenetic gold-quartz vein deposits. *Mineralium deposita*, 20, 284-289.

Miesch, A. T., 1977, Log transformations in geochemistry: *Mathematical Geology* v. 9(2), p. 191–194.

Molnár, F., O'Brien, H.E., Lahaye, Y., Käpyaho, A., Sorjonen-Ward, P., Hyodo, H., Sakellaris, G., 2016. Signatures of Overprinting Mineralization Processes in the Orogenic Gold Deposit of the Pampalo Mine, Hattu Schist Belt, Eastern Finland. *Society of Economic Geologists, Inc. Economic Geology*, v. 111, pp. 1659–1703.

Moon, C. J., Whateley, M. K., & Evans, A. M. (2006). *Introduction to mineral exploration* (No. Ed. 2). Blackwell publishing.

Mutanen, T., & Huhma, H. (2003). The 3.5 Ga Siurua trondhjemite gneiss in the Archaean Pudasjarvi granulite belt, northern Finland. *Bulletin-geological society of Finland*, 75(1/2), 51-68.

Myers, D. E., 1989. To be or not to be... stationary? That is the question. *Mathematical Geology*, 21, 347-362.



Nazarpour A, Rashidnejad Omran N, Rostami Paydar Gh, Sadeghi B, Matroud F, Mehrbinejad A (2015) Application of classical statistics, logratio transformation and multifractal approaches to delineate geochemical anomalies in the Zarshuran gold district, NW Iran. *Chemie der Erde* 75: 117-132.

Nenonen, J., & Huhta, P. (1993). Quaternary glacial history of the Hattu schist belt and adjacent parts of the Ilomantsi district, eastern Finland. *Geological Survey of Finland Special Paper*, 17, 185-191.

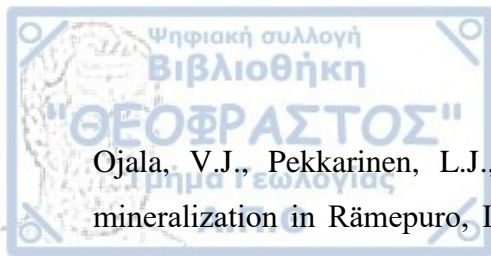
Nesbitt B.E., 1991. Phanerozoic gold deposits in tectonically active continental margins. In: Foster RP (ed) *Gold metallogeny and exploration*. Blackie and Son, Glasgow, pp 104–132

Nurmi, P.A., 1993. Genetic aspects of mesothermal gold mineralisation and implications for exploration in the late Archaean Hattu schist belt, Ilomantsi, eastern Finland. *Geological Survey of Finland, Special Paper 17*, pp. 373–386

Nurmi, P. A., & Sorjonen-Ward, P., (Editors), 1993. Geological development, gold mineralization and exploration methods in the late Archean Hattu schist belt, Ilomantsi, eastern Finland. *Geological Survey of Finland, Special Paper 17*, 386 pages, 196 figures, 60 tables, 5 appendices, and one appended map

Nurmi, P.A., Lestinen, P. & Niskavaara, H., 1991. Geochemical characteristics of mesothermal gold deposits in the Fennoscandian shield, and a comparison with selected Canadian and Australian deposits. *Geol. Surv. Finland, Bull.* 351, 101 p.

O'Brien, H.E., Nurmi, P.A., Karhu, J.A., 1993. Oxygen, hydrogen and strontium isotope compositions of gold mineralization in the late Archean Hattu schist belt, Ilomantsi, eastern Finland. *Geological Survey of Finland, Special Paper*, 17, 291–306.



Ojala, V.J., Pekkarinen, L.J., Piirainen, T., Tuukki, P., 1990. The Archaean gold mineralization in Rämepuro, Ilomantsi greenstone belt, eastern Finland. *Terra Nova* 2, 240–244.

Oliver, M. A., and Webster, R., 1987. The elucidation of soil pattern in the Wyre Forest of the West Midlands, England. II. Spatial distribution. *Journal of Soil Science*, 38, 293–307.

Oliver, M.A., Webster, R., 2015. *Basic Steps in Geostatistics: The Variogram and Kriging*. Springer International Publishing AG. on Mining Innovation. Santiago, Chile

Pekkarinen, L.J., 1988. The Hattuvaara gold occurrence, Ilomantsi; a case history. *Annales Universitatis, Turkuensis, Series 24C–67*, pp. 79–87

Phillips G.N., 2013. Australian and global setting for gold in 2013, in *Proceedings world gold 2013, Brisbane, Australia, 26–29 September 2013*. Aust Inst Min Metall. 15–21.

Phillips G.N., Groves D.I., Martyn J.E., 1984. An epigenetic origin for banded iron-formation- hosted gold deposits. *Econ Geol* 79:162–171

Rasilainen, K., 1996. Geochemical alteration of gold occurrences of the late Archean Hattus schist belt, Ilomantsi, eastern Finland: Geological Survey of Finland, Bulletin388, 80p.

Rasilainen, K., Nurmi, P. A., Bornhorst, T. J., 1993. Rock geochemical implications for gold exploration in the late Archean Hattus schist belt, Ilomantsi, eastern Finland. Geological Survey of Finland, Special Paper, 17, 355-362.

Rawlins, B.G., Lister, T.R., Mackenzie, A.C., 2002. Trace metal pollution of soils in northern England. *Environ. Geol.*46, 612–620.

Reimann, C., 2005. Geochemical mapping: technique or art? *Geochemistry: Exploration, Environment, Analysis* 5(4): 359-370.



Reimann, C., de Caritat, P., 2017. Establishing geochemical background variation and threshold values for 59 elements in Australian surface soil. *Science of the Total Environment*. 578, 633–648.

Reimann, C., Filzmoser, P., Garrett, R.G., 2005. Background and threshold: critical comparison of methods of determination. *Science of the Total Environment* 346(1-3): 1-16.

Reimann, C., & Garrett, R. G. (2005). Geochemical background—concept and reality. *Science of the total environment*, 350(1-3), 12-27.

Ridley JR, Diamond LW (2000) Fluid chemistry of orogenic lode gold deposits and implications for genetic models. *Rev Econ Geol* 13:141–162

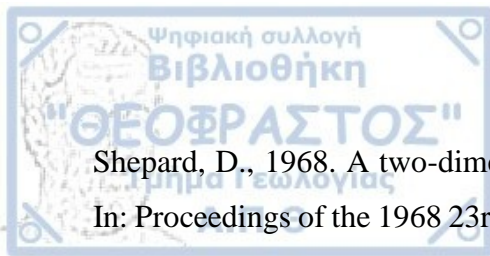
Robinson, T.P., Metternicht, G., 2006. Testing the Performance of Spatial Interpolation Techniques for Mapping Soil Properties. *Computers and Electronics in Agriculture*. 50, 97–108.

Rose, A.W., Hawkes, H.E., Webb, J.S., 1979. *Geochemistry in Mineral Exploration*, 2nd ed., Academic Press, London.

Sakellaris (2016), Unpublished report

Salminen, R., Hartikainen, A., 1985. Glacial transport of till and its influence on the interpretation of geochemical results in North Karelia, Finland. *Geological Survey of Finland* 48 Bulletin 335.

Shepard, D., 1964. A two-dimensional interpolation function for irregularly data spaced. *ACM National Conference*, 517–524.



Shepard, D., 1968. A two-dimensional interpolation function for irregularly-spaced data. In: Proceedings of the 1968 23rd ACM national conference, ACM, New York, pp 517–524

Schodde R.C., 2021. Trends in Gold Exploration with a special focus on quantifying discovery performance. Centre for Exploration Targeting, UWA. May 2021. www.minexconsulting.com

Shuguang, Z., Kefa, Z., Yao, C., Jinlin, W., & Jianli, D. (2015). Exploratory data analysis and singularity mapping in geochemical anomaly identification in Karamay, Xinjiang, China. *Journal of Geochemical Exploration*, 154, 171-179.

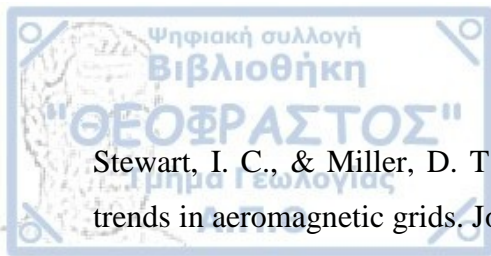
Sinclair, A. J. (1974). Selection of threshold values in geochemical data using probability graphs. *Journal of geochemical exploration*, 3(2), 129-149. Society. American Bulletin 15: 483-506.

Singer, D.A., 1993. Basic concepts in three-part quantitative assessments of undiscovered mineral resources. *Nonrenewable Resources* 2(2): 69-81.

Sorjonen-Ward, P., 1993, An overview of structural evolution and lithic units within and intruding the late Archean Hattu schist belt, Ilomantsi, eastern Finland. *Geological Survey of Finland, Special Paper 17*, 9–102.

Sorjonen-Ward, P. B., Hartikainen, A., Nurmi, P. A., Rasilainen, K., Schaub, P., Zhang, Y., & Liikanen, J. (2015). Exploration targeting and geological context of gold mineralization in the Neoproterozoic Ilomantsi greenstone belt in eastern Finland. *Mineral Deposits of Finland*, 435-466.

Sorjonen-Ward, P., Luukkonen, E.J., 2005. Archean rocks. In: Lehtinen, M., Nurmi, P.A., Rämö, O.T. (Eds.), *Precambrian Geology of Finland—Key to the Evolution of the Fennoscandian Shield*. Elsevier B.V., Amsterdam, pp. 19–99.



Stewart, I. C., & Miller, D. T. (2018). Directional tilt derivatives to enhance structural trends in aeromagnetic grids. *Journal of Applied Geophysics*, 159, 553-563.

Stoch, B., Anthonissen, C. J., McCall, M. J., Basson, I. J., Deacon, J., Cloete, E., Botha, J., Britz, Strydom, M., Nel, D., Bester, M., 2018. 3D implicit modeling of the Sishen Mine: new resolution of the geometry and origin of Fe mineralization. *Mineralium Deposita*, 53(6), 835-853.

Tarantola A, Mullis J, Venneemann T, Dubessy J, de Capitani C (2007) Oxidation of methane at the CH₄/H₂O-(CO₂) transition zone in the external part of the Central Alps, Switzerland: evidence from stable isotope investigations. *Chem Geol* 237:329–357

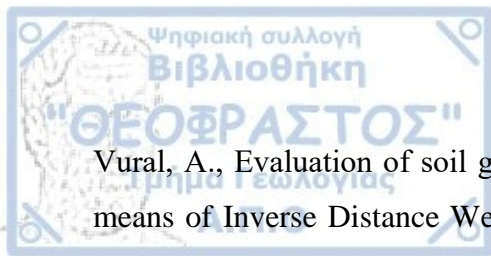
Tukey, J.W., 1977. *Exploratory Data Analysis*, Addison-Wesley, Reading.

Vaasjoki, M., Korsman, K. and Koistonen, T. 2005. Overview. In: Lehtinen, M., Nurmi, P.A., Rämö, O.T. (Editors), *Precambrian Geology of Finland - Key to the Evolution of the Fennoscandian Shield*. Elsevier B.V., Amsterdam, pp. 1-18.

Vaasjoki, M., Sorjonen-Ward, P., Lavikainen, S., 1993. U-Pb age determinations and sulfide Pb-Pb characteristics from the late Archaean Hattu schist belt, Ilomantsi, eastern Finland. *Geological Survey of Finland, Special Paper* 17, 103–131.

Vielreicher N.M., Groves D.I., Snee L.W., Fletcher I.R., Mc Naughton N.J., 2010. Broad synchronicity of three gold mineralization styles in the Kalgoorlie gold field—SHRIMP, U-Pb, and ⁴⁰Ar/³⁹Ar geochronological evidence. *Econ Geol* 105:187–227

Vollgger, S. A., Cruden, A. R., Ailleres, L., & Cowan, E. J., 2015. Regional dome evolution and its control on ore-grade distribution: Insights from 3D implicit modelling of the Navachab gold deposit, Namibia. *Ore Geology Reviews*, 69, 268-284.



Vural, A., Evaluation of soil geochemistry data of Canca area (Gümüşhane, Turkey) by means of Inverse Distance Weighting (IDW) and kriging methods-preliminary findings. Bulletin of the Mineral Research and Exploration 2019. 158: 195-216.

Webster, R., and Oliver, M. A., 1992. Sample adequately to estimate variograms of soil properties. Journal of Soil Science, 40, 493–496.

Weihed, P., Arndt N., Billström, K., Duchesne, J.-C., Eilu, P., Martinsson, O., Papunen, H. and Lahtinen R., 2005. Precambrian geodynamics and ore formation: the Fennoscandian Shield. Ore Geology Reviews 27, 273-322.

Wilde A.R., Bierlein F.P., Pawlitschek M., 2004. Litho-geochemistry of orogenic gold deposits in Victoria, SE Australia: A preliminary assessment for undercover exploration. Journal of Geochemical Exploration, 84, 35–50

Wyman D.A., Cassidy K.F., Hollings P., 2016. Orogenic gold and the mineral systems approach: resolving fact, fiction and fantasy. Ore Geol Rev 78:322–335

Xie, Y., Chen, T. B., Lei, M., Yang, J., Guo, Q. J., Song, B., & Zhou, X. Y., 2011. Spatial distribution of soil heavy metal pollution estimated by different interpolation methods: Accuracy and uncertainty analysis. Chemosphere, 82(3), 468-476.

Xu, H., and Zhang, C., 2023. Development and applications of GIS-based spatial analysis in environmental geochemistry in the big data era. Environmental Geochemistry and Health, 45(4), 1079-1090.

Xuejing, X., and Xueqiu, W., 1991. Geochemical exploration for gold: a new approach to an old problem. Journal of Geochemical Exploration, 40(1-3), 25-48.



Yang L.Q., Deng J., Wang Z.L., Zhang L., Guo L.N., Song M.C., Zheng X.L., 2014. Mesozoic gold metallogenic system of the Jiaodong gold province, eastern China. Acta Petrol Sin 30:2447–2467 (in Chinese with English abstract)

Yousefi, M., & Carranza, E. J. M. (2015). Prediction–area (P–A) plot and C–A fractal analysis to classify and evaluate evidential maps for mineral prospectivity modeling. Computers & Geosciences, 79, 69-81.

Yusta, I., Velasco, F., Herrero, J.-M., 1998. Anomaly threshold estimation and data normalization using EDA statistics: application to lithochemical exploration in Lower Cretaceous Zn±Pb carbonate-hosted deposits, Northern Spain. Applied Geochemistry 13(4): 421-439.

Zhang, C., Tang, Y., Xu, X., & Kiely, G., 2011. Towards spatial geochemical modelling: Use of geographically weighted regression for mapping soil organic carbon contents in Ireland. Applied Geochemistry, 26, 1239–1248.

Zhang, C., Zuo, R., Xiong, Y., Shi, X., & Donnelly, C. (2021). GIS, geostatistics, and machine learning in medical geology. Practical Applications of Medical Geology, 215-234.

Zhu, Y. S., 1997. Prospectivity mapping methods. Beijing: Geological Publish House.

Zuo, R., Xia, Q., & Wang, H. (2013). Compositional data analysis in the study of integrated geochemical anomalies associated with mineralization. Applied geochemistry, 28, 202-211.